R and D CENTER LABORATORY TECHNICAL REPORT

NO. 12685

Propagation of Visible and Infrared Radiation by Fog, Rain, and Snow

Contract No. DAAE07-81-G-4006

July, 1982

by L. W. Winchester, Jr.
and
G. G. Gimmestad

Keweenaw Research Center
Michigan Technological University
Houghton, Michigan 49931

U.S. ARMY TANK-AUTOMOTIVE COMMAND
RESEARCH AND DEVELOPMENT CENTER
Warren, Michigan 48090

Notices

The findings in this report are not to be construed as an official Department of the Army Position.

Mention of any trade names or manufacturers in this report shall not be construed as advertising nor as an official indorsement or approval of such products or companies by the U.S. Government.

Destroy this report when it is no longer needed. Do not return to the originator.

SECURITY CLASSIFICATION OF THIS PAGE (When Data Entered)

REPORT DOCUMENTATION PAGE		READ INSTRUCTIONS BEFORE COMPLETING FORM
1. REPORT NUMBER 12685	2. GOVT ACCESSION NO.	3. RECIPIENT'S CATALOG NUMBER
4. TITLE (and Subtitle) Propagation of Visible and Infrared Radiation in Fog, Rain, and Snow		5. TYPE OF REPORT & PERIOD COVERED Final Report 9 Apr 1981 - 1 Apr 1982 6. PERFORMING ORG. REPORT NUMBER KRC 82-10
7. AUTHOR(s) L. W. Winchester, Jr. and G. G. Gimmestad		8. CONTRACT OR GRANT NUMBER(s) DAAE07-81-G-4006 Delivery Order 0002
9. PERFORMING ORGANIZATION NAME AND ADDRESS Keweenaw Research Center Michigan Technological University Houghton, Michigan 49931		10. PROGRAM ELEMENT, PROJECT, TASK AREA & WORK UNIT NUMBERS
11. CONTROLLING OFFICE NAME AND ADDRESS U.S. Army Tank-Automotive Command Warren, Michigan 48090		12. REPORT DATE July, 1982 13. NUMBER OF PAGES 94
14. MONITORING AGENCY NAME & ADDRESS(if different from Controlling Office)		15. SECURITY CLASS. (of this report) Unclassified 15a. DECLASSIFICATION/DOWNGRADING SCHEDULE

16. DISTRIBUTION STATEMENT (of this Report)
Approved for Public Release

Distribution Unlimited

17. DISTRIBUTION STATEMENT (of the abstract entered in Block 20, if different from Report)

18. SUPPLEMENTARY NOTES

19. KEY WORDS (Continue on reverse side if necessary and identify by block number)

Atmospheric Transmission
Infrared Transmission
Obscured Atmosphere
Infrared Extinction
Visible Extinction
Phase Function

20. ABSTRACT (Continue on reverse side if necessary and identify by block number)

Measurements of the attenuation of radiation at 0.6328, 1.06, and 8 to 12 micrometers by fog, rain, and snow are reported. Theoretical models are presented which account for the scattering properties of fog droplets, raindrops, and snow crystals at each wavelength. Attenuation by fog in the 8 to 12 micrometer band is shown to be a function of the liquid water content of the fog while attenuation at 0.6328 micrometers is a function of

DD FORM 1 JAN 73 1473 EDITION OF 1 NOV 65 IS OBSOLETE

SECURITY CLASSIFICATION OF THIS PAGE (When Data Entered)

both liquid water content and the fog droplet size distribution. It is shown that not only must the scattering properties of rain drops and snow crystals be properly modeled, but the susceptibility of the experimental instruments to scattered radiation must also be known.

SUMMARY

A model of the effects of countermeasures to ground vehicle infrared signatures on threat weapon system performance must take into account the propagation of infrared radiation through the earth's atmosphere. A number of models for atmospheric transmission have been published by various authors, and one of them (LOWTRAN) works well for clear air, indicating that it accounts for molecular absorption reasonably well. When particles are present in the atmosphere, existing models are not as good. The GAP model (Moulton, et al 1976) addresses this problem by relating infrared extinction to visible extinction (found from visibility). The GAP model has been found to have the following weaknesses:

(1) It makes no distinction between molecular absorption and extinction by particles;

(2) Infrared extinction is calculated from visibility, rather than from weather parameters;

(3) GAP model parameters are obtained by fitting curves to experimental data which may be instrument-dependent;

(4) In fog, the model predictions are representative only of specific fogs in certain locations.

The phase function has been found to be of great importance in determining the transmission of radiation through a scattering atmosphere. The rain model has illustrated the need to use the proper phase function when computing atmospheric transmission.

The added dimension of finite size receivers increases the need for knowledge of the scatterers, hence the phase function when applying relations derived from data obtained on one set of apparatus to another instrument.

A detailed investigation is presented for the scattering of visible and infrared radiation by fog, rain, and snow. The theoretical analysis is compared to the measured data obtained at the Keweenaw Research Center. The analysis and the results are compared to the prediction of other available models. In addition, the implication of the present work to the on-going TACOM modeling effort of target signatures is discussed.

PREFACE

The work described in this technical report is sponsored by the Countermeasure Function, DRSTA-ZSC of the U.S. Army Tank-Automotive Command under contract DAAE07-81-G-4006, delivery order 0002. The Atmospheric Transmission facility at the Keweenaw Research Center is operated in support of the Vehicle Signature Modeling effort and is dedicated to a study of the transmission properties of the atmosphere through snow and rain. For further information, contact the Keweenaw Research Center, R.R. 1, Box 94-D, Calumet, Michigan 49913 or the Tank-Automotive Command, DRSTA-ZSC, Warren, Michigan 48090.

T A B L E O F C O N T E N T S

LIST OF TABLES

LIST OF FIGURES

INTRODUCTION

The attenuation of visible and infrared radiation in the atmosphere is due to absorption and scattering by its constituents. Absorption by air molecules such as NO_2, O_2, O_3, CH_4, and CO has been studied extensively and compiled by McClatchey et al (1973). Using the compilation which includes the frequency, half-width, and oscillator strength of each resonance as well as the energy and relevant quantum numbers of the lower state, it is possible to compute the absorption by clear air (non-particulate) for wavelengths greater than 1.0 micrometer. This type of calculation is very useful over a small frequency region such as a laser line, but very time-consuming for a broad band. Selby et al (1978) has developed a low resolution computer program (LOWTRAN), which is an accurate predictor of clear air absorption. FASCODE, a fast high resolution atmospheric transmission program capable of using Doppler, Lorentz, and/or Voight line profiles, was developed by Smith et al (1978) for use in computing transmission in a layered atmosphere. This study is concerned with transmission in the atmospheric boundary layer where the density of each atmosperic species and the pressure are assumed to be uniform along the path.

Since the atmospheric gas molecules are very small compared with the wavelengths of radiation, any scattering of radiation by these molecules is described by Rayleigh scattering (Fabelinskii, 1968; Shifrin, 1968). The phase function or angular pattern of scattered radiation characteristic of Rayleigh scattering is

$$f_R(\Theta) = \frac{3}{4}(1 + \cos^2\Theta) \qquad (1)$$

where Θ is the scattering angle measured from the forward direction.

Several studies of extinction of electromagnetic radiation by fog, rain, and snow which have appeared in literature

have often presented conflicting results. Chu and Hogg (1960) measured the extinction of radiation at wavelengths of 0.63, 3.5 and 10.6 micrometers in fog, rain, and snow. They obtained a loss of 15.5 I + 2.66 dB/km at 0.6328 micrometer in rain where I is rainfall rate. The loss rate was obtained by a least-squares fit to data between 12.5 and 100 millimeter/hour rainfall. They calculated a single scattering correction term using van de Hulst's (1957) approximation of the extinction efficiency and by assuming a Gaussian pattern to the forward scattering beam. The agreement between measurement and calculation was within 10% for 0.6328 micrometer radiation.

Sokolov and Sukhonin (1971) examined the effect of the functional form of the drop size distribution on calculations of extinction by rain. They compared the measurements of Chu and Hogg (1960) with computations using the drop size distributions of Laws and Parsons (1943), Best (1950), and Barteneva, et al (1967) for rains of intensity between 0 and 100 mm/hr. As Sokolov and Sukhonin did not consider the possibility of any scattered light reaching the receiver, the extinctions of 0.63, 3.5, and 10.6 micrometers are all identical as shown in Figure 1. The data of Chu and Hogg (1960) had also been plotted for the purposes of comparing theory and experiment. Sokolov and Sukhonin concluded that the distribution due to Barteneva, et al (1967) gave the best agreement with experiment. A ray tracing method was used to calculate the backscatter amplitude function. Bisyarin, et al (1971) measured the attenuation coefficient of 0.63 and 10.6 micrometer radiation in snow and rain over a 1.36 km path. In snow they found the following relations for the extinction parameters measured in dB/km

$$\beta_{0.63} = 10.8\ I^{0.53} \tag{2}$$

$$\beta_{10.6} = 15.1\ I^{0.71} \tag{3}$$

where I is the snowfall rate measured in millimeters per hour. Rain measurements were made for rainfall intensities of less than 10 millimeters per hour and are inconclusive.

Recent data from the OPAQUE measurement program at the German station at Birkhof (Jessen, et al, 1980) have indicated that the drop size distribution of rain is an important factor in computing transmission. The authors also place importance on the knowledge of aerosol physics and humidity in order to understand transmission through the atmosphere. The particles which have the largest effect on scattering/absorption are those comparable in size to the wavelength of the radiation. The small rain droplets, comparable in size to some fog droplets, do not have the intense diffraction peak present in scattering by large particles. When dealing with any scattering medium, knowledge of the particle size distribution is of prime importance in understanding the scattering process.

Since the orientation of the snow crystals, as well as their size and shape, must be considered when calculating scattering, the phase functions of various types of snow crystals are needed in order to compute the transmission through a snowy atmosphere. The snow crystal phase functions are of importance in problems involving radiative transfer in cloudy atmospheres as high altitude clouds consist mainly of ice crystals.

Previous experimental studies of the phase function of ice crystals have been concerned with artificial ice crystals. Huffman and Thursby (1969) used a polar nephelometer employing a filtered Xenon arclamp as a source operating at 0.55 micrometers to measure scattering from microscopic ice crystals grown in a refrigerated chamber. They reported that the phase function of hexagonal plates, hexagonal columns and irregular ice crystals were identical at angles less than 130°. Compared with calculations using Mie theory for equivalent spheres, the ice crystals produced more lateral scattering, i.e. scattering in the angular range of 60° to 130°. Since the phase function $f(\theta)$ is normalized as shown below

$$1 = 0.5 \int_0^{\pi} f(\theta) \sin(\theta)\, d\theta \qquad (4)$$

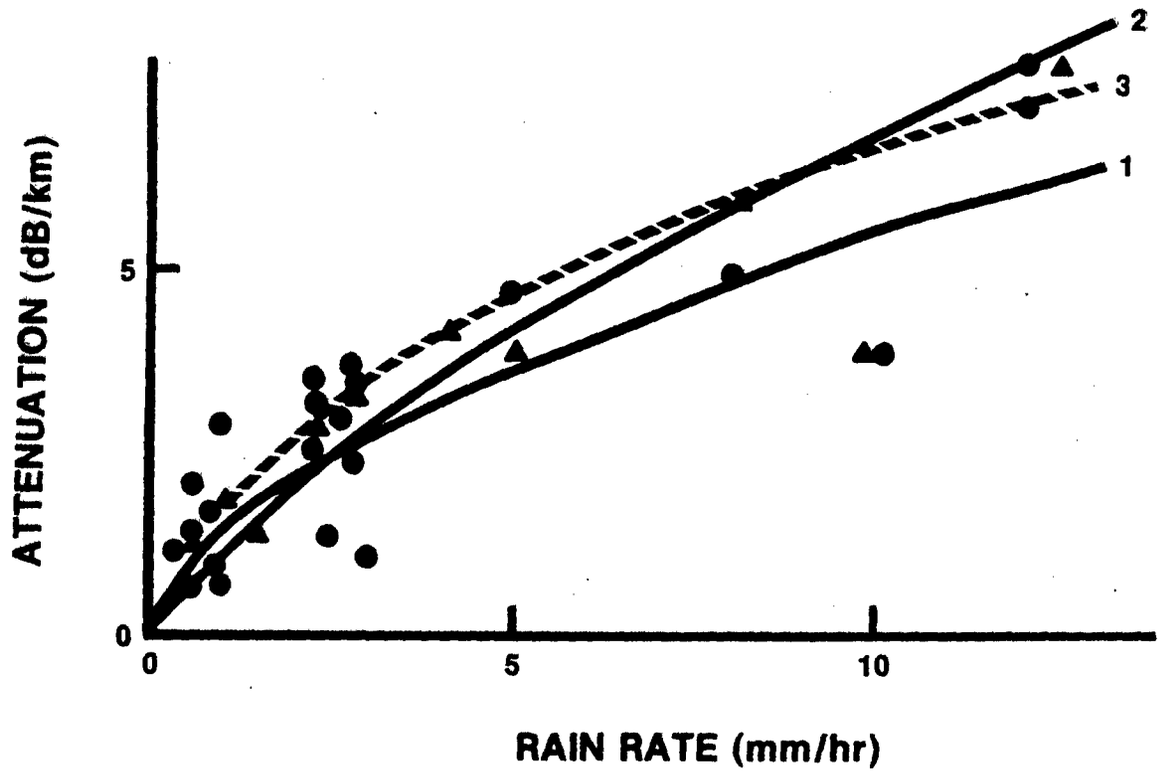

Figure 1. Comparison of attenuation versus rain intensity for several drop size distributions (taken from Sokolov and Sukhonin, 1970). Curves 1 and 2 use the distributions of Best (1950) and Barteneva, et al (1967) while Curve 3 is a least-squares fit.

the increase in lateral scattering must be accompanied by a corresponding decrease in forward scattering and/or backscattering. In a later paper, Huffman (1970) reported on polarized scattering from a Gaussian distribution of hexagonal ice columns with a mode length of 25 micrometers. Defining the polarization ratio as

$$P = (M_1 - M_2)/(M_1 + M_2) \qquad (5)$$

where M_1 and M_2 are the phase functions measured where the polarization of the incident and scattered light are both perpendicular and both parallel, respectively, to the scattering plane, Huffman (1970) found a negative value of the polarization ratio near 22° and a broad maximum near 115°. Dugin et al. (1971) measured phase functions of artificial ice crystals which were mainly platelets, prisms and little stars in the size range of 20 to 100 micrometers. A clear maximum near the 22° halo, an indication of the 46° halo, and considerable lateral scattering were observed. In a subsequent paper, Dugin et al. (1977) measured the phase function of artificial ice crystals in several scattering planes ranging in 30° increments from horizontal to vertical. The results showed that the phase function varied from plane to plane with most of the scattered energy being concentrated in the horizontal and vertical scattering planes. Unfortunately, the size and shape of the crystals varied from plane to plane casting doubt on the significance of the energy concentration data. Haloes were observed at both 22° and 46° in all planes. Preliminary experiments by Liou et al. (1976) using a cold room to study light scattering by ice plates and needles showed fairly strong backscattering and the absence of any structure, although data for angles smaller than 30° was not presented. Later measurements by Sassen and Liou (1979a and b) were made using a small cold chamber at the center of a polar nephelometer instead of immersing the entire instrument in a cold room. Polarized measurements were made for several crystal

types, yielding a very strong depolarized component for backscattering which did not agree with calculated values of the Fresnel coefficients. Nikiforova et al (1977) have obtained the phase functions at a wavelength of 0.63 micrometers of ice crystal fogs having various crystal shapes. They reported that all measurements were found to lie between two curves; one exhibiting the 22° and 46° haloes and relatively intense scattering from 60° to 150°, and the other closely resembling the data of Huffman and Thursby (1969). Recent measurements of the phase functions of columns and platelets by Volkovitskiy et al (1980) have shown the presence of the 22° halo. The authors report no significant difference between the phase functions of columns and platelets.

Since the experimental studies have shown that the phase functions of snow crystals, with the possible exception of graupel, cannot be approximated using Mie theory computations for spheres with either equivalent area or equivalent volume, it is necessary to examine methods of calculating the phase function of snow crystals using other methods. When calculating scattering of radiation of wavelength λ by an object of characteristic size 2r, the size parameter given by

$$\chi = 2\pi r\lambda^{-1} \tag{6}$$

and the complex index of refractions are of great importance. Scattering by right circular cylinders was first studied by Wait (1955) and subsequently reformulated by Greenberg et al (1967), Kerker (1969), and Liou (1972a and b). While these calculations allow for oblique incidence, the cylinder length is assumed to be infinite. Asano and Yamamoto (1975) have reported the results of computations of scattering from spheroids with a size parameter less than 7, while Mugnai and Wiscombe (1980) have calculated the phase functions for moderately nonspherical particles with a size parameter less than 10.

Jacobowitz (1971) used a ray tracing method to compute the phase function of hexagonal ice prisms with size parameters as large as 142. The diffraction peak was added using the Kirchhoff formalism. The 22° halo was evident in all computations and the energy in the halo region was found to be comparable to the energy in the diffraction peak. Wendling et al (1979) computed phase function of hexagonal ice crystals in the form of columns and platelets. They reported haloes at 22° and 46° and, contrary to the results of Jacobowitz (1971), strong backscattering and the absence of icebows. Results obtained for randomly oriented hexagonal ice columns and plates were in good agreement with the experimental data of Nikiforova et al (1977). Liou and Coleman (1979) have computed the phase function of hexagonal columns and plates randomly oriented in space using a ray tracing method for wavelengths of 0.55 and 10.6 micrometers. The major features of their phase function include strong forward scattering, a halo in the region between 20° and 30° and a weak halo at 46°. Scattering at angles greater than 84° is attributed to end effects and internal reflections.

Meteorological visibility is a required input to the current level of military models such as GAP (Moulton et al, 1976) and E-O SAEL (Duncan et al, 1979) which predict the attenuation in various infrared regions of the spectrum in adverse weather conditions. Using Kochsmeider's relation, the extinction coefficient at 0.55 micrometer is given by

$$\beta_{0.55} = \frac{3.912}{V} \qquad (7)$$

where V is the meteorological visibility. The visible extinction coefficient is then used to calculate the extinction coefficient in the desired infrared band by assuming that the logarithm of the infrared extinction coefficient is either a linear (Moulton et al., 1976; Duncan et al., 1979) or quadratic (Shields, 1978) function of the logarithm of the extinction coefficient at 0.55 micrometer. Experimental data collected at Fort A.P. Hill, Virginia, and at

Grafenwoehr, Germany, were used to obtain the necessary coefficients of the above-mentioned functions for such general types of weather conditions as fog, rain, and snow. Fog was further broken down into three categories: "dry", "wet", and "all". A fog was classified "wet" if condensation collected on exposed metal surfaces and "dry" otherwise. The major weakness of this approach is that the extinction coefficient in the visible region of the spectrum is not calculated from the weather parameters. The results for attenuation of radiation in the 3 to 5 micrometer region compared to attenuation at 0.55 micrometer by "all", "dry", and "wet" fogs are shown in Figures 2, 3, and 4, respectively, which were taken from the report by Turner, et al (1980). The visibility ranges from 0.4 to 2.5 kilometers. The authors note that the variance in the data is much less for "dry" fogs than for "wet" fogs, and suggests that the atmospheric conditions vary less for "dry" fogs as far as the intrinsic particle properties are concerned. A similar result was obtained for extinction in the 8 to 12 micrometer region as shown in Figures 5, 6, and 7. Measurements made for a single day are in much better agreement with a linear equation, as shown by some typical data in Figure 8. The data from Grafenwoehr and Fort A.P. Hill were collected at thirty-minute intervals. As the time between measurements is long compared with fog lifetimes, it is not possible for the GAP model to follow the evolution of fogs as they form and dissipate.

Winchester, et al (1980a) have shown that the contribution of scattering processes to extinction is comparable to that of absorption in the infrared and dominates extinction in the visible range. The model for extinction of radiation in fogs must include an algorithm for calculating the ability of the detection or viewing device to collect scattered radiation (Bruscaglioni, 1978 and 1979; Bruscaglioni and Ismaelli, 1978 and 1979; Winchester, et al (1980a and b). Such a feature will allow for implementation of the model for any set of equipment, not just the apparatus on which the original data were taken, as in the case of the GAP model.

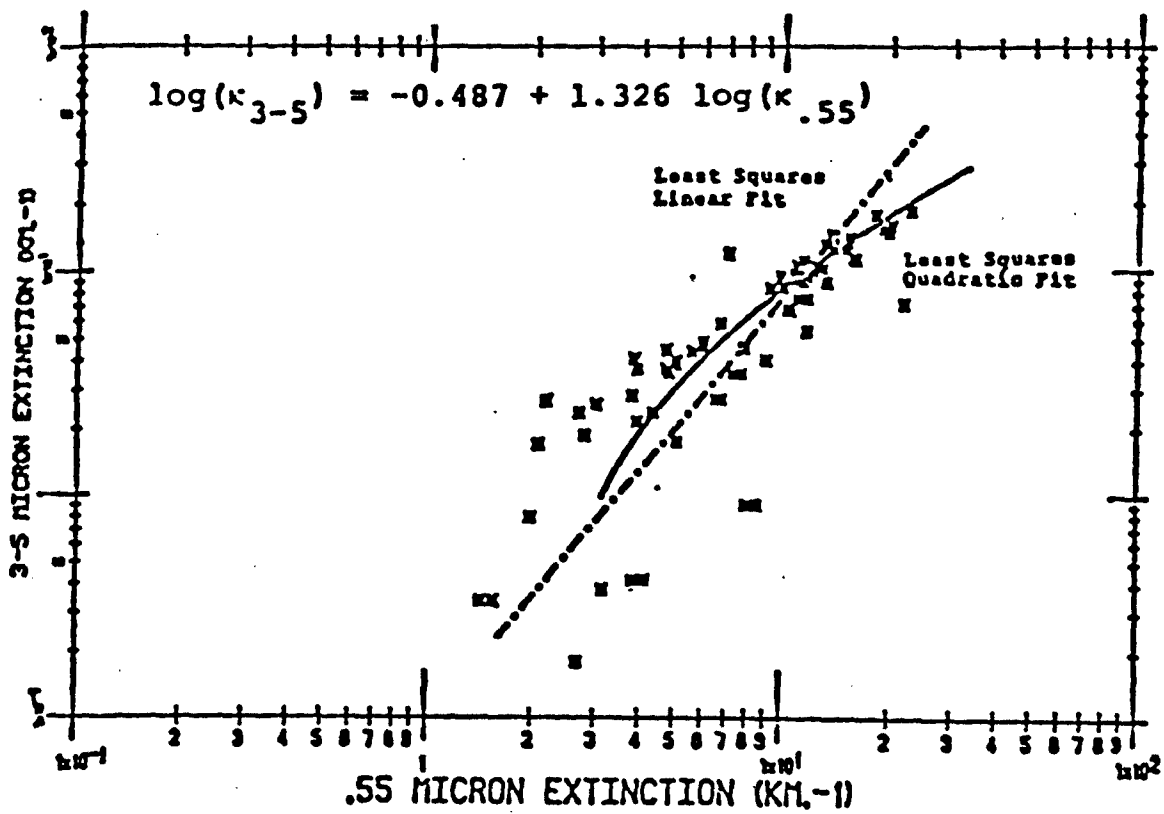

Figure 2. Volume Extinction coefficients in the 3 to 5 micrometer band and at 0.55 micrometers for "all" fogs. (A. P. Hill data between April 1977 and November 1977, taken from Turner, et al (1980)).

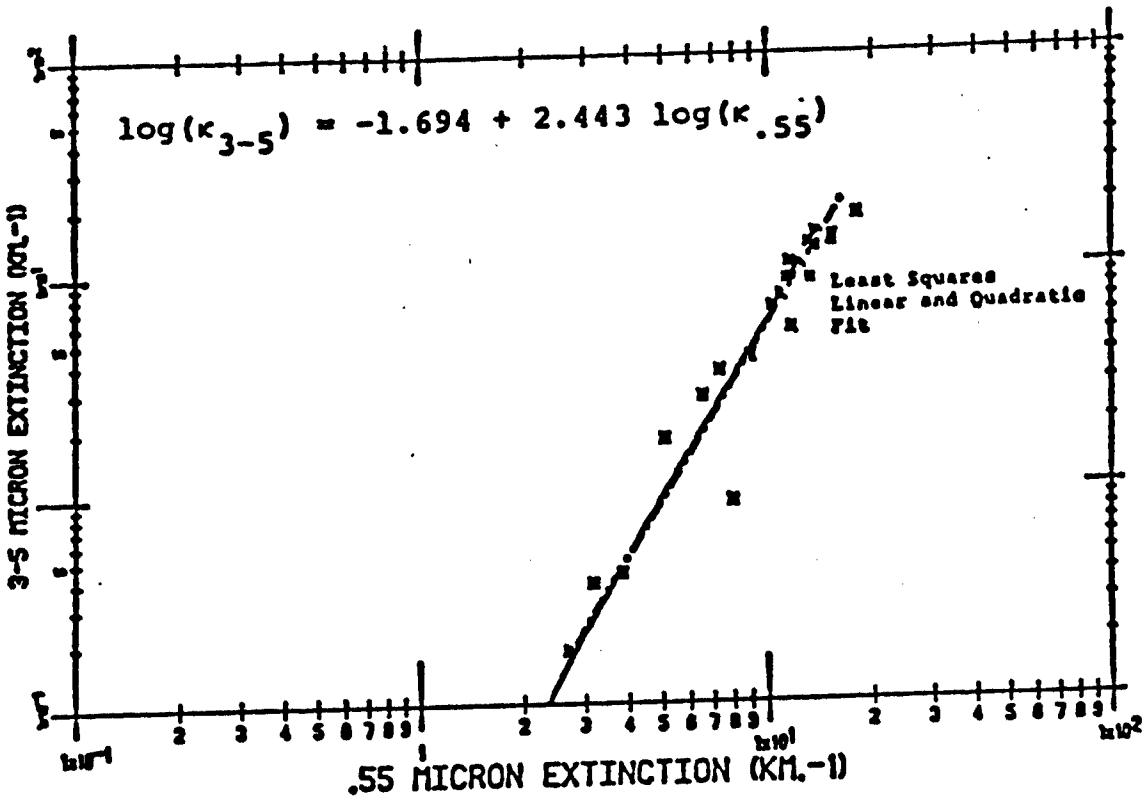

Figure 3. Volume extinction coefficients in the 3 to 5 micrometer band and at 0.55 micrometers for "dry" fogs. (A. P. Hill data between June 1977 and November 1977, taken from Turner, et al (1980)).

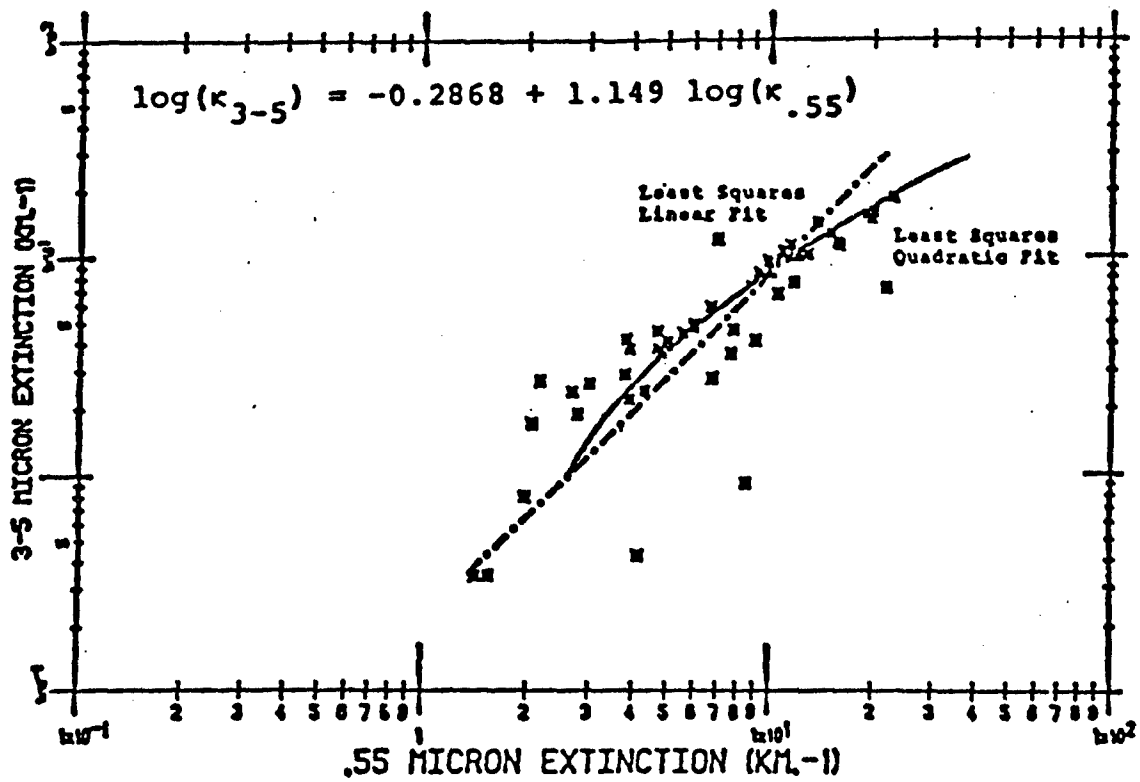

Figure 4. Volume extinction coefficient in the 3 to 5 micrometer band and at 0.55 micrometers for "wet" fogs. (A. P. Hill data between April 1977 and November 1977, taken from Turner, et al (1980)).

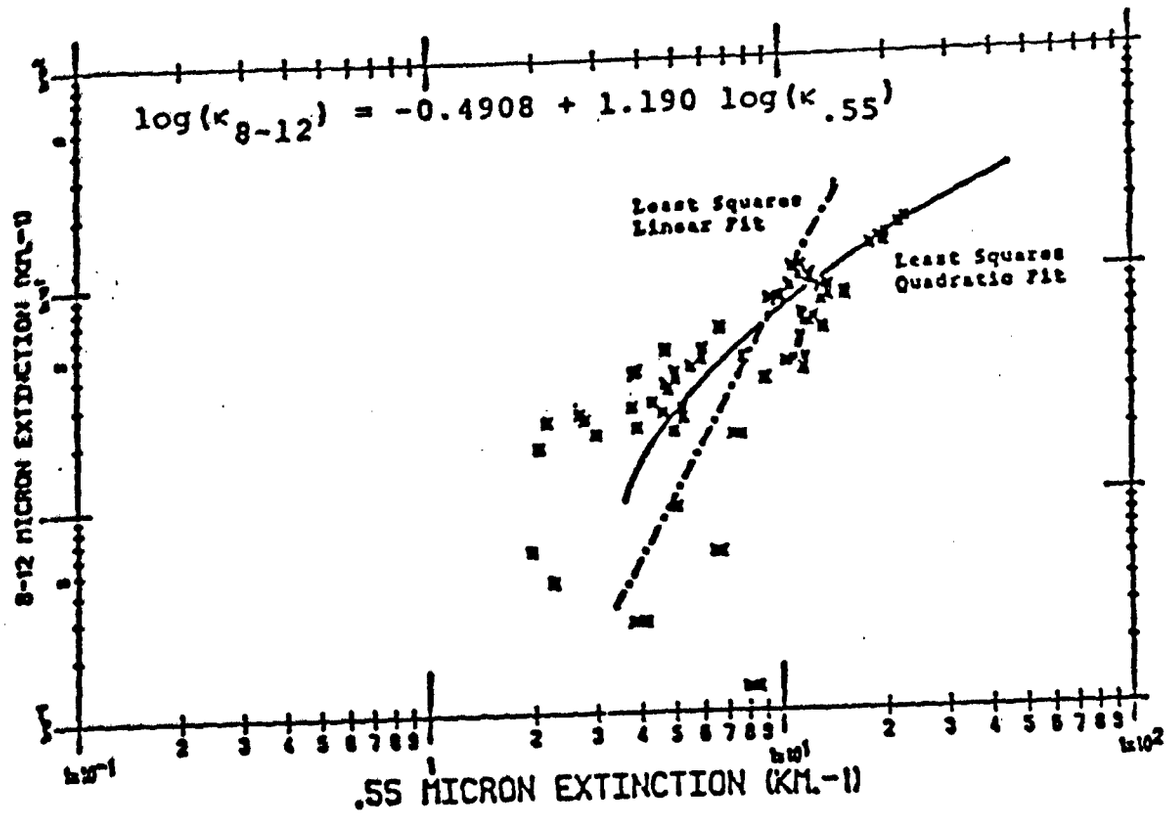

Figure 5. Volume extinction coefficient in the 8 to 12 micrometer band and at 0.55 micrometers for "all" fogs. (A. P. Hill data between April 1977 and November 1977, taken from Turner, et al (1980)).

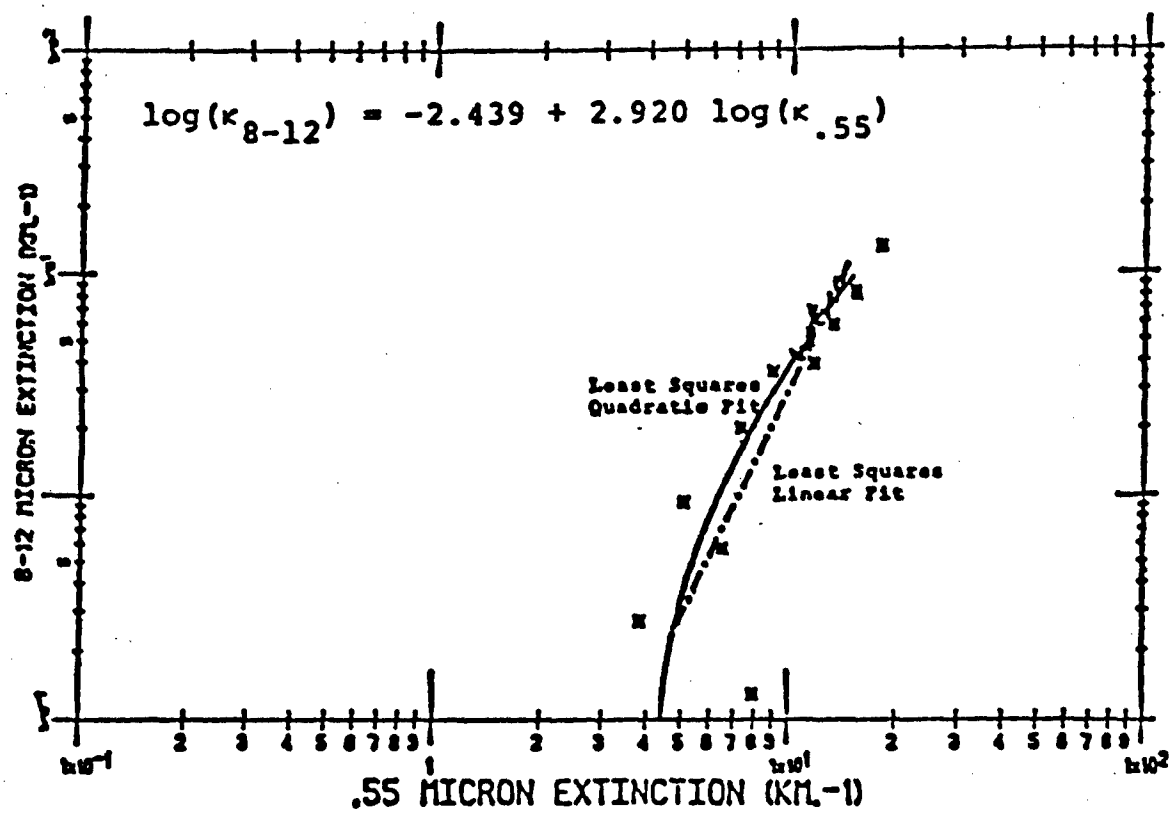

Figure 6. Volume extinction coefficient in the 8 to 12 micrometer band and at 0.55 micrometers for "dry" fogs. (A. P. Hill data between June 1977 and November 1977, taken from Turner, et al (1980)).

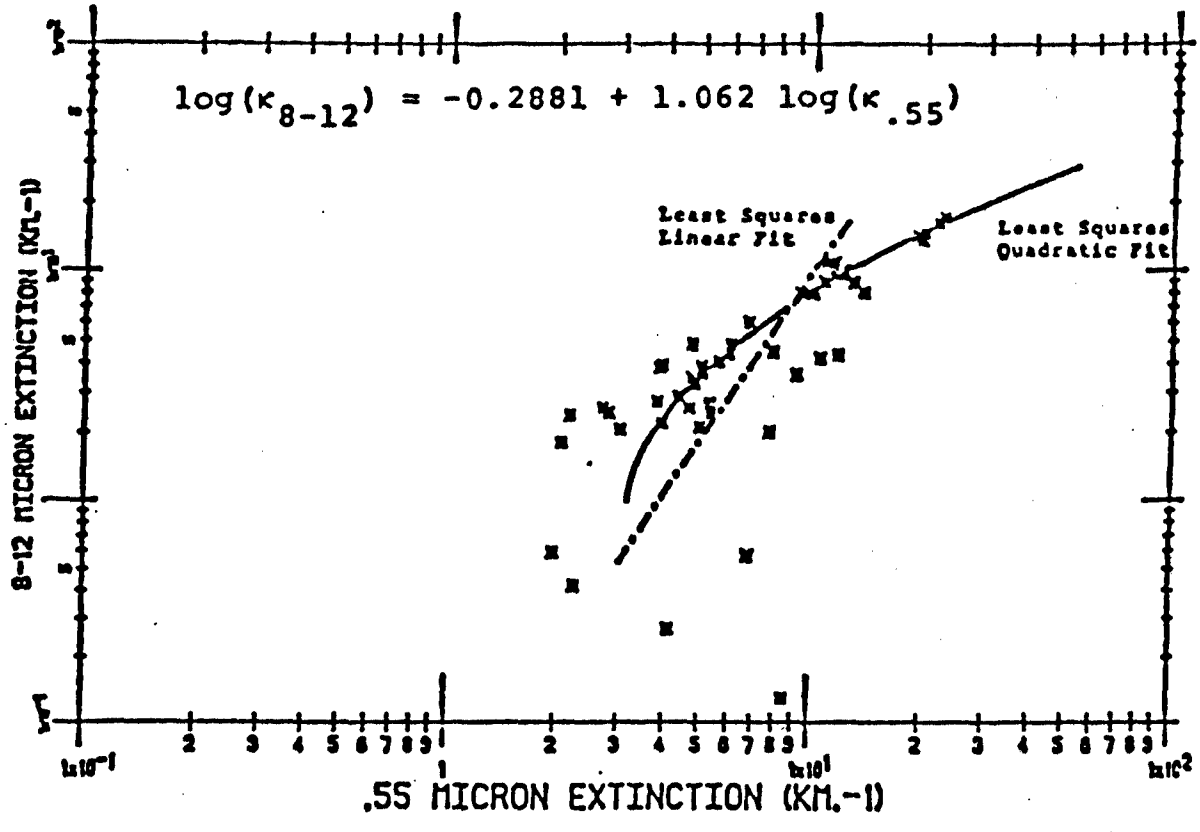

Figure 7. Volume extinction coefficient in the 8 to 12 micrometer band and at 0.55 micrometer for "wet" fogs. (A. P. Hill data between April 1977 and November 1977, taken from Turner, et al (1980)).

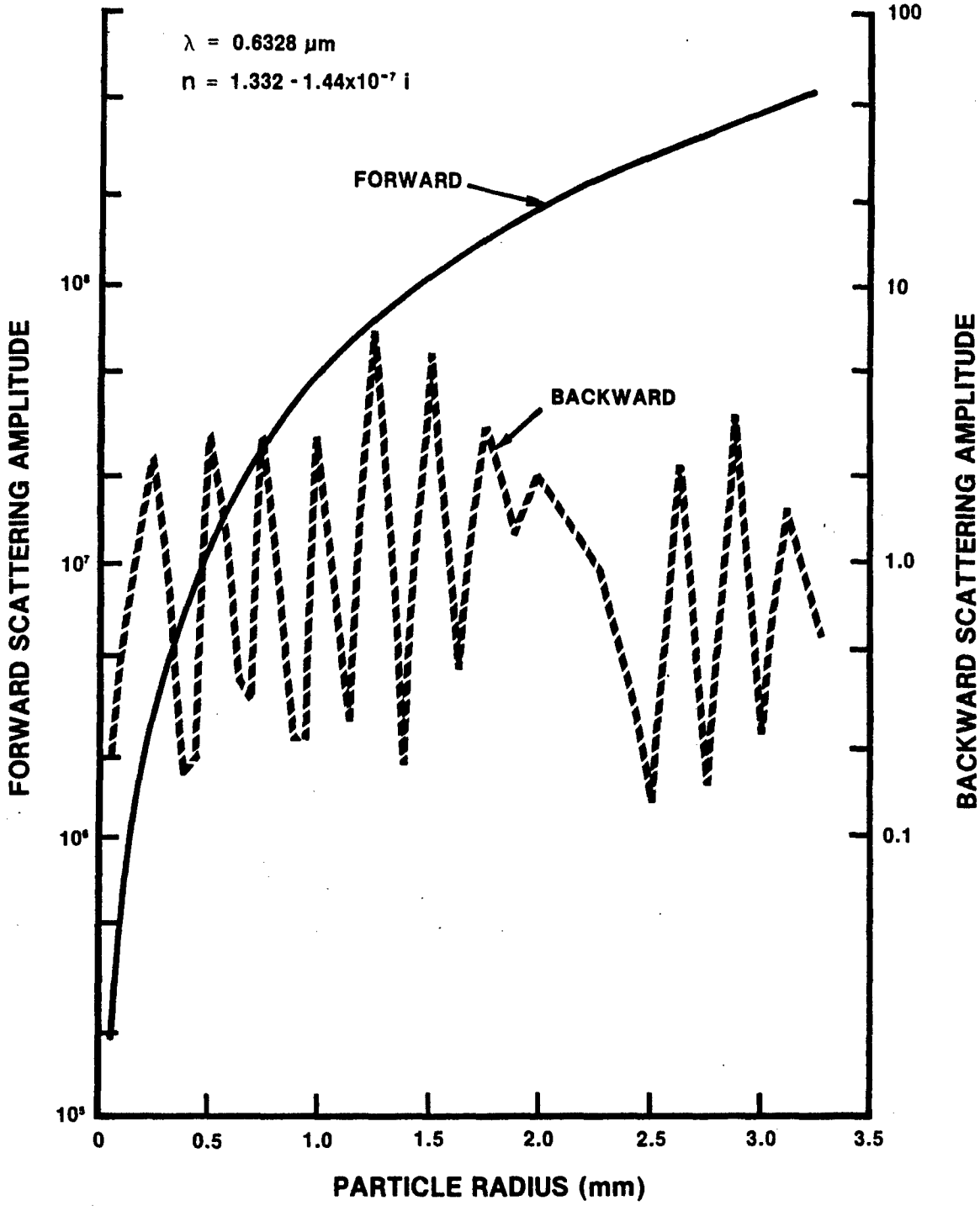

Figure 8. Variation of the forward and backward scattering intensities with the particle radius.

The large scatter in the GAP and OPAQUE data results from combining data from many different fogs into one data plot. Because fogs are characterized by the particle size distribution function, and because the ratio of the infrared extinction to the visible extinction is very sensitive to particle size, a large scatter in fog extinction data should be expected when considering many fogs. Another contribution to extinction is absorption by the air. This contribution is dependent on weather parameters such as temperature and pressure and must be predicted separately in order to isolate the extinction due to fog. As Turner, et al (1980) have suggested, the linear relation between the logarithms of the extinction coefficients may be a good approximation for one fog. If measurements are made at intervals on the order of a minute instead of at half-hourly intervals, as in the case of the GAP and OPAQUE data, the extinction of radiation may be studied as the fog evolves. This is clearly evident from data sampled at one-minute intervals at the Keweenaw Research Center (KRC), which will be discussed below.

OBJECTIVE

The objective of this work is to develop a better understanding of the propagation of infrared radiation through the lower atmosphere especially in adverse weather. The approach consists of a program of experimental measurements and computer modeling combined with a review of the work of other investigators.

RECOMMENDATIONS

For calculating infrared absorption due to molecules, LOWTRAN should be used.

The model used to compute attenuation of radiation at a wavelength of 0.6328 micrometers due to rain, as described in this report should be used as part of the vehicle signature model. The transmission in the 8 to 12 micrometer band may then be computed using data presented here on the relation between the two extinction coefficients.

A model of extinction by snow as a function of snowfall rate and/or liquid water content should be developed by augmenting the KRC weather station with snowfall measuring equipment.

A study of extinction by fog based on a method presented in this report could be made by installing a particle size measuring system on the KRC transmission range.

Snow phase function measurements at 1.06 micrometers should be performed.

A 10.6 micrometer laser should be installed on the KRC transmission range to obtain data for use with CO_2 laser rangefinders.

THEORETICAL FORMULATION

Extinction by particulate matter is in general due to both scattering and absorption. In order to assess the relative importance of scattering versus absorption, the complex index of refraction must be known. Scattering is governed by the real part of the index of refraction while absorption is a function of the imaginary part. The phase function $f(\Theta,\phi)$, namely the angular dependence of the scattered light, is usually normalized

$$\tilde{\omega} = \frac{1}{4\pi} \int_{4\pi} f(\Theta,\phi)\, d\Omega \qquad (8)$$

where $\tilde{\omega}$ is the albedo, or ratio of scattering to total extinction (absorption plus scattering) and Θ and ϕ are angles describing the scattering direction in spherical polar coordinates. In practice, scattering is assumed to be independent of the azimuthal angle ϕ so Eq. 8 may be rewritten

$$\tilde{\omega} = \frac{1}{2} \int_{0}^{\pi} f(\Theta) \sin\Theta\, d\Theta \qquad (9)$$

where Θ is the scattering angle. As the scattering parameter $\rho = 2\pi\, r/\lambda$ (where r is the particle radius and λ is the wavelength of the incident electromagnetic radiation) is increased, the amount of forward scattering (near 0°) increases, while backscattering (180°) oscillates, as illustrated in Figure 8 for the case of raindrops illuminated by radiation with a wavelength of 0.6328 micrometer from a Helium-Neon laser. When calculating transmission through a scattering atmosphere, an estimate of the amount of radiation which reaches the detector after experiencing one or more scattering events must be evaluated to determine what order scattering processes are important. Because it is a measure of the angular spread of the scattered radiation, the phase function is essential to an accurate estimate of transmission in a scattering atmosphere.

When calculating the received power of a laser transmissometer the relative importance of both scattering and absorption must be carefully considered. Since some of the scattered radiation will reach the detector after one or more scattering events, the receiver parameters must be considered when evaluating the scattering contribution. The instrument dependence must be accounted for when either measuring or using experimental values of atmospheric extinction under adverse weather conditions such as fog, rain, or snow. The amount of scattering is dependent on the real part of the index of refraction while absorption is related to the imaginary part. For a particle described by a large scattering parameter ($\chi >> 1$), a very strong forward scattering is observed. The shape of the particles is also a factor in determining the phase function. Computations similar to those of Mie (1908) for spheres have been made for cylinders (Kerker, 1969) and regular hexagonal plates (Jacobowitz, 1971).

The geometry of a laser transmissometer is shown in Figure 9. A laser with power I_L and negligible beam divergence is located a distance R from a receiver described by a collection optics diameter H and an acceptance angle α_R.

The amount of power reaching the receiver without undergoing a scattering event is given by

$$I_o = I_L \, g \, P_{NS} \, (R) \tag{10}$$

where g is a geometrical factor related to the divergence and profile of the laser beam and the type and size of the receiver optics. The probability of a photon traveling a distance R without being scattered or absorbed, P_{NS} (R), can be written

$$P_{NS} \, (R) = \exp \{-[N(\sigma_s + \sigma_A) + \beta_{AIR}]R\} \tag{11}$$

where N, σ_s, and σ_A are the number density, scattering cross section and absorption cross section, respectively, of the particles and β_{AIR} is the atmospheric extinction coefficient.

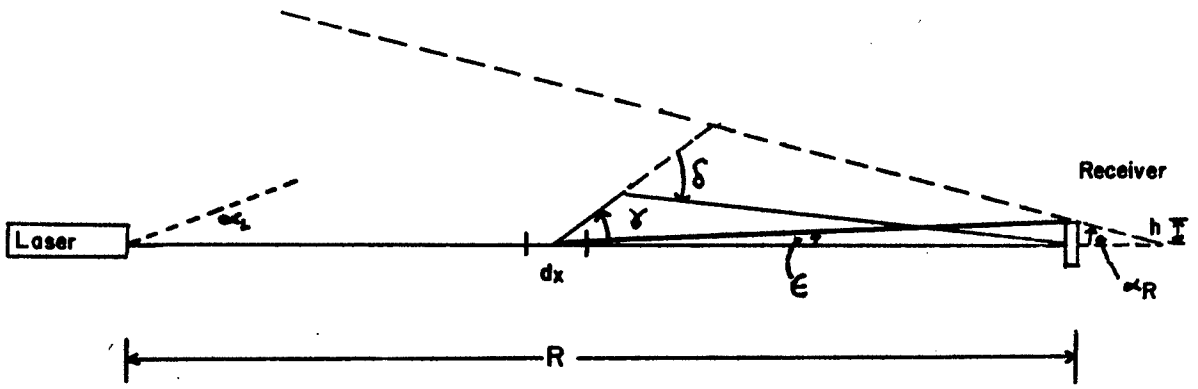

Figure 9. Laser Transmissometer Geometry

The contribution of first order scattering to received power can be written

$$I_1 = I_L \int_0^R \int_{\Omega(\varepsilon)} P_s(x)\, f(\varepsilon)\, P_{NS}\,(R - x)\, d\Omega(\varepsilon)\, dx \qquad (12)$$

The probability of scattering in the element dx after traveling a distance x is $P_s(x)\, dx$ where

$$P_s(x) = N\sigma_s\, P_{NS}(x) \qquad (13)$$

and the phase function $f(\varepsilon)$ has been evaluated at the scattering angle ε. The solid angle $\Omega(\varepsilon)$ is limited by the size of the receiver. The expression for second order scattering is written as

$$I_2 = I_L \int_0^R \int_x^R \int_{\Omega(\gamma)} \int_{\Omega(\delta)} P_s(x)\, f(\gamma)\, P_S(x' - x)\, f(\delta)\, P_{NS}(R - x') \, d\Omega(\delta) d\Omega(\gamma)\, dx'\, dx \qquad (14)$$

where the first and second scattering angles are given by γ and δ, respectively.

As can be seen from Eqs. 12 and 14, the magnitude of the scattering contributions depends on the phase function. A critical factor in determining the type of scattering, hence the required phase function, is the size parameter ρ. When $\rho << 1$ and $|m|\rho < 1$, where $|m|$ is the complex index of refraction, the scattering is referred to as Rayleigh scattering described by the phase function shown in Eq. 1.

When dealing with spherical particles with $\rho > 0.1$, a rigorous calculation is required. For distributions of spherical particles the scattering amplitudes must be calculated for each particle size using Mie theory (1908) and averaged over the particle size distribution function. For very large spheres ($\rho > 10$) it is often more efficient to use geometrical optics to calculate the phase function.

In order to compute the attenuation of radiation by rain, the atmospheric raindrop size distribution function must be known. Laws and Parsons (1943) have measured the drop size distribution at the surface. The atmospheric rain drop distribution may then be determined using the size data of Laws and Parsons (1943) together with the raindrop fall velocity measurements of Laws (1941). The results are shown in Figure 10. The drop sizes considered varied in radius from 0.0625 to 3.25 millimeters. The phase function and scattering efficiency of each individual drop size is computed using Mie theory assuming that the drops are pure water with a refractive index of $1.332 - 1.44 \times 10^{-8}i$. The composite phase function and cross section of the rain is found by averaging over the rain drop size distribution function. The composite phase function and cross section are then used in Eqs. 10, 12 and 14 to compute transmission. The predicted transmission is graphed as a function of rain rate in Figure 11.

A linear relation between the logarithm of the extinction at wavelengths around 10 micrometers and the liquid water content of fog has been shown by Chylek (1978), Pinnick, et al (1979), and Carradini and Tonna (1981). Such a relation may be explained by examining the dependence of the extinction efficiency factor Q_E on the size parameter. As shown in Figure 12, the efficiency factor at a wavelength of 10.6 micrometers may be approximated as a straight line out to a size parameter of 8.0 corresponding to a fog droplet with a radius of 12.7 micrometers. Fog drop size distributions are dominated by particles of radius less than 7 micrometers (Pinnick, et al, 1979; Carradini and Tonna, 1981; Roach, et al, 1976; Pinnick, et al, 1978). Using the relation

$$\sigma_E(\lambda,r,m(\lambda)) = Q_E(\lambda,r,m(\lambda))\pi r^2 = C(\lambda)r^3 \qquad (15)$$

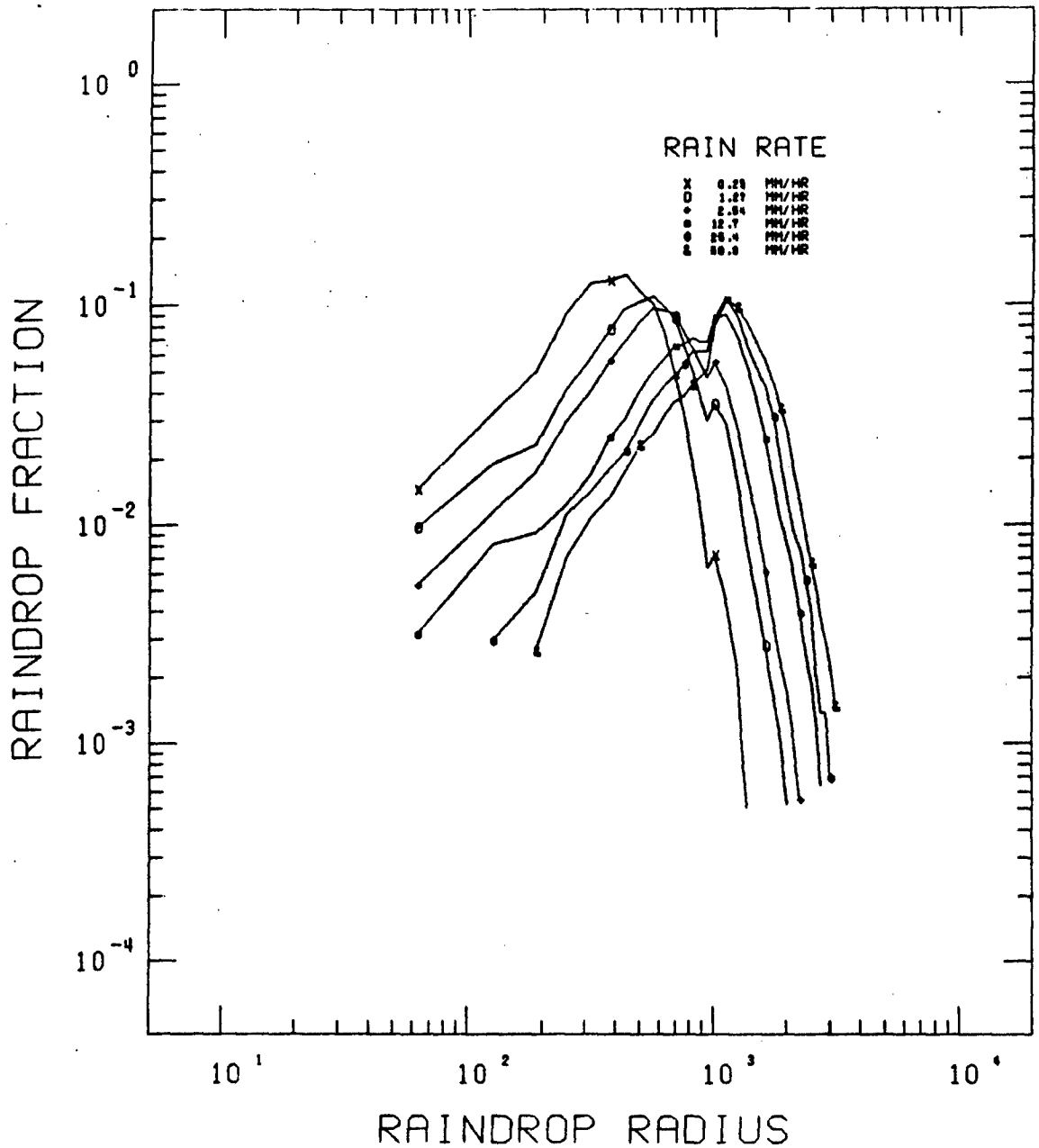

Figure 10. Fraction raindrop size distribution.

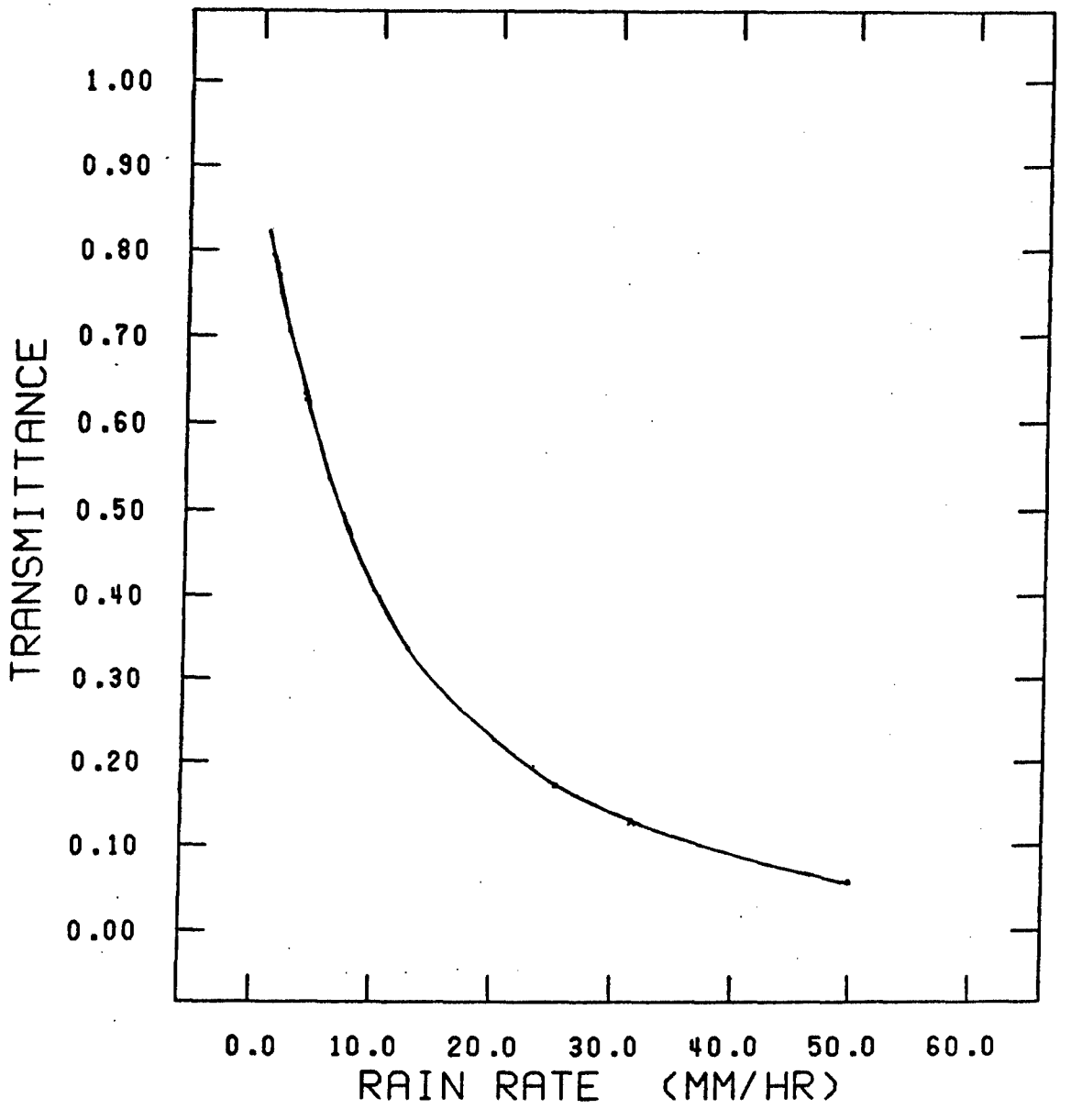

Figure 11. Predicted attenuation of 0.6328 micrometer radiation by rain. The model assumes the raindrops to be spheres of pure water.

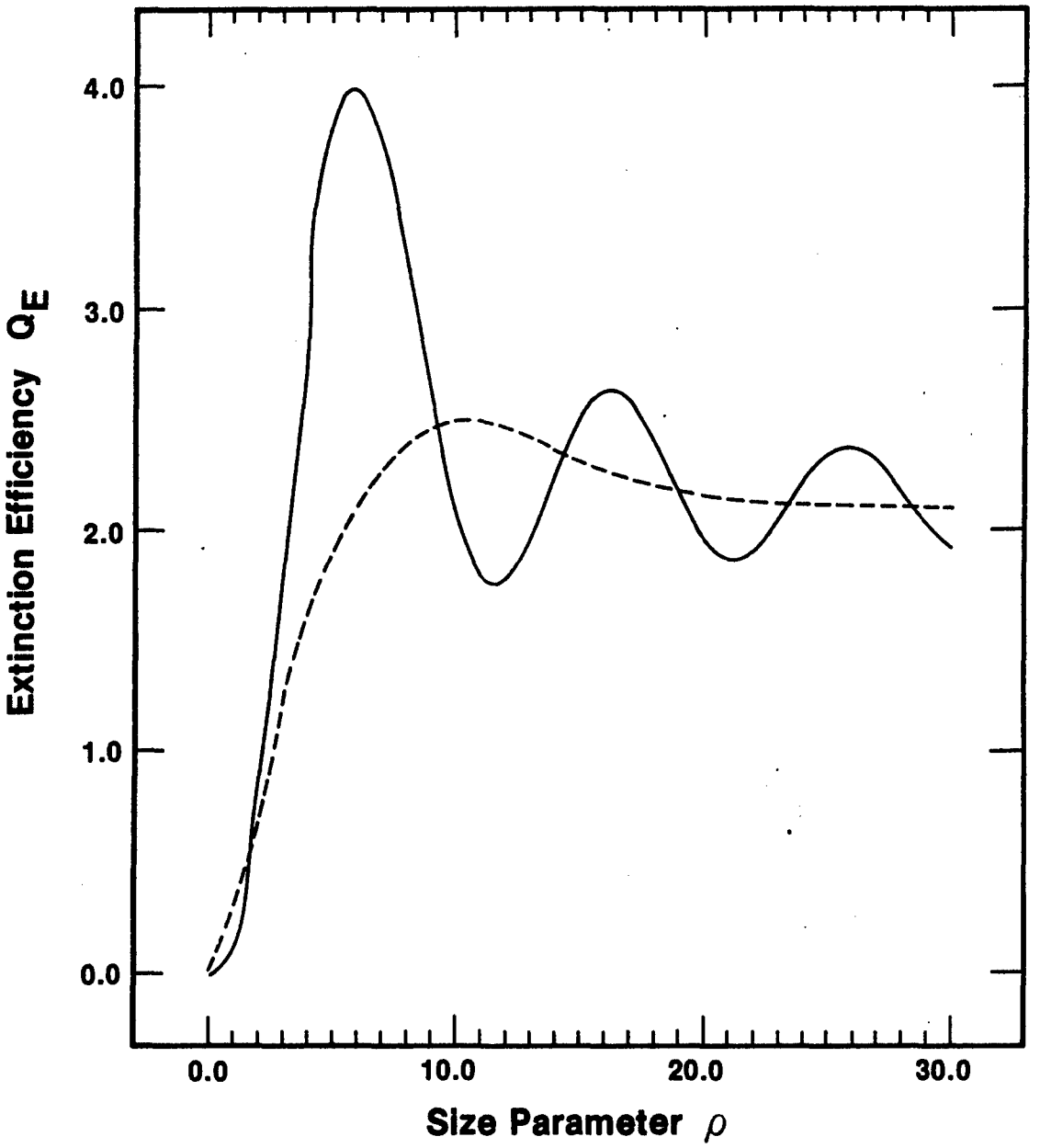

Figure 12. Extinction efficiency as a function of size parameter. Computations were made for spherical water drops using Mie theory.

where $C(\lambda)$ is the slope of the curve in Fig. 12 for size parameters less than 8.0, the extinction coefficient in the 8 to 12 micrometer band may be written

$$\beta_{8-12}(t) = \int_{8}^{12} C(\lambda) \int_{0}^{12.7} n(r,t) r^3 dr \, d\lambda \qquad (16)$$

where the total number of fog particles per unit volume is given by

$$N(t) = \int_{0}^{\infty} n(r,t) dr \qquad (17)$$

The inner integral in Eq. 16 is proportional to the liquid water content of a fog described by the drop size distribution $n(r,t)$. Consequently, the extinction in the 8 to 12 micrometer region can be directly related to the liquid water content of the fog. A similar relation between extinction efficiency and the size parameter exists at a wavelength of 0.6328 micrometers for fog drops of radius less than 1.0 micrometer. Because fogs contain a significant number of drops with radii greater than 1.0 micrometer, the extinction coefficient in the visible region is a function of both the particle size distribution and the liquid water content of fog. As a fog forms and dissipates, the liquid water content increases then decreases, but the drop size distribution $n(r,t)$ does not retrace its evolution in time, so the path of the data points on the log-log plot does not retrace its steps. A linear model may be a good approximation for the dependence of β_{IR} on β_{VIS} for any single fog process, but only if measurements are made on a time scale short compared to fog lifetimes. However, a single line cannot represent the relationship between β_{IR} and β_{VIS} for fogs in general, because differences in $n(r,t)$ cause a large variation in β_{VIS} for any given liquid water content.

EXPERIMENTAL FACILITY

A sheltered outdoor transmission range has been established at KRC, along with facilities to monitor appropriate weather parameters. The range incorporates a folded path, in which radiation goes from the outdoor source out a window to a plane mirror at 500 meters, and is reflected back to the receiver, which is located indoors near the source. The optical arrangement is shown schematically in Figure 13. The advantage of this arrangement, as compared to a straight path, is that all the electronics are at one end, making calibration, maintenance, and temperature control relatively easy.

Visible transmission is measured by using a Helium-Neon laser as a source. The laser emits 0.6 mW CW, is mechanically chopped at 900 Hz, and is aimed at the mirror with no collimating optics. The receiver for the laser is based on cassegrain optics 20 cm in diameter with an 11-milliradian angle of acceptance. The detector is silicon and it is fitted with a narrowband filter centered at the laser wavelength, 0.6328 micrometer. The detector output is fed into a phase-sensitive amplifier, along with a chopper reference signal. The laser and chopper are shown in Figure 14, and the receiver optics are shown in Figure 15.

Near infrared transmission is determined using a neodymium doped YAG laser as a source of radiation at a wavelength of 1.06 micrometers. Because of range safety regulations, the laser output is attenuated to 1.0 milliwatt before exiting the laboratory. The beam is mechanically chopped at a frequency of 400 hertz and aimed at the mirror without any collimating optics. A Cassegrain telescope 15 cm in diameter with a 4-milliradian field of view is used as a receiver. A silicon detector is mounted at the focal point. The detector output is fed into a pre-amplifier and then into a phase sensitive amplifier together with the chopper reference signal. To guard against errors being introduced into the transmission measurements by laser power

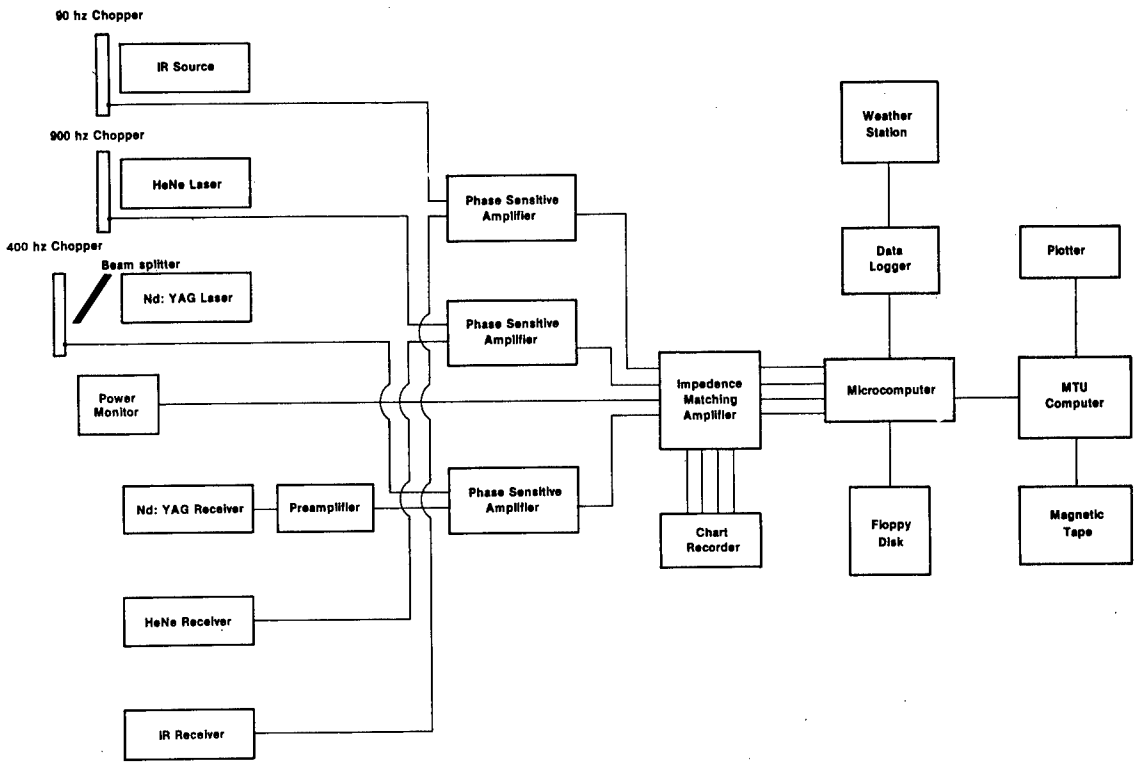

Figure 13. Schematic diagram of transmission laboratory.

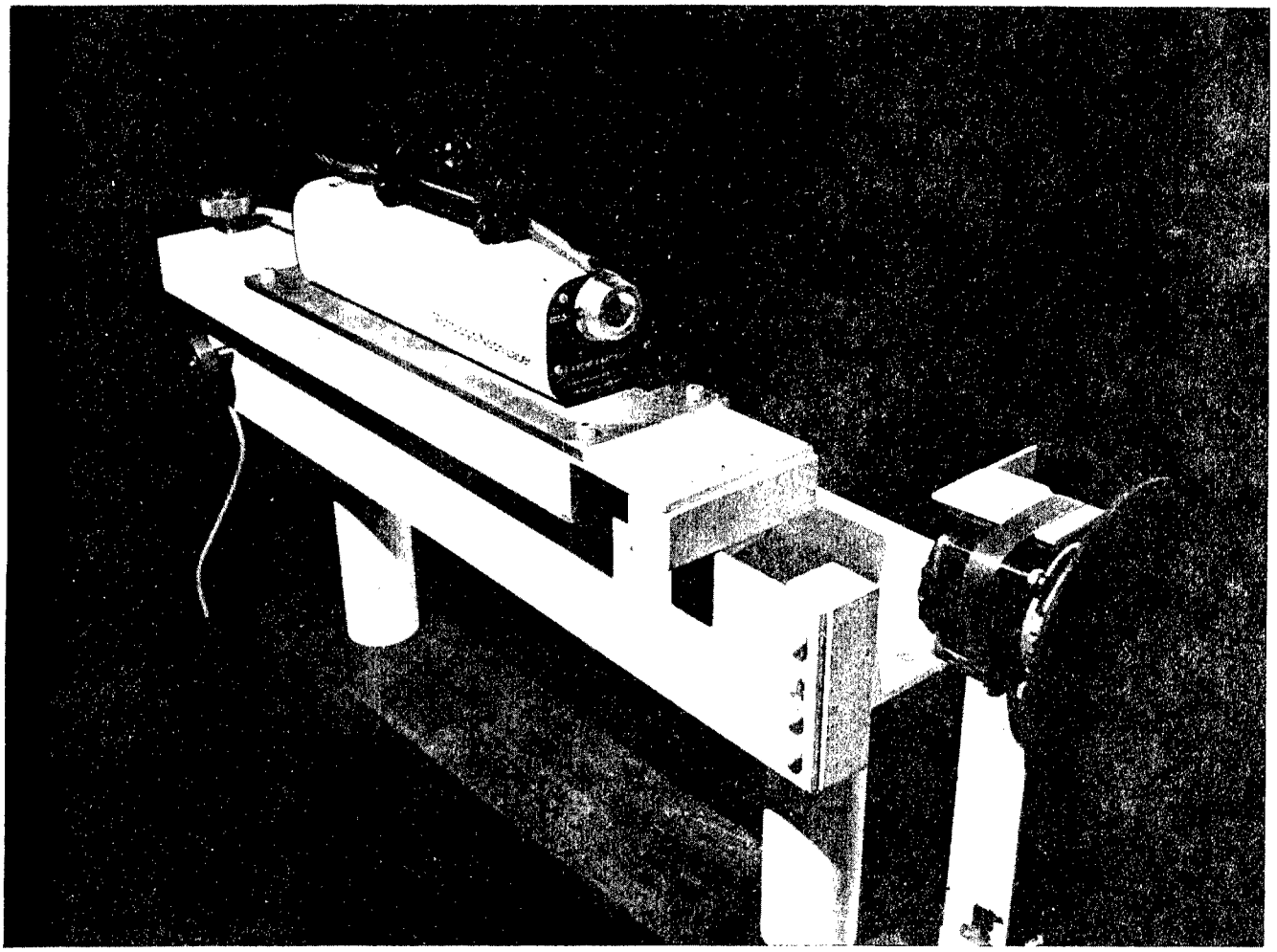

Figure 14. HeNe Laser and Chopper

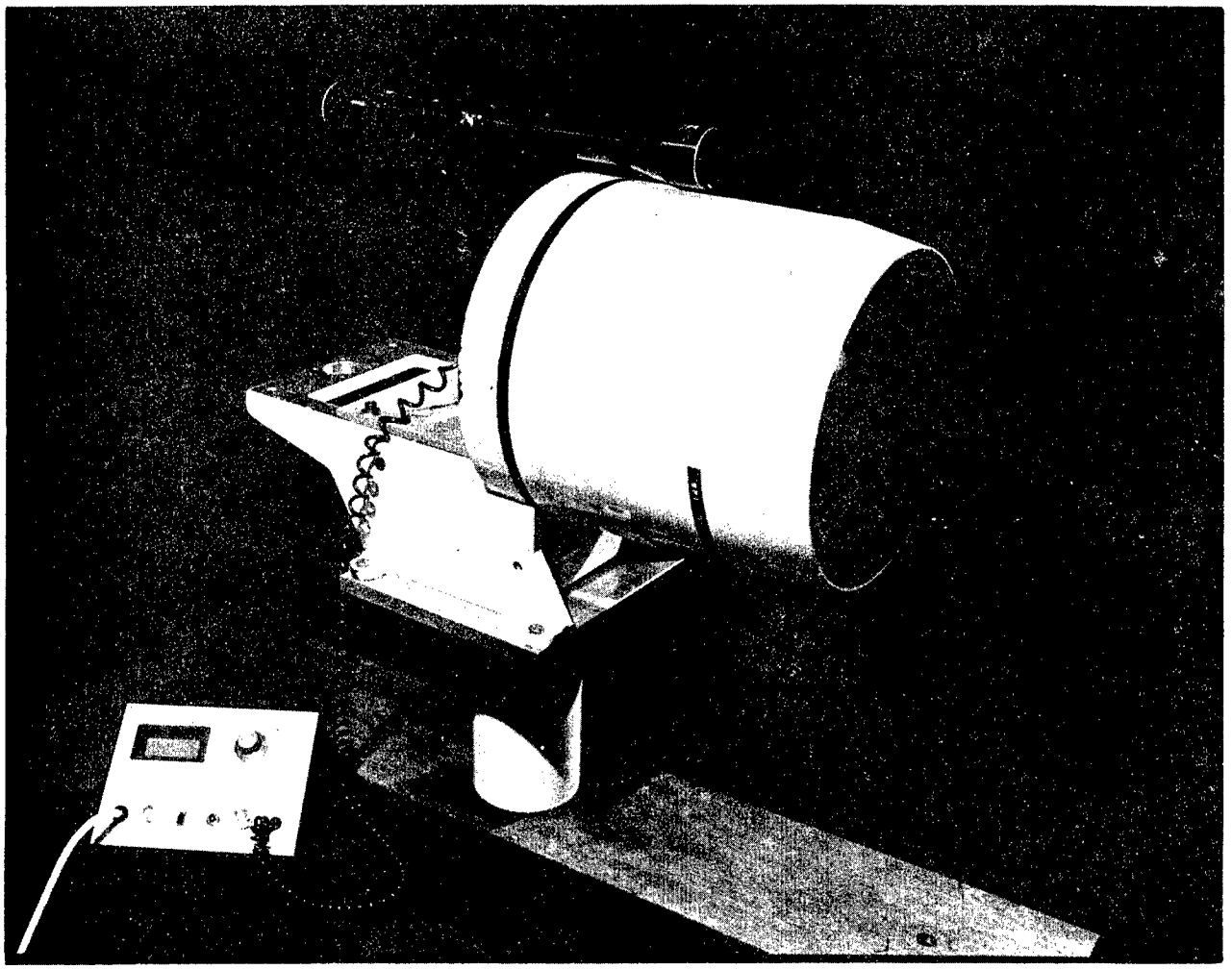

Figure 15. HeNe Receiver

fluctuations, the output of the Nd:YAG laser is continuously monitored. The laser and chopper are shown in Figure 16 and the receiver is shown in Figure 17.

The apparatus used for the infrared measurements is the Barnes Engineering Transmissometer System, Model 14-708, which consists of a source unit, a receiving unit, and a data logger. The source is a temperature controlled black body with chopper and optics, the receiver consists of a 4-inch diameter germanium lens focussing the radiation on a detector, in front of which is one of four infrared filters mounted on a wheel, and the data logger, containing a phase-locked amplifier, provides both digital and analog measures of percent transmission over a one-kilometer path. The source and receiver are shown in Figures 18 and 19, respectively. The Barnes Transmissometer has been modified to change channels under computer control. This enables data collection in both the 3 to 5 and 8 to 12 micrometer bands almost simultaneously.

The mirror which is located 500 meters from the building is 20 cm in diameter, optically flat, and is coated with aluminum plus a protective overcoat. It is in an adjustable mount on top of a steel column anchored in concrete. The mirror is sheltered from weather by a tubular shroud, which is mounted independently of the mirror support column. The sources and receivers are also sheltered from weather, by an extension of the building.

Transmission data is recorded both on strip charts and digitally. The digitizer is controlled by a microcomputer, which also processes the data. Outdoor transmission measurements are modulated by refractive scintillation, which depends on weather conditions in a complicated way. To arrive at a value of transmission typifying a given time interval, the signal is digitized many times, and the individual samples are averaged to obtain the mean value. To record a measure of the size of refractive scintillations, the standard deviation of the samples is also calculated and recorded. Data are

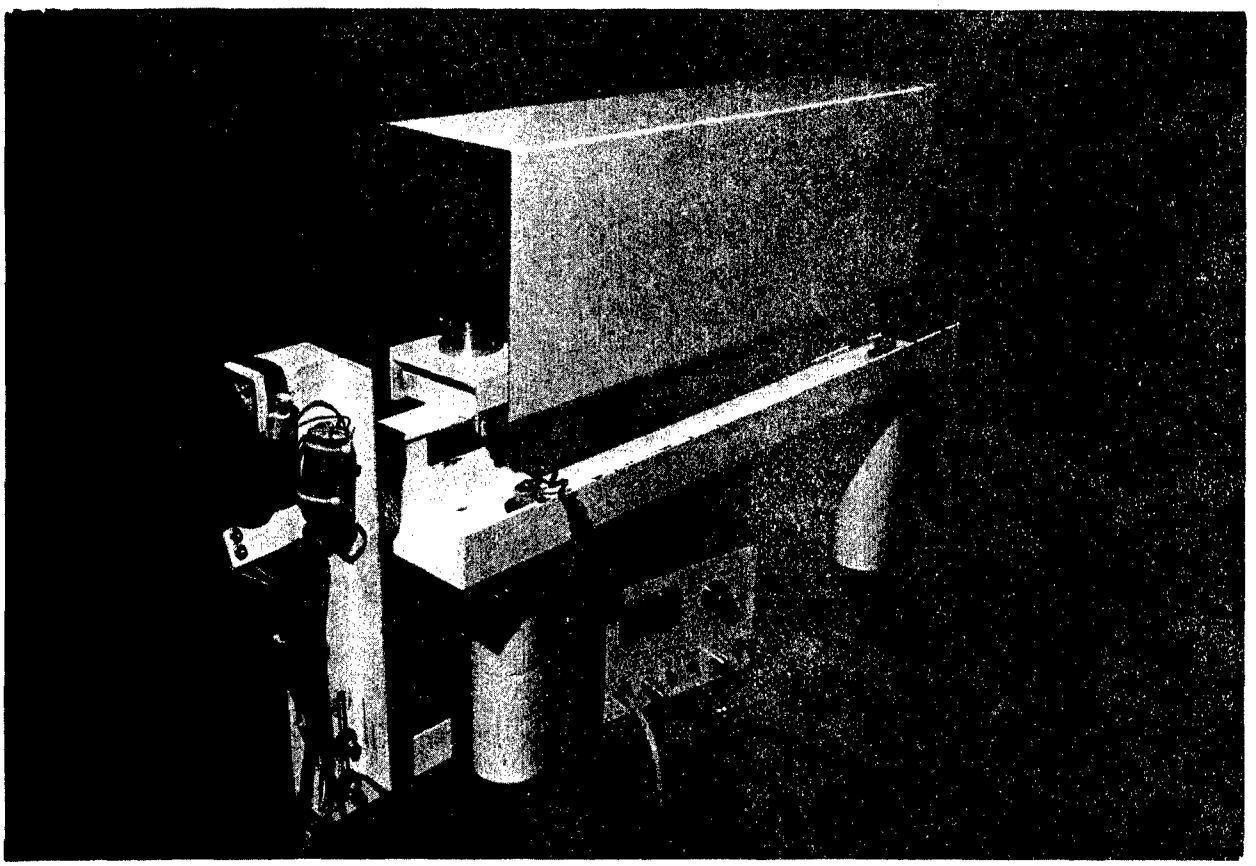

Figure 16. Nd:YAG Laser and Chopper

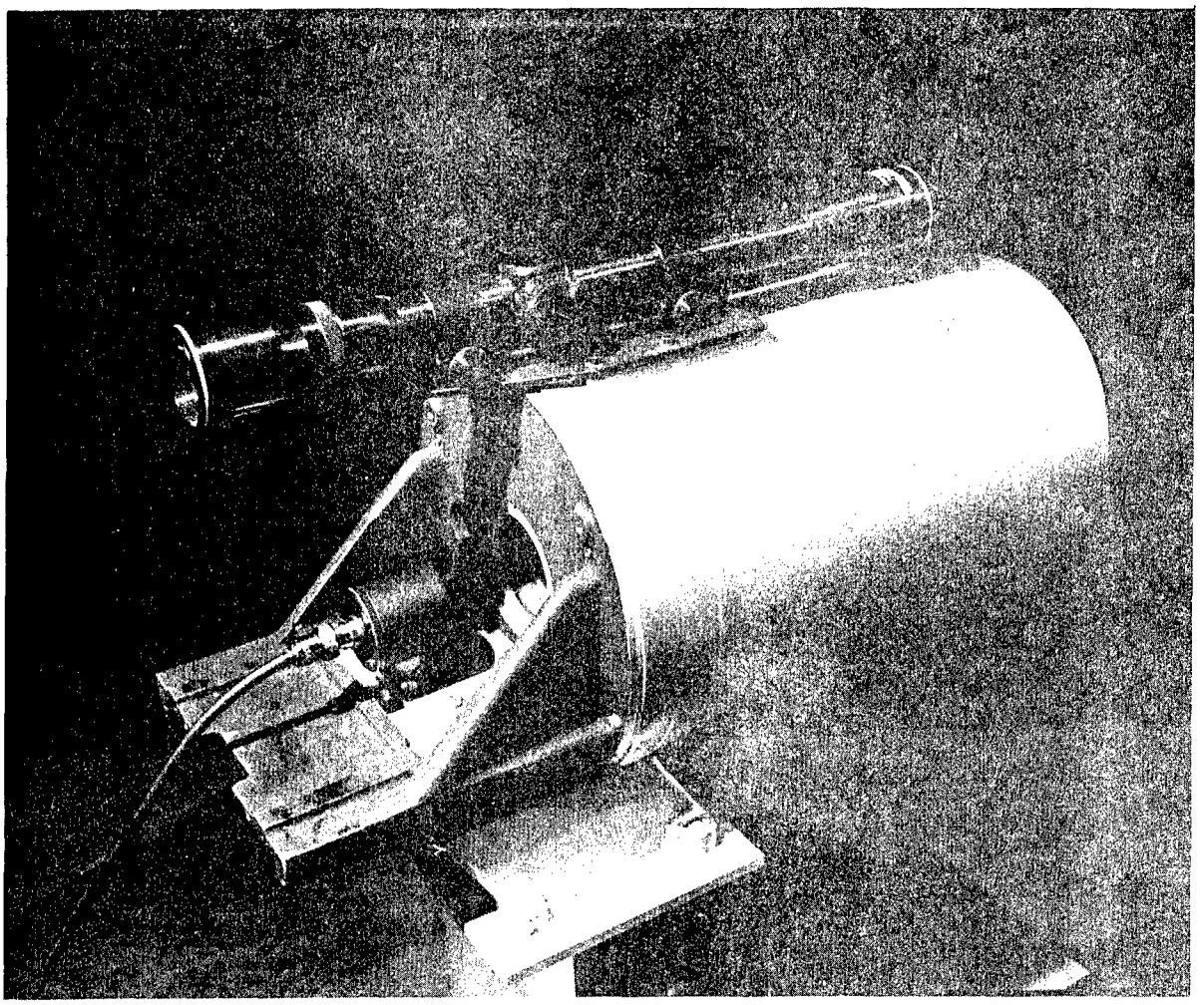

Figure 17. Nd:YAG Receiver

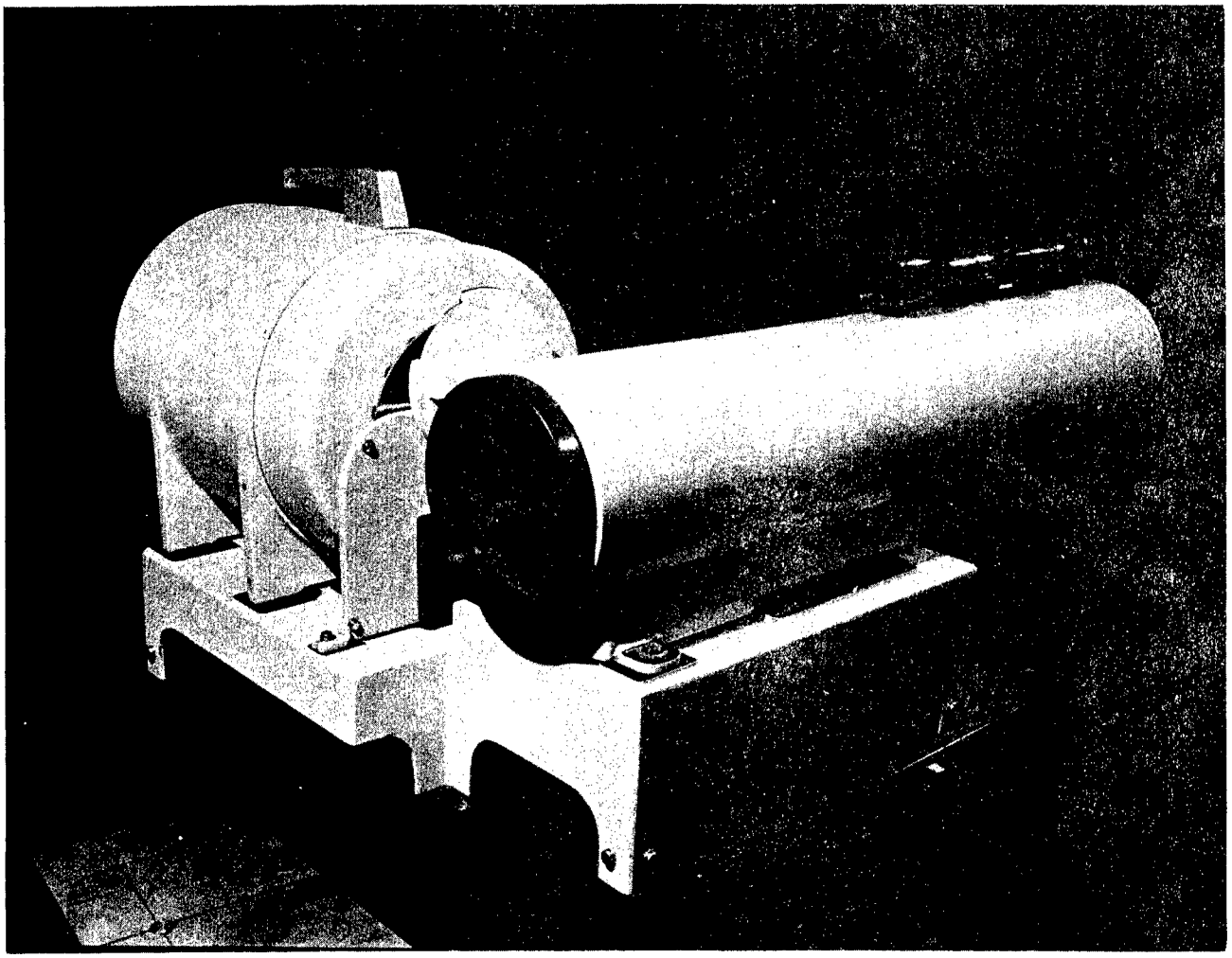

Figure 18. Barnes Transmitter

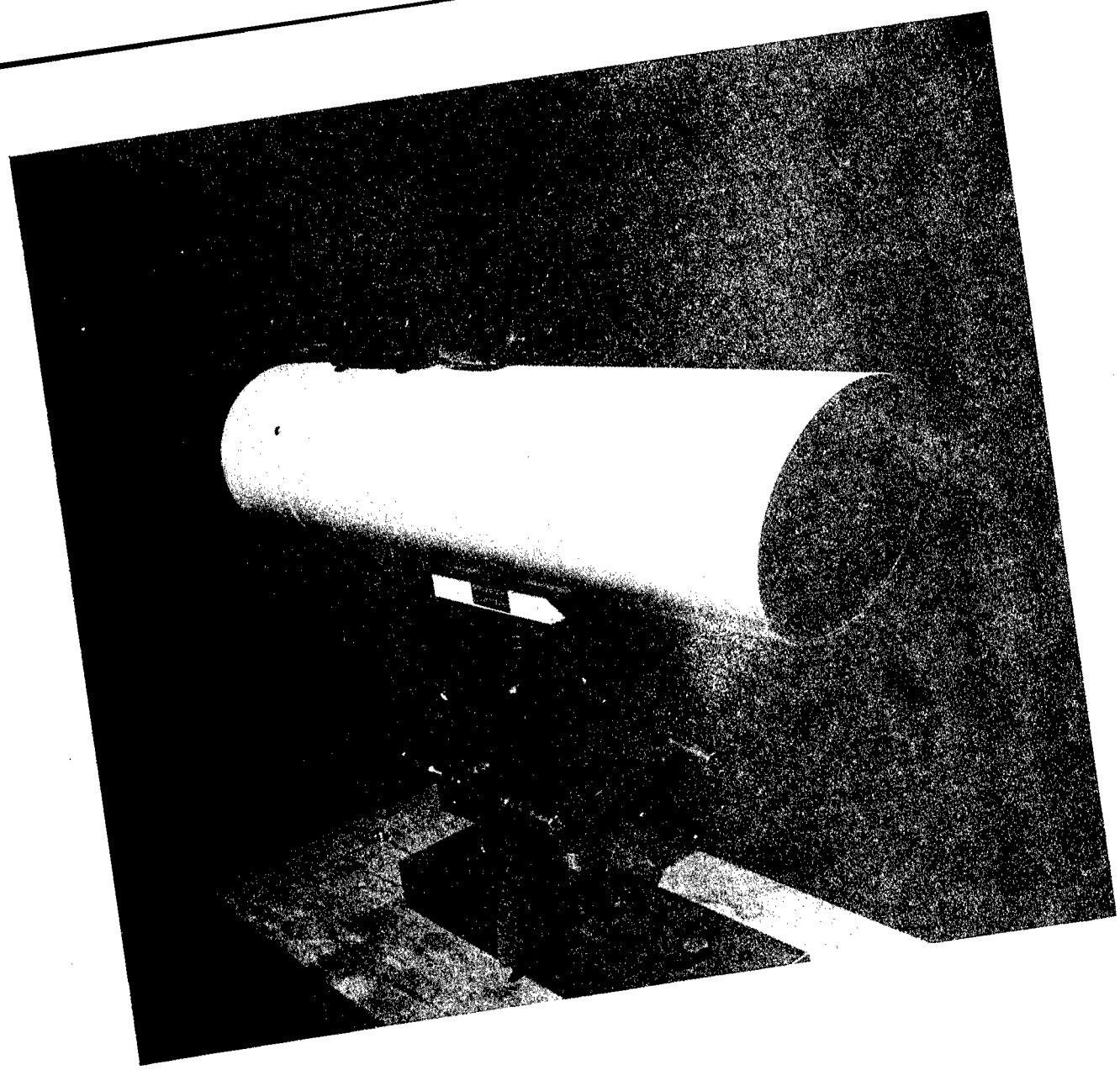

Figure 19. Barnes Receiver

then stored on a floppy disk, and can be examined later on a video display, in a transmission-versus-time format which simulates a strip chart. Interesting time intervals are then further analyzed and plotted on a digital plotter. The microcomputer system has been interfaced to the Michigan Technological University's UNIVAC 1100/80 computer. The data files are transferred to the UNIVAC for further processing and storage.

Weather data are necessary to characterize the path during field experiments. For this purpose, a weather station (shown in Figure 20) has been established at KRC, which automatically records the parameters listed in Table 1 in a digital format, at pre-set time intervals. Besides the standard weather variables, it will be necessary to characterize falling snow for future experiments. This task will be accomplished in two ways: by the use of replicas, and by photographing crystals caught in black trays. Snow crystals will be divided into six main categories (needles, plane dendritic, spatial dendritic, graupel, powder snow, and crystals with droplets) and a given snowfall will be characterized by the size statistics of each category.

A polar nephelometer, shown in Figure 21, has been constructed at the Keweenaw Research Center to measure the phase function of various types and sizes of particles. A Helium-Neon laser operating at a wavelength of 0.6328 micrometers is used as a light source and two photomultiplier tubes mounted on movable arms are used as detectors. Snow crystals are brought through a vertical chute leading from the roof to the scattering volume located above the pivot of the two arms by creating a slightly reduced pressure in the laboratory. The rate at which particles are brought into the scattering volume is controlled by regulating the pressure gradient between the room and the outside. Scattered light is collected by a lens placed in front of each photomultiplier and focussed onto the photocathode. The reference arm is placed at an angle 15° while the measurement arm is used to measure the phase

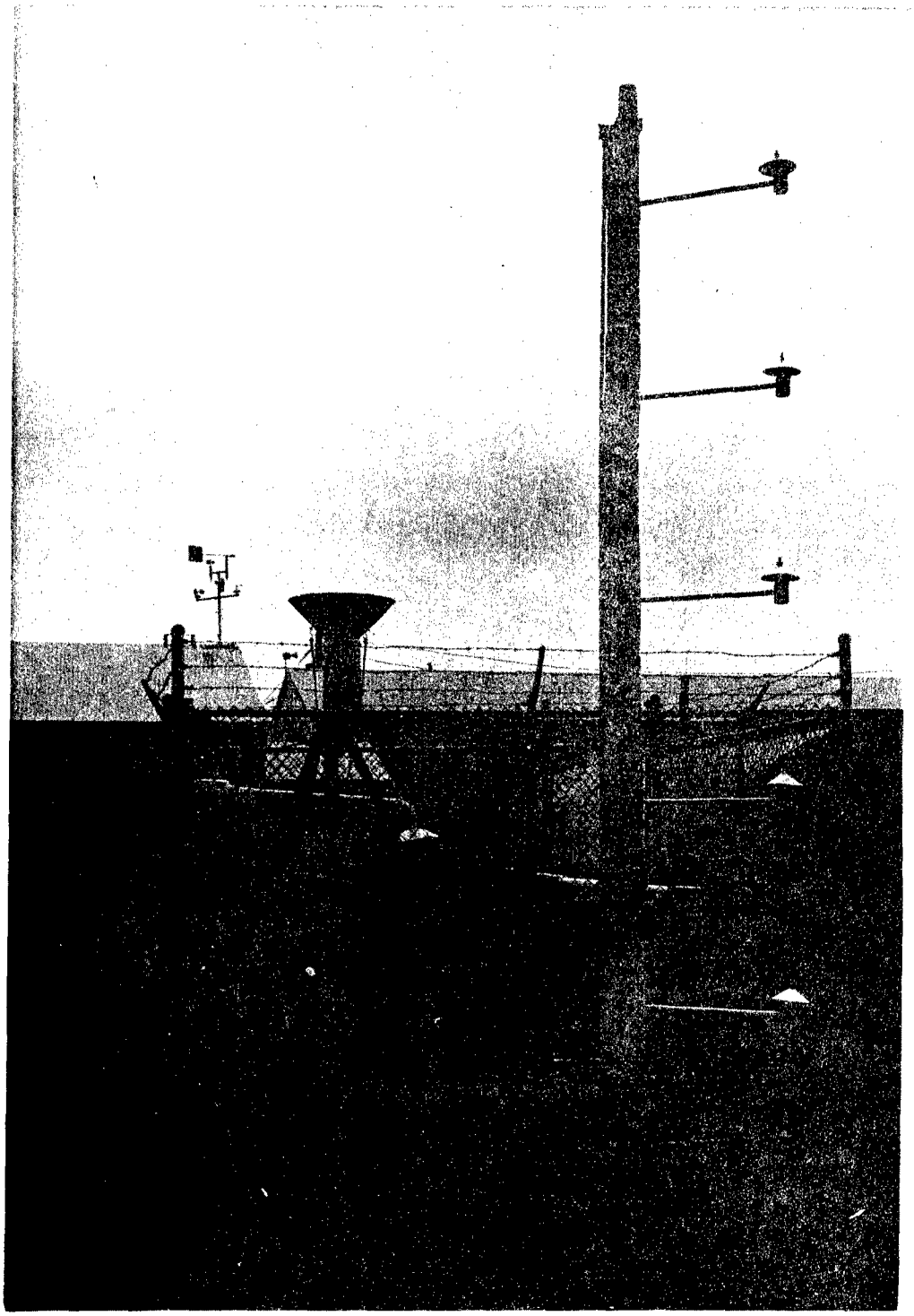

Figure 20. Weather Station

Table 1. KRC Weather Station

Weather Parameter	Measuring Instrument
Air Pressure	Analog Output Barometer
Air Temperature	Thermocouple
Air Temperature Gradient	Series of Thermocouples
Asphalt Temperature	Thermocouple
Fog	Visiometer
Ground Temperature	Thermocouple
H_2O Vapor Density	Optical Dewpointer
Net Solar Load	Radiometer
Rainfall/Snowfall	Tipping Bucket
Smoke & Dust	Nephelometer
Wind Direction	Wind Vane
Wind Speed	3-Cup Anemometer

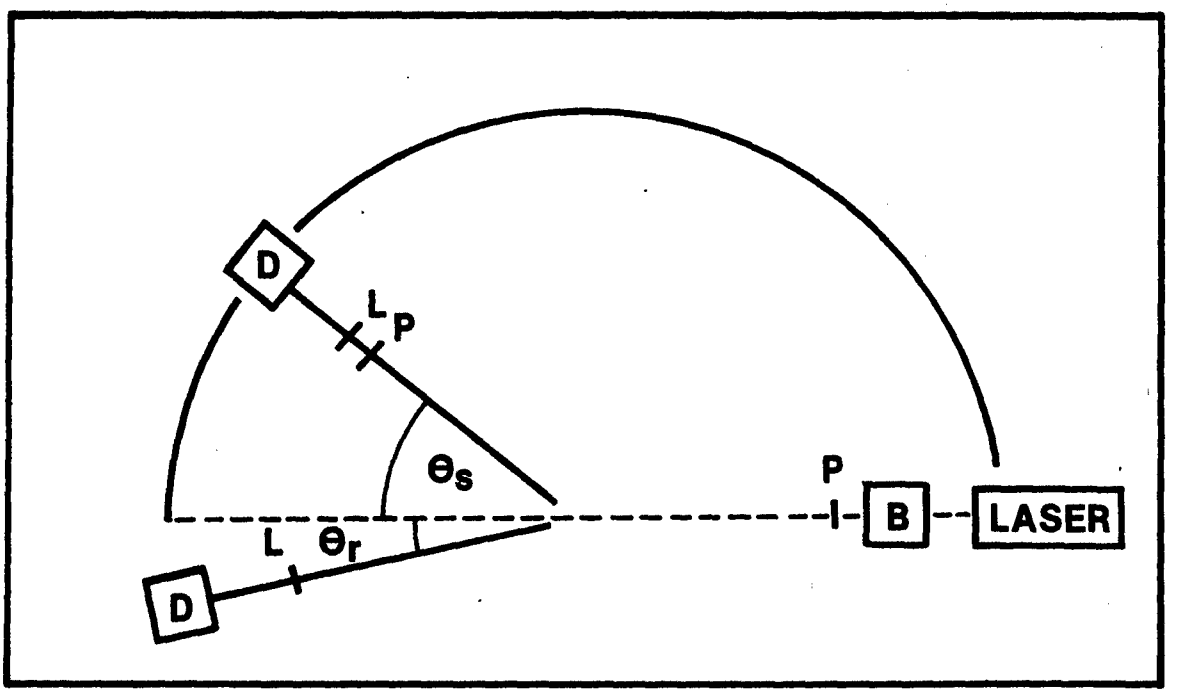

Figure 21. Polar Nephelometer. The laser beam is expanded by a beam telescope (B) and encounters the snowflakes at the intersection of the two movable arms. The scattered light is collected by lenses (L) and focussed onto the detector (D). The reference detector is placed at θ_r for the entire experiment while the measurement arm is used to measure the phase function at angle θ_s. Polarization measurements may be made by placing polarizers (P) after the beam telescope and in front of the collection lens on the measurement arm.

function. As a snowflake falls through the laser beam, a pulse is observed at the output of each phototube. Coincidence of pulses from both the reference and measurement phototubes is used to ascertain that the snowflake did pass through the scattering volume and not a part of the laser path visible to only one photomultiplier. To insure that the snow crystals do not change phase during the experiment, the room is allowed to cool to the outside temperature.

RESULTS

Because water vapor is an absorber of infrared radiation, it is important to know the transmission losses due to water vapor and other atmospheric molecules as a function of temperature, atmospheric pressure, and relative humidity. This is easily calculated with repeated application of LOWTRAN using a filter function comparable to those of the Barnes transmissometer. The results are plotted as a function of temperature in Figure 22 for the 3 to 5 micrometer region for various values of the relative humidity at an atmospheric pressure of 1000 millibars. Similar curves are obtained for other values of the atmospheric pressure. A maximum attenuation of 34% is obtained at a temperature of 34°C and a relative humidity of 100%. A more dramatic decrease in transmission with increasing relative humidity is seen in the 8 to 12 micrometer band as shown in Figure 23. An attenuation of 76% is predicted for a temperature of 35°C and a relative humidity of 100% at an atmospheric pressure of 1000 millibars.

The attenuation of Helium-Neon laser radiation of wavelength 0.6328 micrometers by rain has been measured as a function of rain rate (Winchester et al., 1982). Both transmission and rainfall were averaged over 1-minute intervals. The results are shown in Figure 24 superimposed on the theoretical

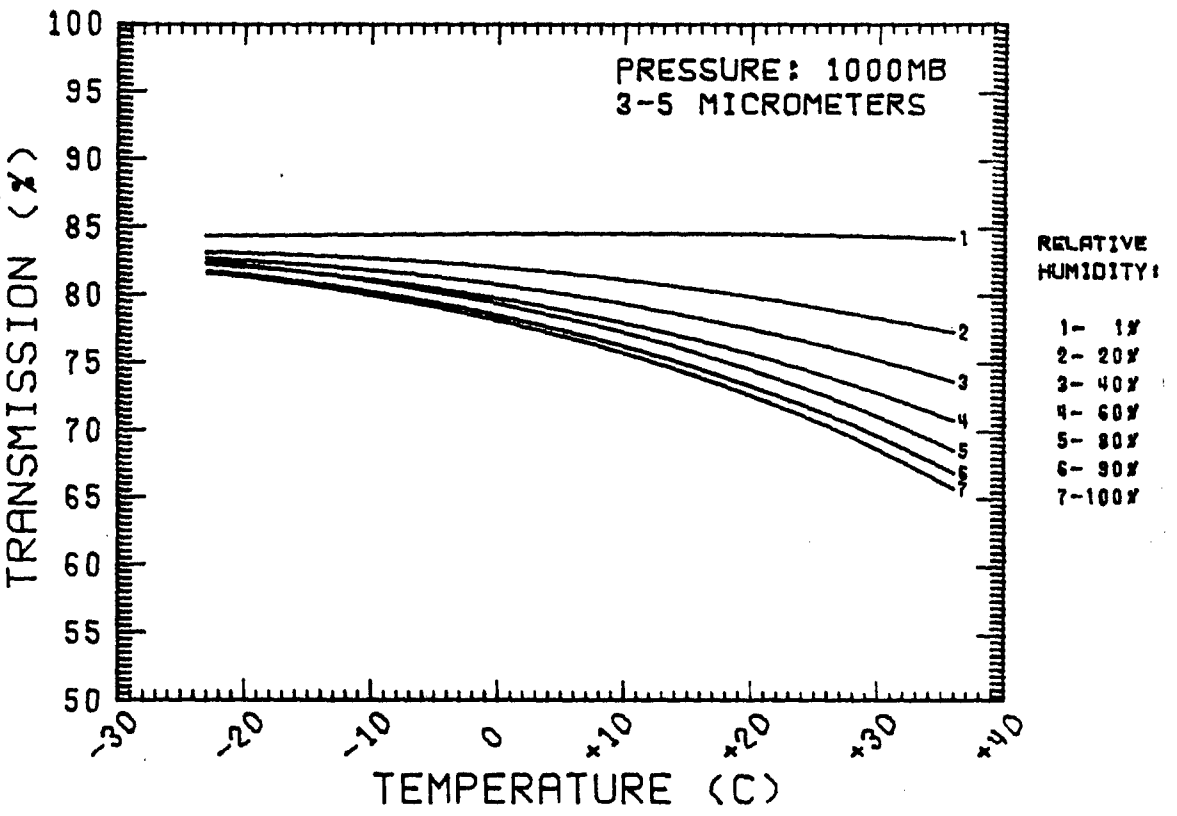

Figure 22. Predicted transmission in the 3 to 5 micrometer band. The curves were obtained using LOWTRAN for clear air.

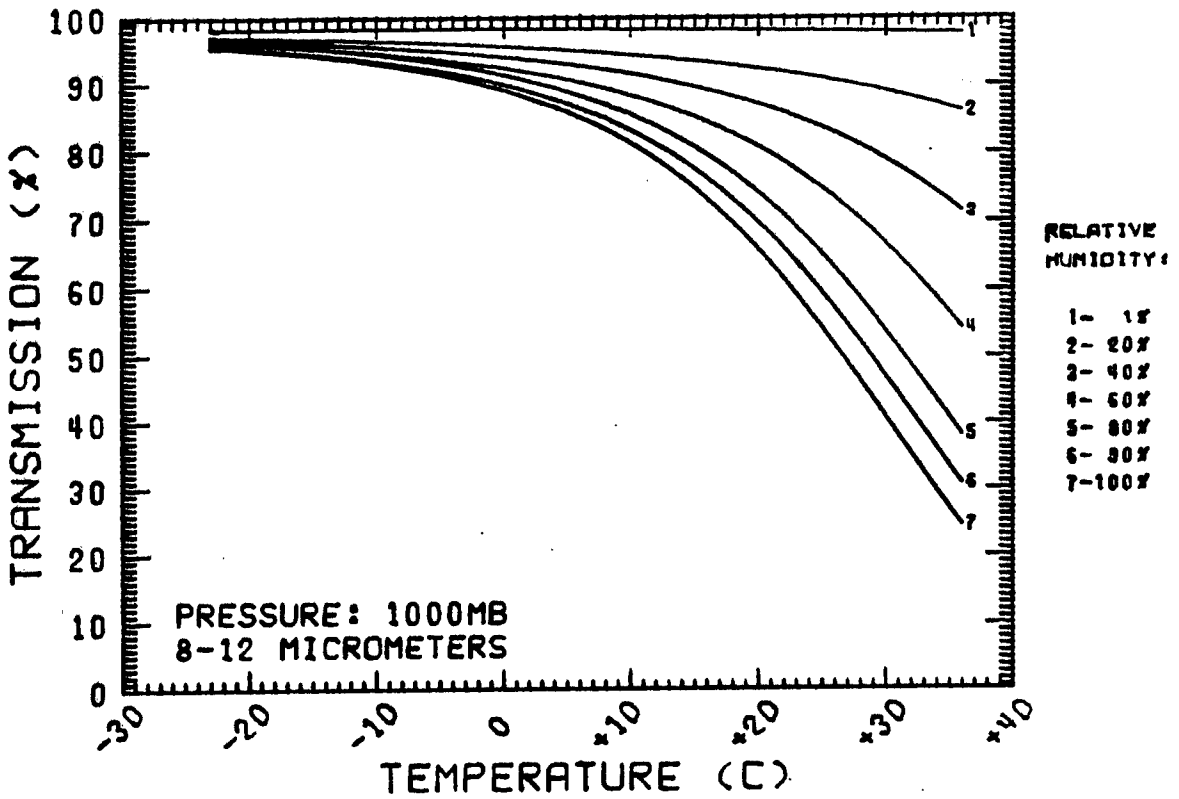

Figure 23. Predicted transmission in the 8 to 12 micrometer band. The curves were obtained using LOWTRAN for clear air.

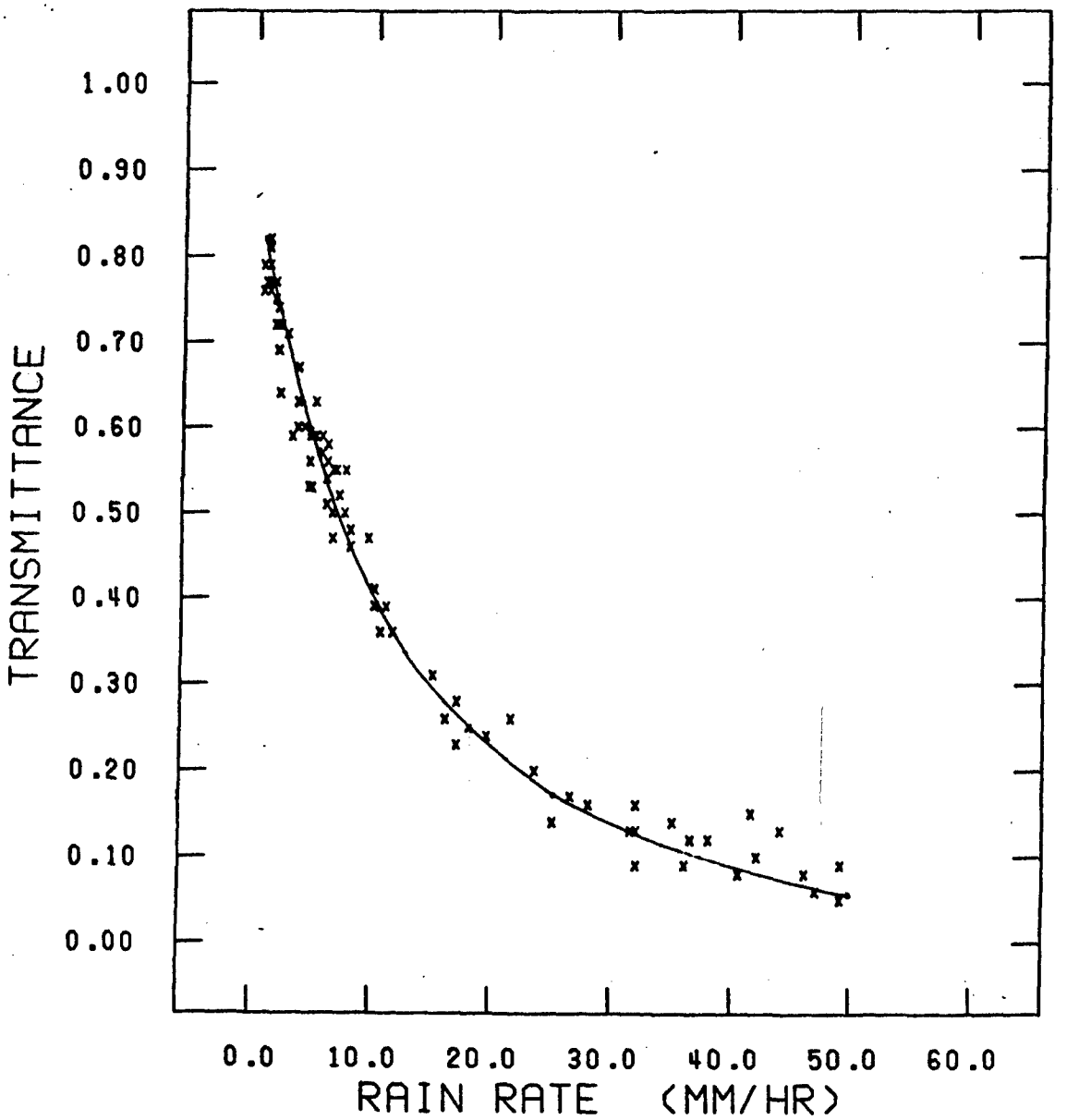

Figure 24. Comparison of experimental data and theoretical model for extinction of 0.6328 micrometer radiation by rain. The data were collected and averaged over 30-second intervals.

curve described previously. The agreement between the model and experiment is quite good for rain rates greater than 10 millimeters per hour. At rain rates less than 10 millimeters per hour, good agreement between theory and experiment is obtained only if the lower rainrate occurs initially or is immediately preceded by a period of intense rain. After a period of constant rain at rates less than 10 millimeters per hour, the experimentally measured value is much less than the predicted value. This is attributed to the suspension or near-suspension of some of the very small drop sizes associated with low rain rates in the atmosphere.

In order to develop a similar model for attenuation of visible laser radiation by snow, it is necessary to know the phase function and the absorption and scattering cross sections of snowflakes of different shapes and sizes. A model for the phase function of snow needles has been developed (Winchester, 1982a and b) and found to be in good agreement with previously measured data (Winchester et al., 1981). The phase function of natural snow crystals was measured during an intense snow storm on November 15, 1980. The measurements were made with unpolarized light since a complete set of polarized measurements would require at least four hours. Data were taken between 10° and 170° in 5° intervals. At each scattering angle, a minimum of 51 events were recorded. Ice crystals were collected and examined after every fourth set of phase function measurements. The crystal size and shape remained constant during the two-hour experiment. The crystals were needles with an average length of 2.1 millimeters and an average radius of 0.125 millimeters corresponding to a size parameter of 1266. Very little riming was observed. Comparison of crystal size and shape measurements in the laboratory and outside showed the system which delivered the crystals to the scattering volume had no effect on crystal size or shape. The needles fell with their axes oriented in a vertical direction.

The phase function of the snow needles shown in Figure 25 has four distinct features: a forward scattering peak, two broad lateral scattering structures between 70° and 115° and between 115° and 150°, and a backscattering region at angles greater than 150°. The phase function values were determined by averaging the measurements at each scattering angle and then normalizing at 10°. The standard deviation at each point is plotted as an error bar. The phase function in Figure 25 shows a deeper minimum and less lateral scattering than the measurements of Huffman and Thursby (1969). This is consistent with the snow crystals observed in this study being much larger than the artificial ice crystals used in all other studies as more energy goes into forward scattering for larger particles. A broad backscattering feature present at angles greater than 145° may contain an icebow.

As several investigators (Huffman and Thursby, 1969; Huffman, 1970; Dugin et al., 1977) have reported, Mie theory cannot be used to describe the phase function. Liou (1972a) has developed a straightforward method for computing scattering from circular cylinders. Using this method the phase function of a circular cylinder of ice with a complex refractive index $m = 1.332 - 1.44 \times 10^{-8} i$ was calculated at a wavelength of 0.6328 micrometers. The wavevector of the incident radiation was assumed to be perpendicular to the cylinder axis and the scattered intensities were summed over all possible polarization combinations. The resultant, shown in Figure 26, has been averaged over a 5° collection angle and normalized at 10°. The exact calculation using the method of Liou (1972a) predicts much more scattering between 10° and 40° and icebows at 143° and 168°. The computed phase function has some structure between 70° and 130°, but it does not match the structure shown by the data. The general intensity level of the lateral scattering does agree with experiment as does the intensity of backscattering near 160°.

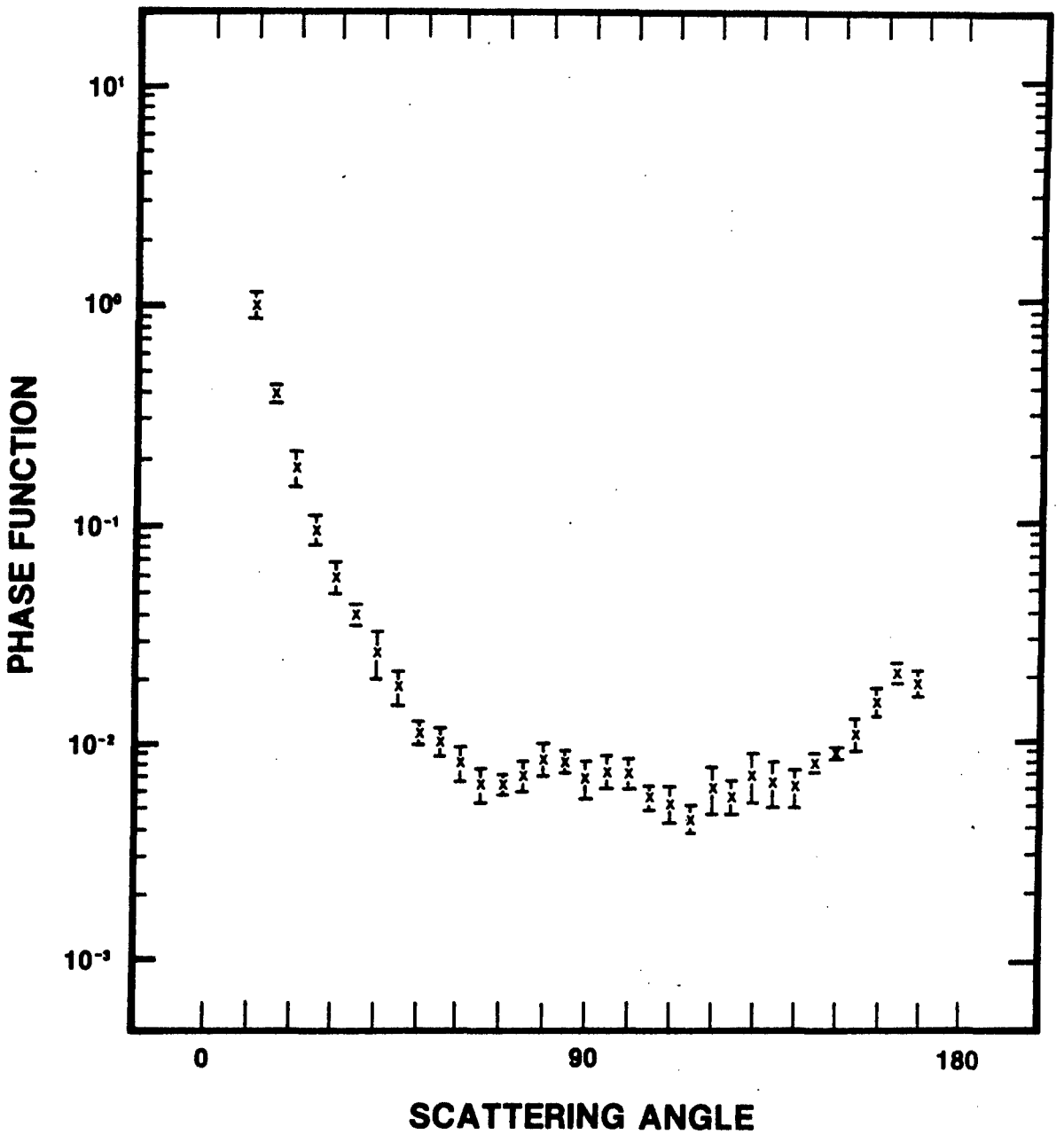

Figure 25. Phase function measurements of snow needles normalized at 10°. The crystals averaged 2.1 millimeters in length and 0.125 millimeters in radius.

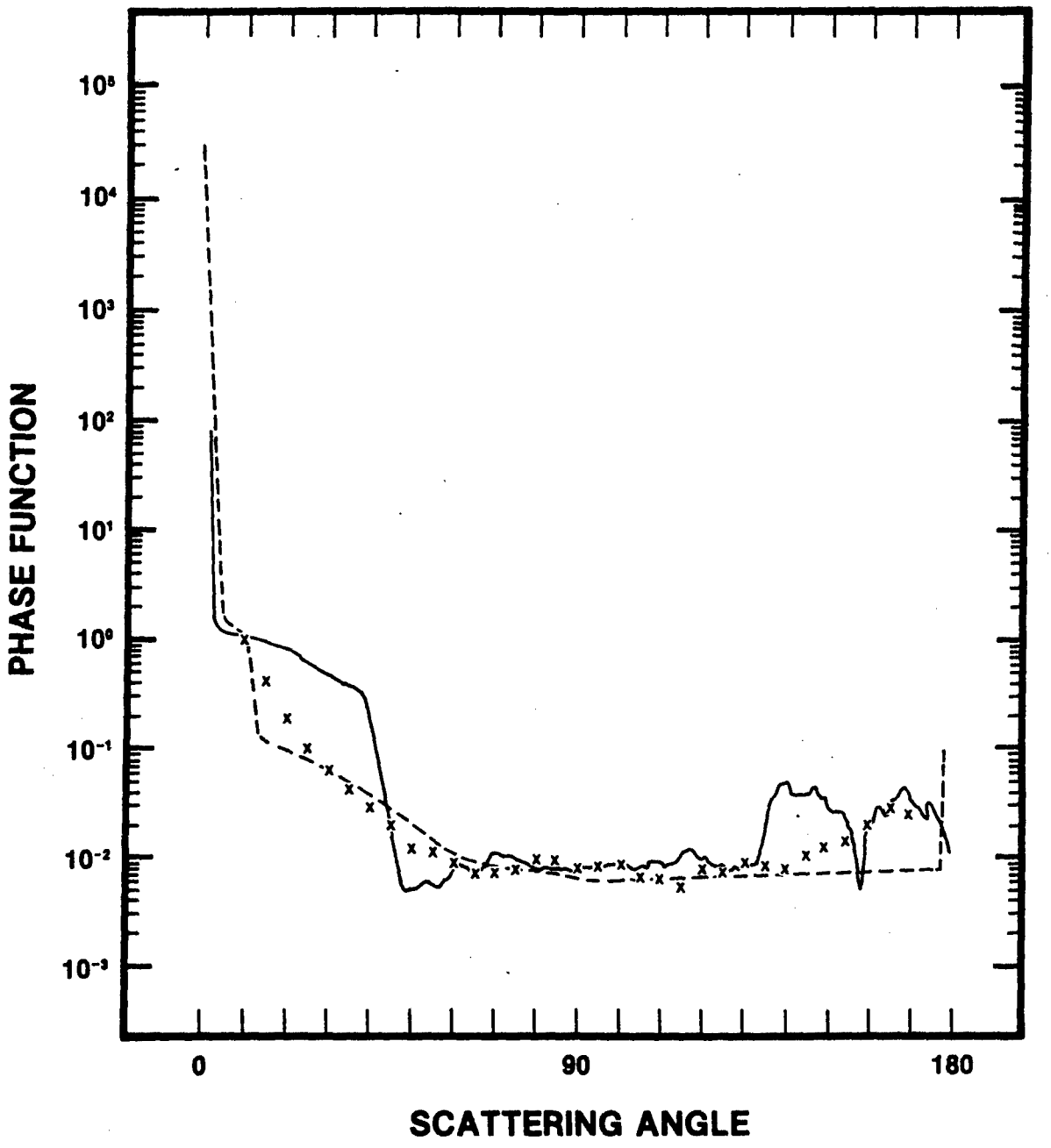

Figure 26. Comparison of experiment with calculated phase functions. Scattering from circular cylinders was computed using the method of Liou (1972a) while the geometric optics approximation sums the diffracted, reflected, and refracted components.

Several ray tracing methods have been reported for hexagonal platelets and hexagonal columns (Jacobowitz, 1971; Wendling et al., 1979; Liou and Coleman, 1980). These methods follow the internal path of a ray inside the ice crystal for up to six internal reflections. Since natural ice crystals such as snow are formed by successive deposition and scavenging it is reasonable to assume that each crystal is made up of many small domains. In the case of needles, some of the domains may be annular, resembling the rings of a tree. There is considerable scattering and absorption of light, as well as polarization scrambling, at the domain interfaces. This can explain the difference between the measurements of depolarized light components and computed values of Fresnel coefficients observed by Sassen and Liou (1979a and b). A ray tracing model for a circular cylinder oriented with the cylinder axis vertical was used to obtain a geometric optics solution for the phase functions. The method follows each ray path through the crystal and assumes that radiation not exiting the crystal on the first pass is absorbed. The externally reflected and transmitted components are studied for 6000 equally spaced rays incident on the cylinder. A single rectangular diffraction pattern (Born and Wolf, 1970) is then added to give the phase function which has been normalized at 10°. The resultant is shown as the dashed curve in Figure 26. The agreement between the ray tracing solution and the data is quite reasonable at scattering angles less than 140°. In the geometrical optics approximation the backscattering from a cylinder is concentrated near 180° instead of in a broad peak as seen in the data. The broadening of the backscattering is attributed to surface roughness and end effects.

The comparative extinctions at 0.6328 micrometers, 1.06 micrometers, and in the 8 to 12 micrometer bands may be illustrated using GAP-type plots. However, when using

GAP-type plots, it should be remembered that the susceptibility of the receiving optics to scattered radiation influences the extinction coefficient used in these plots. The He-Ne laser receiver has a field of view of 11 milliradians while the Nd:YAG laser receiver has a 4-milliradian field of view. The field of view of the Barnes transmissometer is also 4 milliradians. The effect of field of view on susceptibility to scattered radiation has been discussed previously (Winchester, et al, 1981).

As described previously, attenuation of radiation in the 8 to 12 micrometer band by fog is a function of the liquid water content of the fog while attenuation at 0.6328 micrometers is related to the fog droplet size distribution function. This is shown by the behavior of the infrared and visible extinction coefficients during a period of fog observed on 14 April 1980 (see Figure 27). As the fog formed a linear path is traced out (o) as the liquid water content increases. This process lasted 76 minutes and was sampled at one-minute intervals. The fog then began to dissipate over a 63-minute period (■). During this time interval, the liquid water content of the fog decreased. The fog formation and dissipation extinction data do not lie along the same curve because the particle size distribution function is not a simple function of liquid water content. As the fog again thickened over a 39-minute period, a third path (▲) is parameterized by the two extinction coefficients.

Figures 28 and 29 show the extinction coefficient in the 8 to 12 micrometer band as a function of the extinction coefficient at 0.6328 micrometers for fogs measured on 7 June 1981 and 8 June 1981, respectively. These two graphs are typical of the many fog measurements made during the course of this study. When data from many fogs are graphed on the same plot, the value of the infrared extinction coefficient may range over a decade for a single value of the visible extinction coefficient (Turner, 1980). This problem is

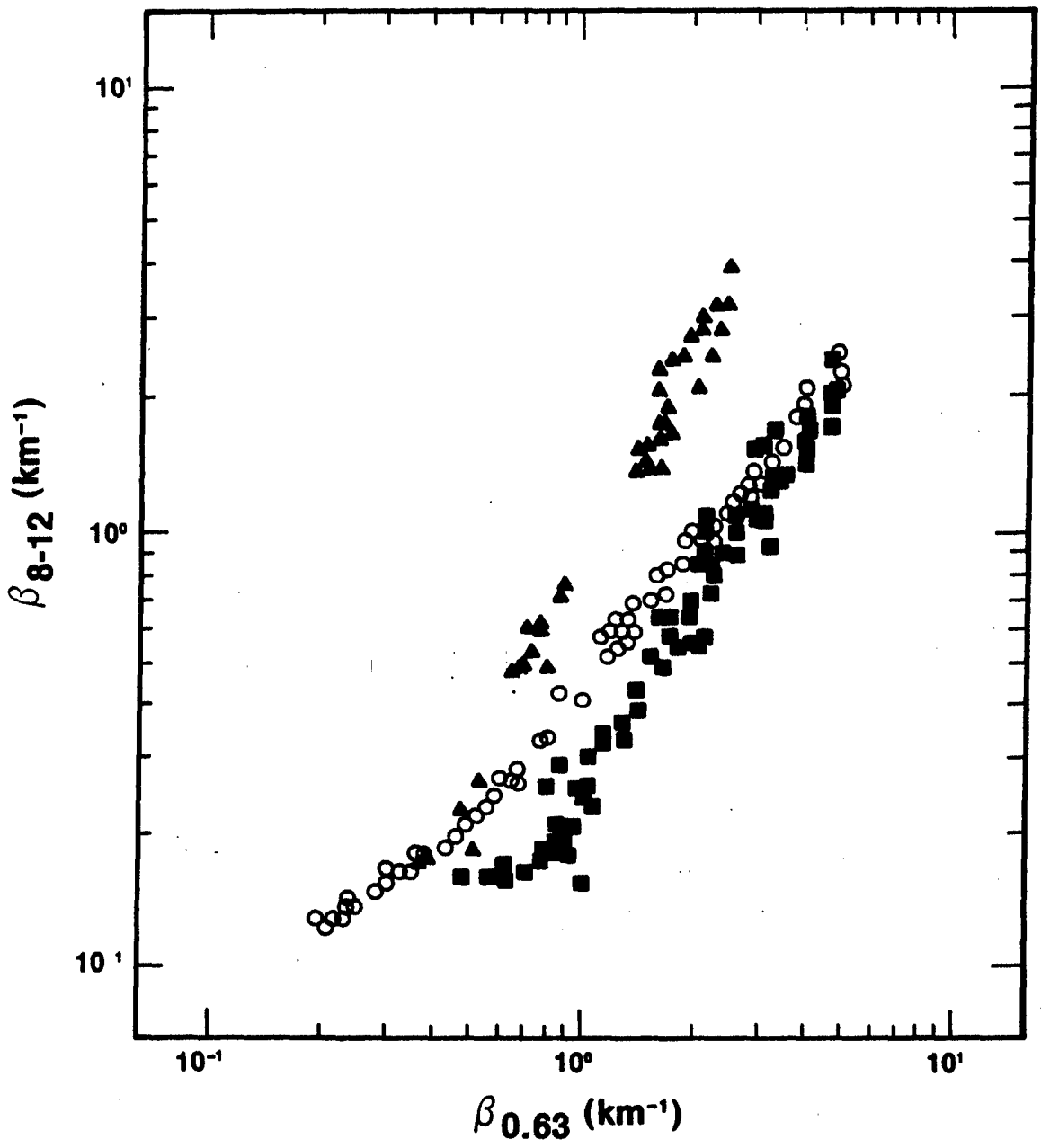

Figure 27. Extinction fog, 14 April 1980. Fog extinction measurements were obtained at one-minute intervals. The extinction coefficient in the 8 to 12 micrometer band is plotted as a function of the extinction coefficient at 0.6328 micrometers. The fog formed over a 76-minute period (O), dissipated over the next 63-minute period (■), and then thickened again (▲) over a 39-minute period.

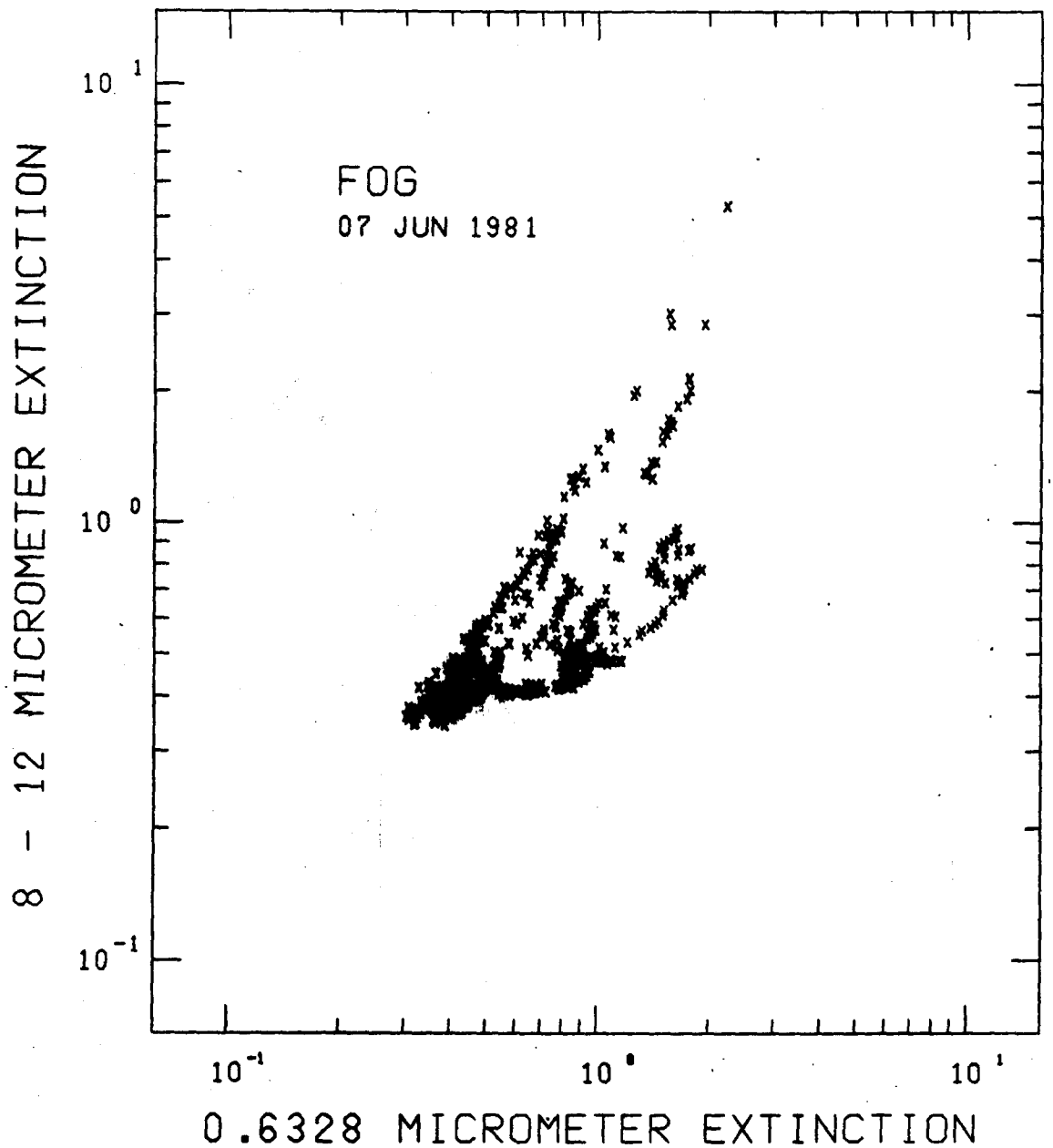

Figure 28. Extinction in Fog, 7 June 1981.

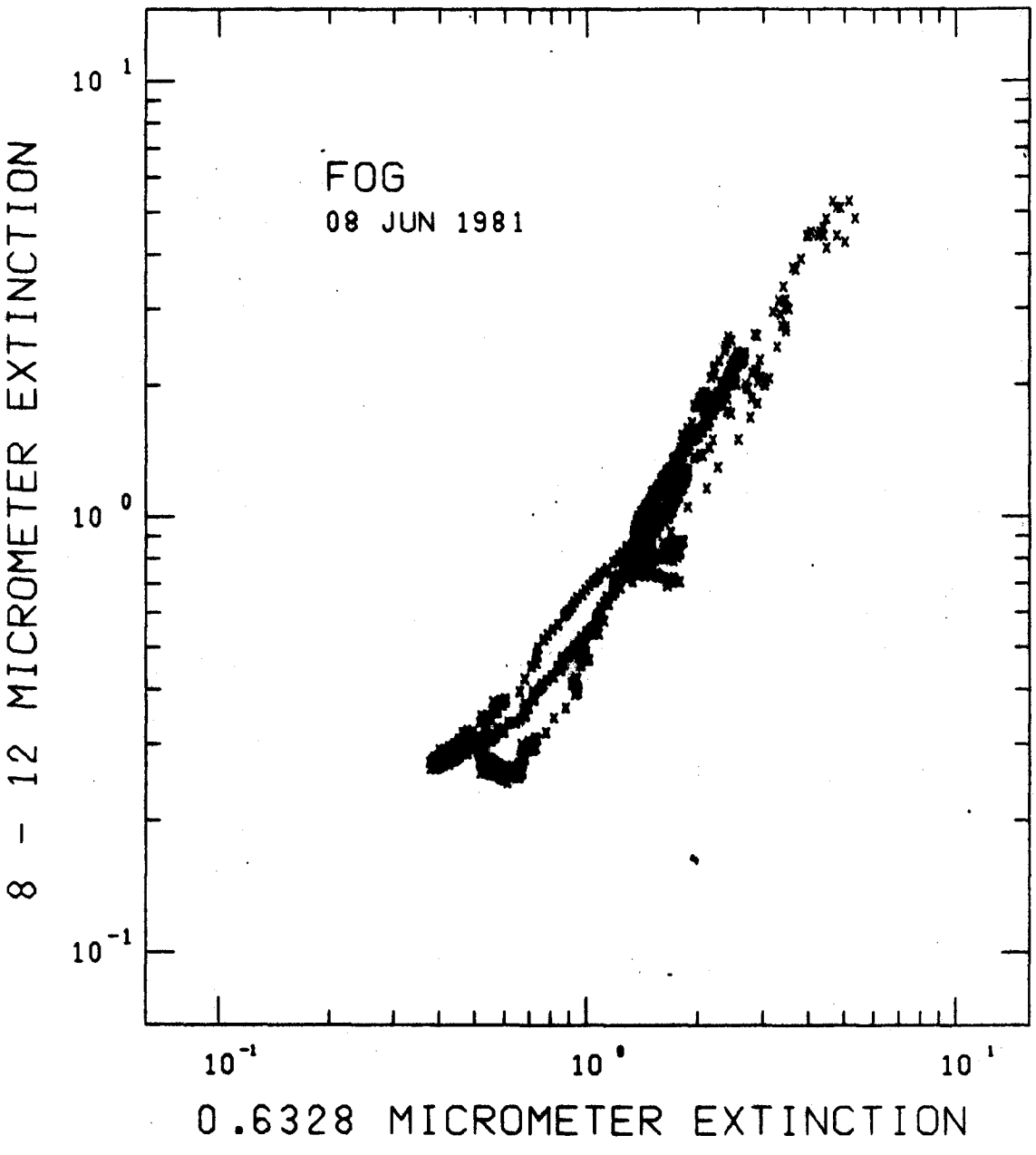

Figure 29. Extinction in Fog, 8 June 1981.

compounded by sampling at thirty-minute intervals as has been past practice. By sampling at one-minute intervals the continuous change in the GAP-type curve may be observed. This is best illustrated in Figure 27 and can also be seen in Figures 28 and 29. The spread in parameterized curves observed over many fogs is due to the variations in the fog droplet size distribution function.

When measuring the extinction coefficients at 0.6328 micrometers and in the 8 to 12 micrometer band by rain, it is important to include the susceptibility of each instrument to scattered radiation. Rain drops are large compared to the wavelengths of radiation considered here and the phase functions will be dominated by an intense forward scattering peak. If the complex index of refraction of the rain drops is assumed then almost all the visible radiation is scattered with only a very small amount being absorbed while the scattering and absorption contributions to extinction are approximately equal in the infrared band (Winchester, et al, 1981). Comparison of the measured extinction coefficients due to rain is shown in Figure 30. Both extinction coefficients graphed in Figure 30 include other losses such as absorption due to atmospheric gases and water vapor and are not corrected for scattered radiation. The data for 6 June 1981 are typical of extinction data by rain.

Because of an average annual snowfall of over six meters, extinction of visible and infrared radiation by falling and blowing snow may be studied extensively at KRC. Transmission measurements were made at 0.6328 and 1.06 micrometers and in the 8 to 12 micrometer band. As mentioned previously, the three transmissometer systems are susceptible to scattered radiation to different degrees. Therefore the GAP-type curves parameterized by the observed extinction values depend on the phase function of the scattering particles. A change in the type or size of the scattering particles will affect the slope and position of the parameterized curve.

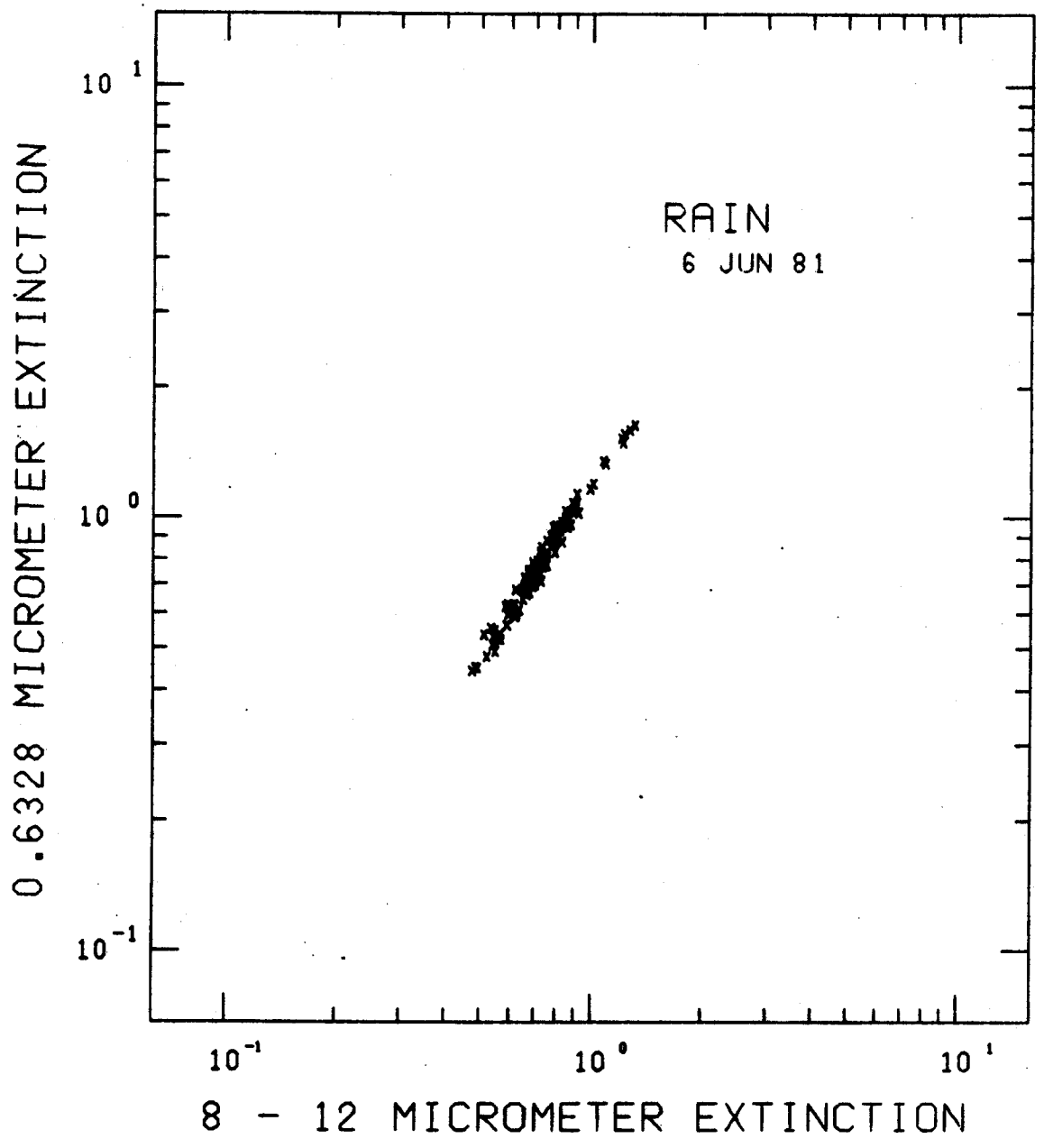

Figure 30. Extinction in Rain, 6 June 1981.

When data collected over a period of several days is plotted on a single graph, a large spread in the data is present as shown in Figure 31 for data taken between 26 and 28 January 1982. The spread in the data is due to the presence of several different crystal types during the three-day period. This is very similar to the curves of Turner, et al (1980) for fog. The same behavior is seen in a plot of the 1.06 micrometer extinction as a function of the 0.6328 micrometer extinction shown in Figure 32 and in a plot of the 8 to 12 micrometer extinction as a function of the 1.06 micrometer extinction shown in Figure 33. When dealing with one type of crystal the spread of the extinction coefficient in the 8 to 12 micrometer band for any given value of the extinction coefficient is reduced considerably as shown in Figure 34. The data were taken in blowing snow over a seven-day period. Blowing snow consists of very small broken snow crystals resembling needles or bullets with well-defined scattering properties. Similar results are shown in Figure 35 where the extinction coefficients at 1.06 micrometers and at 0.6328 micrometers are plotted. Figure 36 illustrates the behavior of the extinction coefficient in the 8 to 12 micrometer band as a function of the 1.06 micrometer extinction coefficient. Again the spread of the data is reduced.

On 10 February 1982, transmission of 0.6328 micrometer radiation and transmission in the 8 to 12 micrometer band was measured in snow consisting of plate-type crystals. The data snown in Figure 37 lie in a narrow region when plotted on a fully logarithmic axis. The spread in data for high extinction values correspond to a time period which included some blowing snow.

On 20 February 1982, extinction measurements were made using all three transmissometer systems during a snowfall which consisted of planar dendritic crystals. A linear

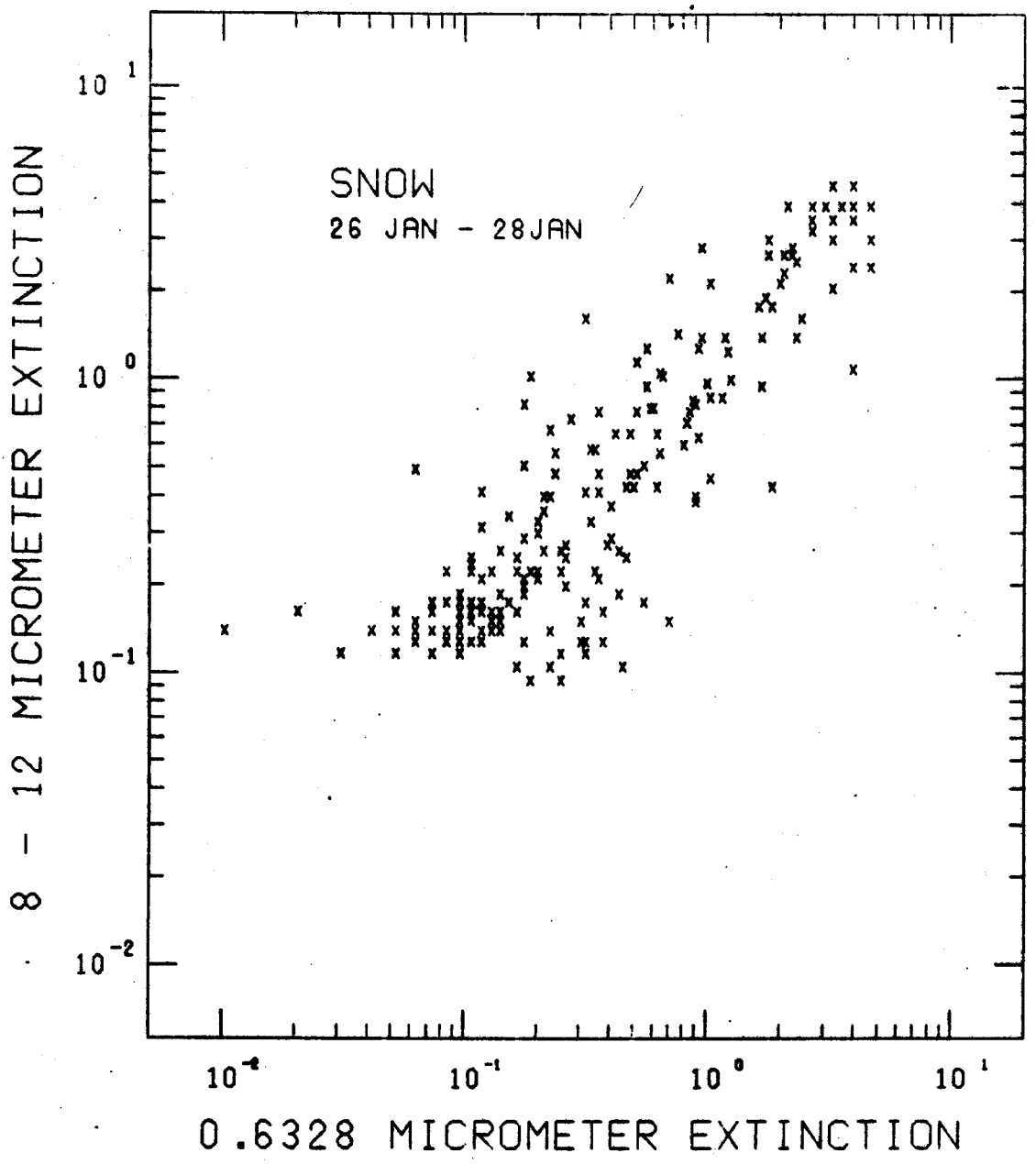

Figure 31. Extinction in Snow, 26-28 January 1982.

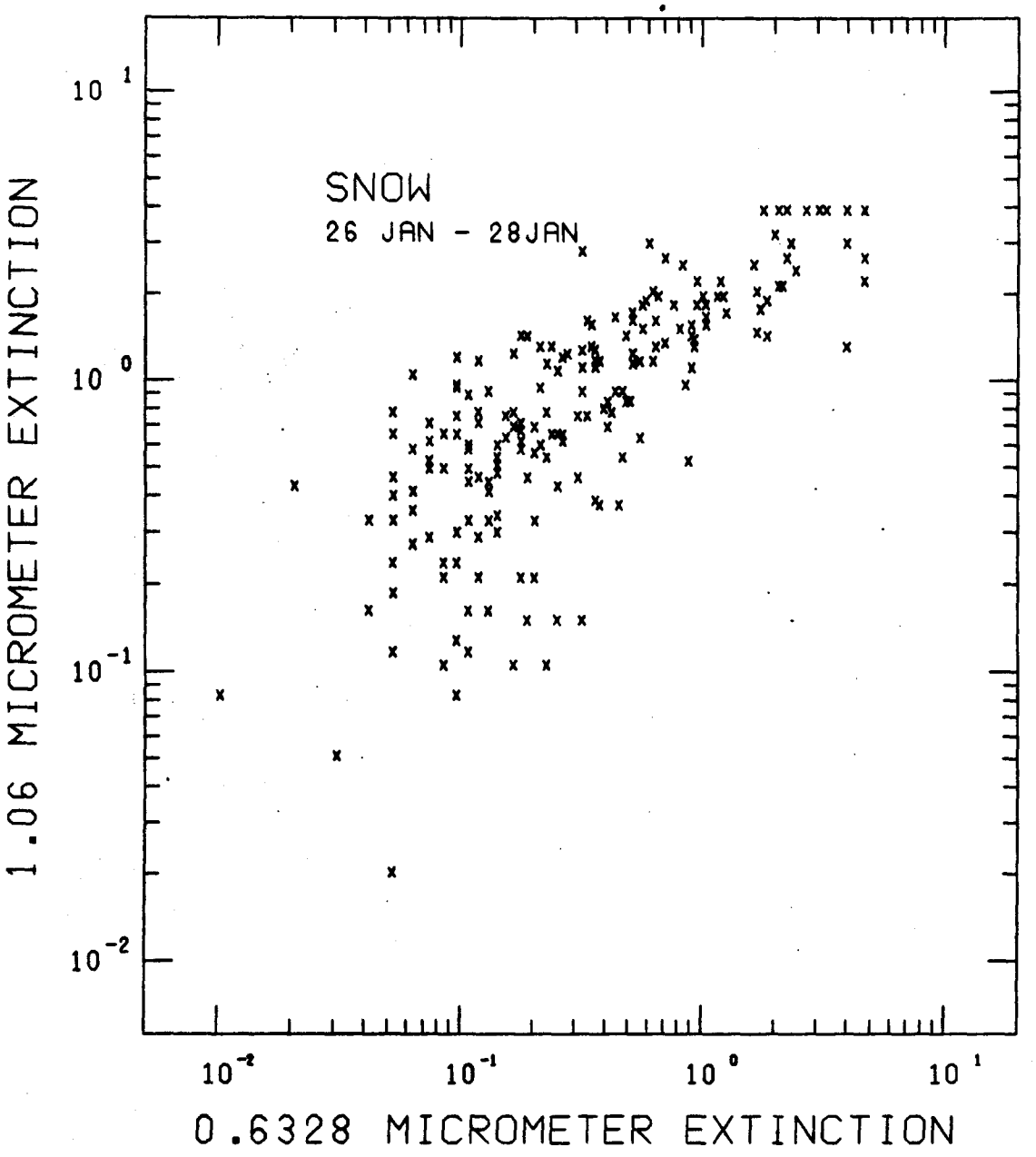

Figure 32. Extinction in Snow, 26-28 January 1982.

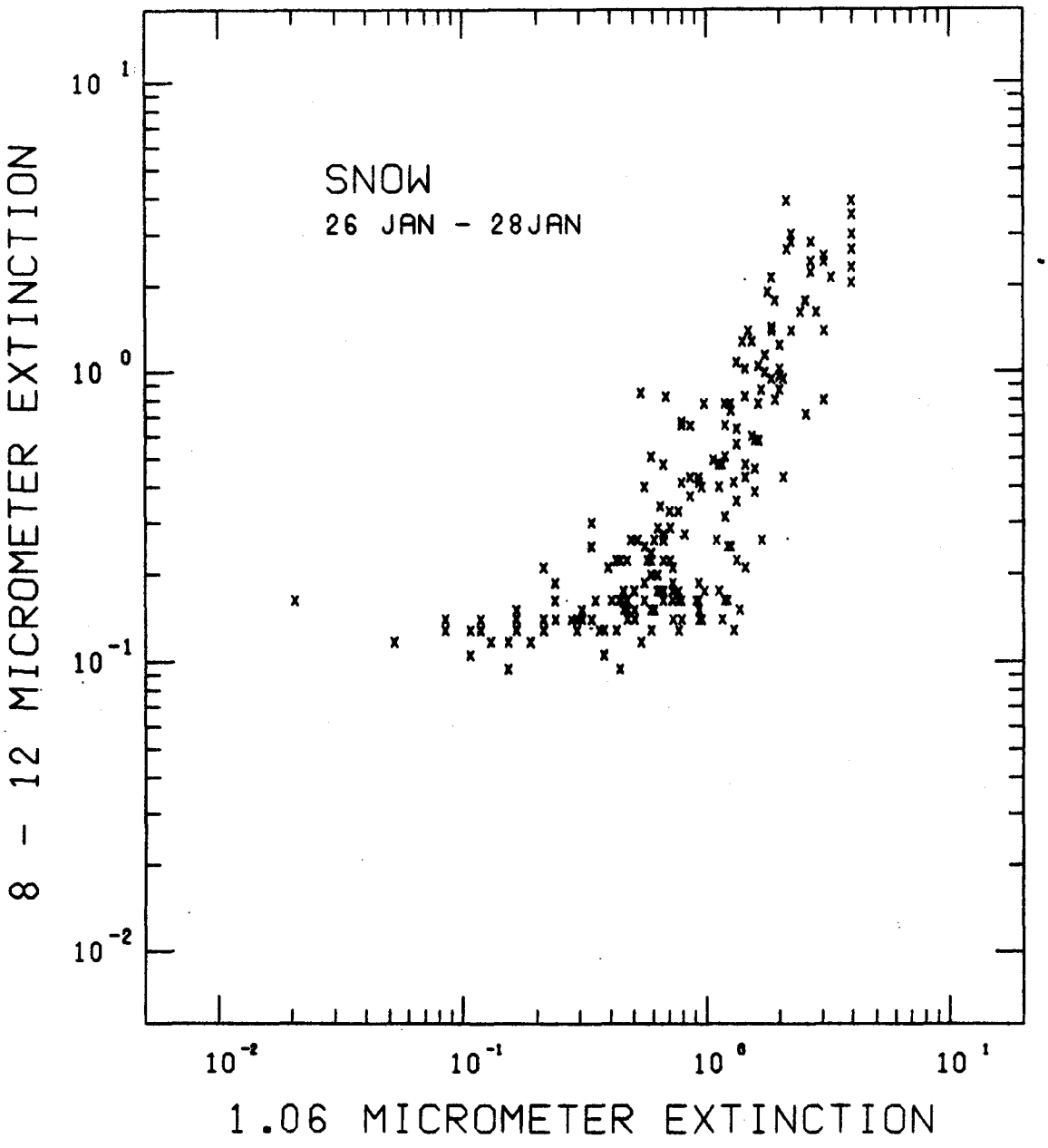

Figure 33. Extinction in Snow, 26-28 January 1982.

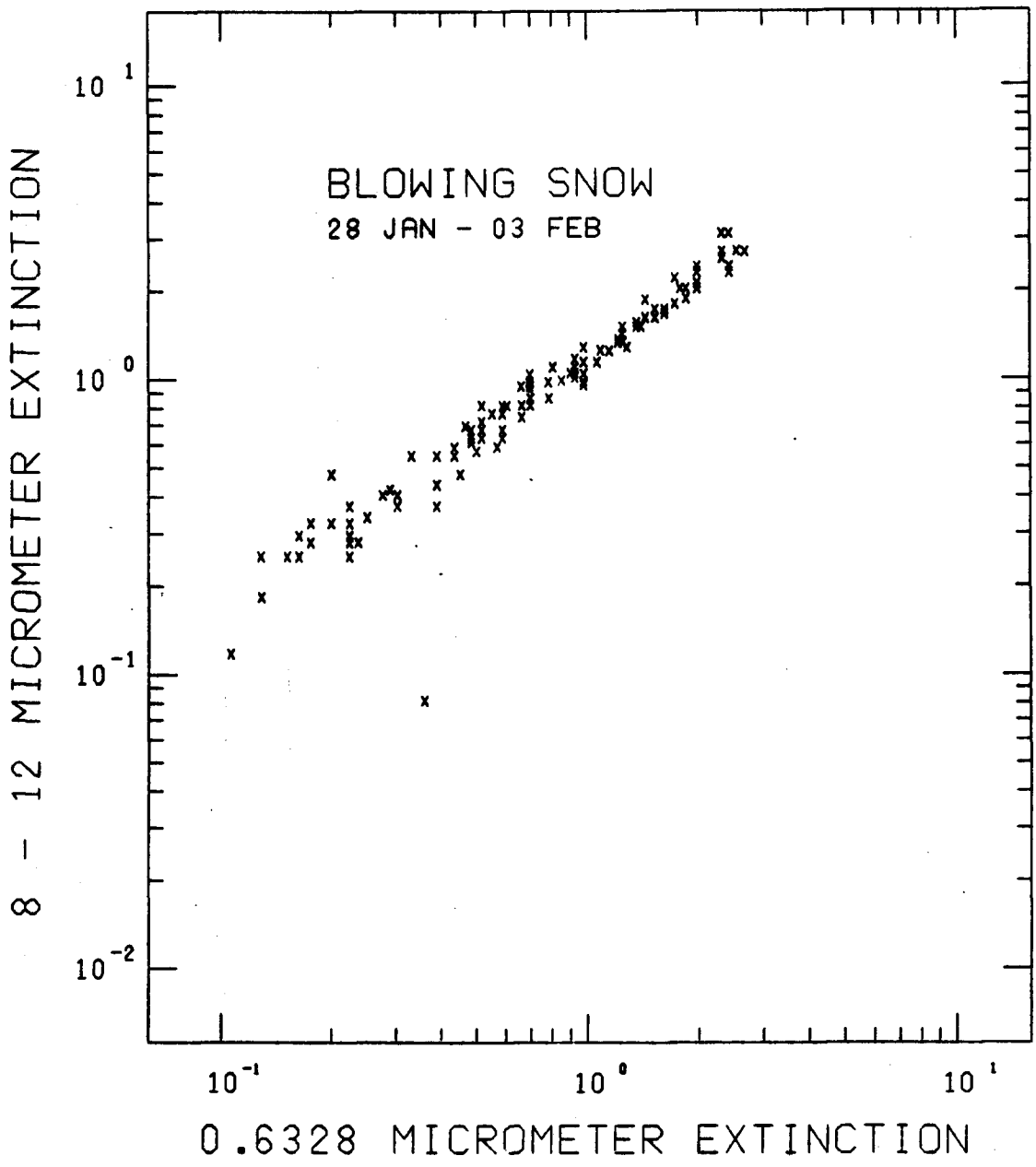

Figure 34. Extinction in blowing snow, 28 January - 03 February 1982.

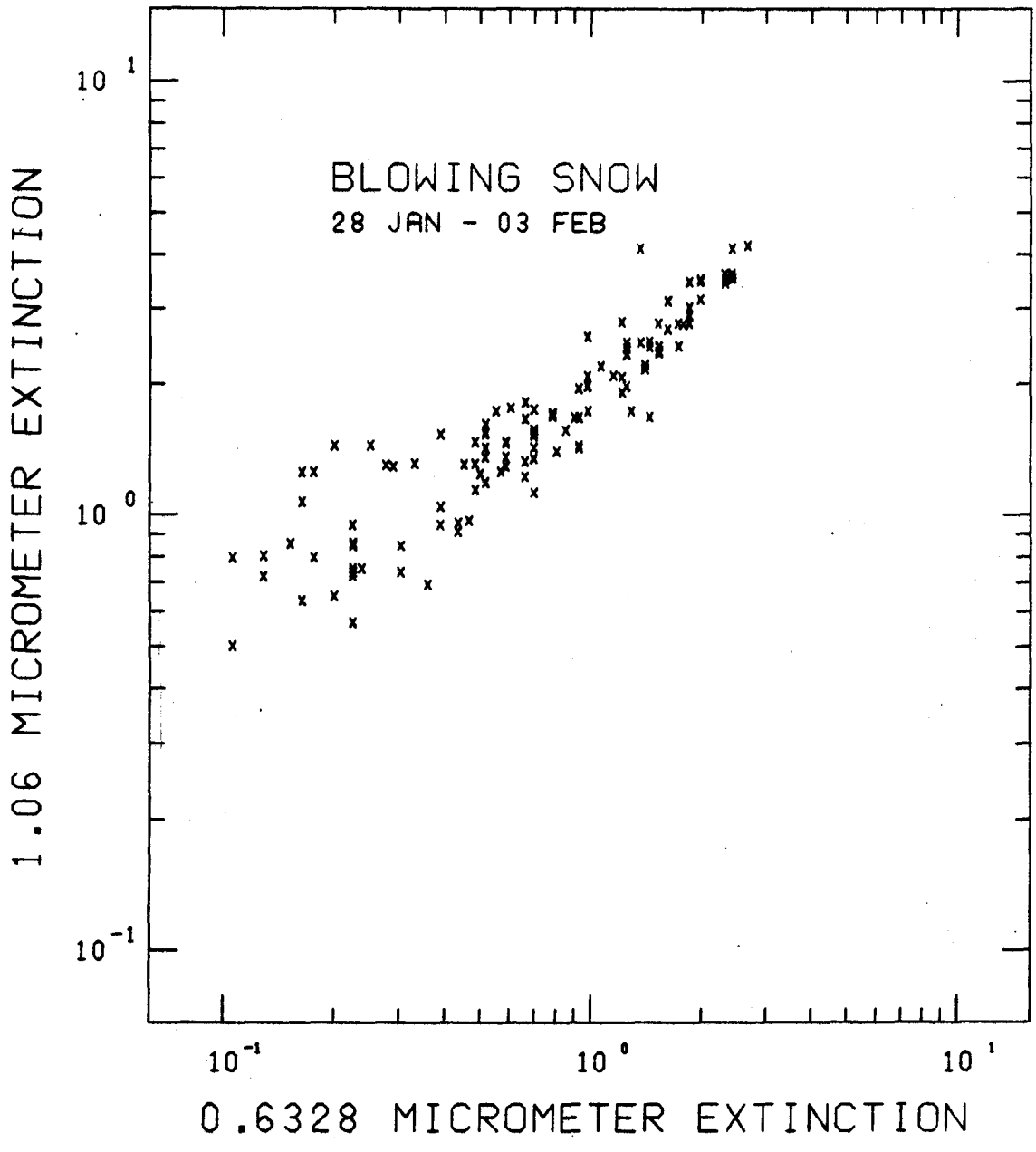

Figure 35. Extinction in blowing snow, 28 January - 03 February 1982.

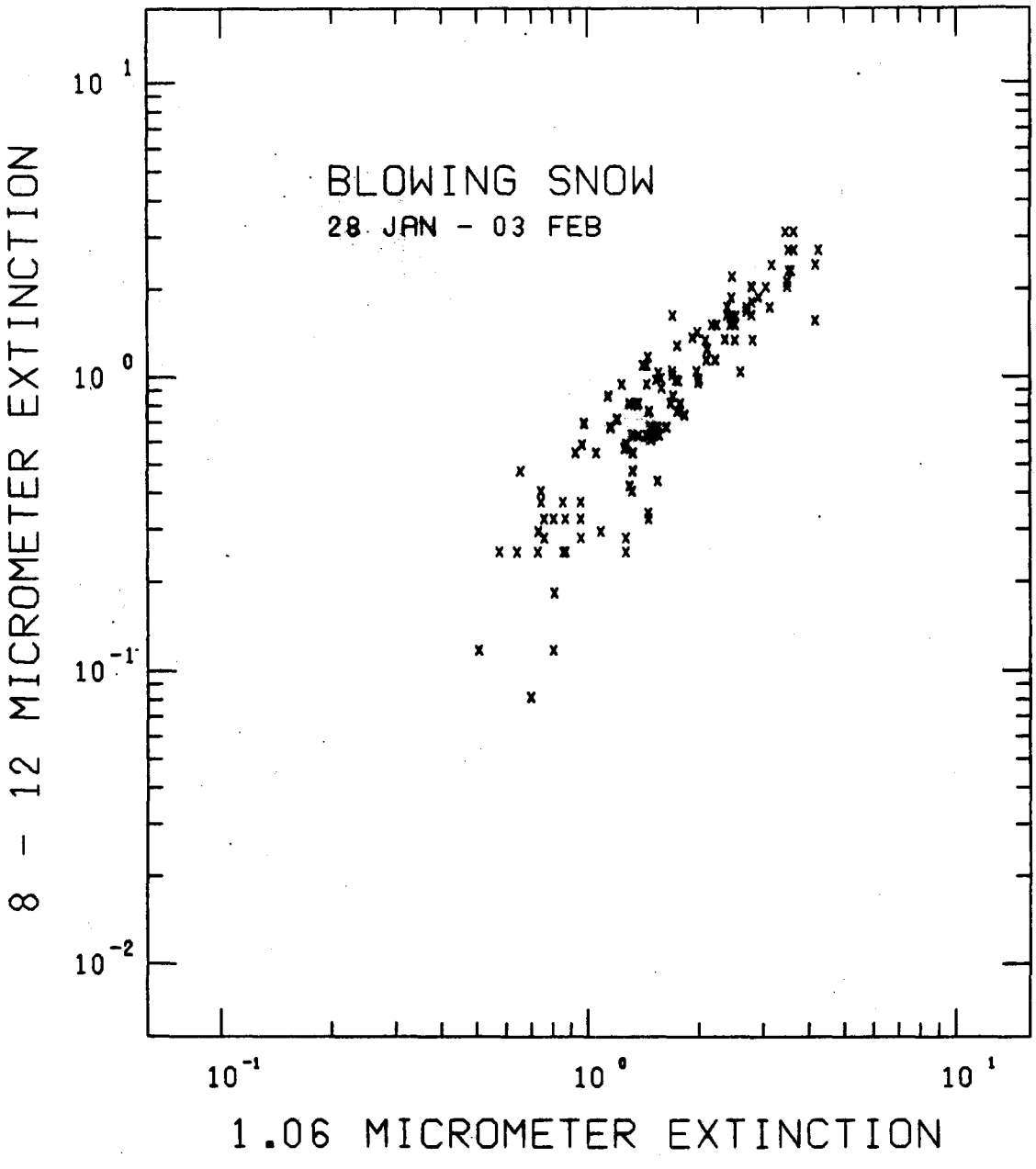

Figure 36. Extinction in blowing snow, 28 January - 03 February 1982.

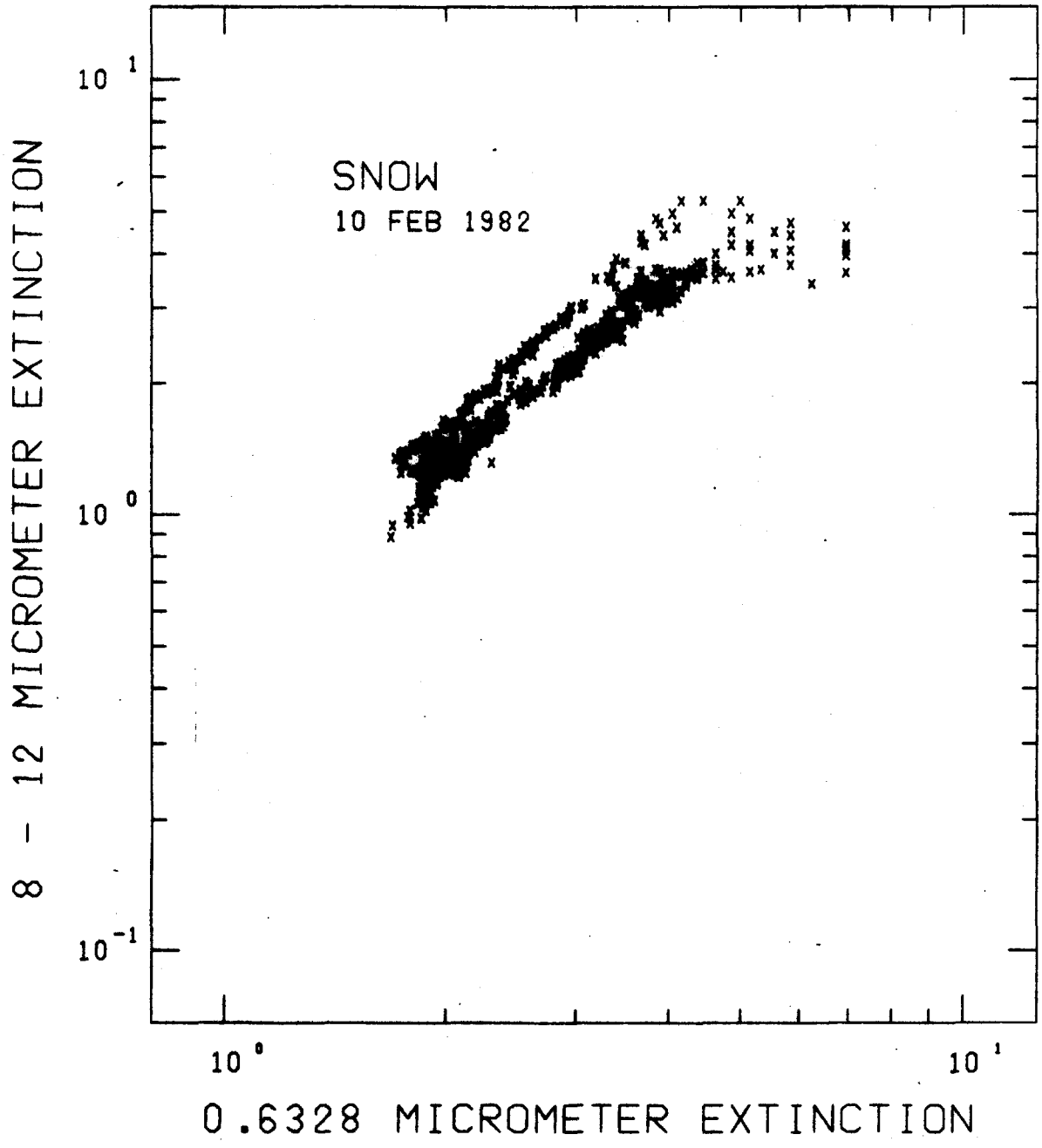

Figure 37. Extinction in snow, 10 February 1982.

relation between the 8 to 12 micrometer extinction coefficient and the 0.6328 micrometer extinction data is quite evident in Figure 38. The spread in 1.06 micrometer extinction shown in Figure 39 as a function of the value of the extinction coefficient at 0.6328 micrometers is much larger than that shown by the 8 to 12 micrometer extinction data. The spread in the data decreases as the magnitude of the extinction coefficients increase. A similar curve is shown in Figure 40 where the 8 to 12 micrometer data is plotted as a function of the 1.06 micrometer extinction coefficient. The spread in the data shown in Figures 39 and 40 is attributed to the measurements at 1.06 micrometers. This phenomena was observed repeatedly. On 21 February 1982, Figures 41, 42 and 43 are GAP-type plots of the extinction data measured in falling snow which consisted of large planar dendritic snow crystals. A large spread in the data associated with the 1.06 micrometer extinction coefficient is seen. On the next day, 22 February 1982, a variation in the 1.06 micrometer extinction coefficient was seen for needle-type snow crystals as shown in Figures 44, 45 and 46. In Figures 47, 48 and 49, extinction measurements made in a storm consisting of large needle-like crystals approximately 3 millimeters in length show a large spread in the data which is again attributed to the measurements at 1.06 micrometers.

The large spread in the 1.06 micrometer band is rarely seen at 0.6328 micrometers or in the 8 to 12 micrometer band extinction data. This phenomena will be discussed below. The linearity in the plots of the 8 to 12 micrometer band extinction data, as a function of the 0.6328 micrometer extinction, are to be found for all types of snow crystals when the types are considered singly. This is illustrated by Figure 50 for snow consisting of needles, Figure 51 for platelets, Figure 52 for needles, Figures 53 and 54 for planar dendritic, Figure 55 for needles and Figure 56 for

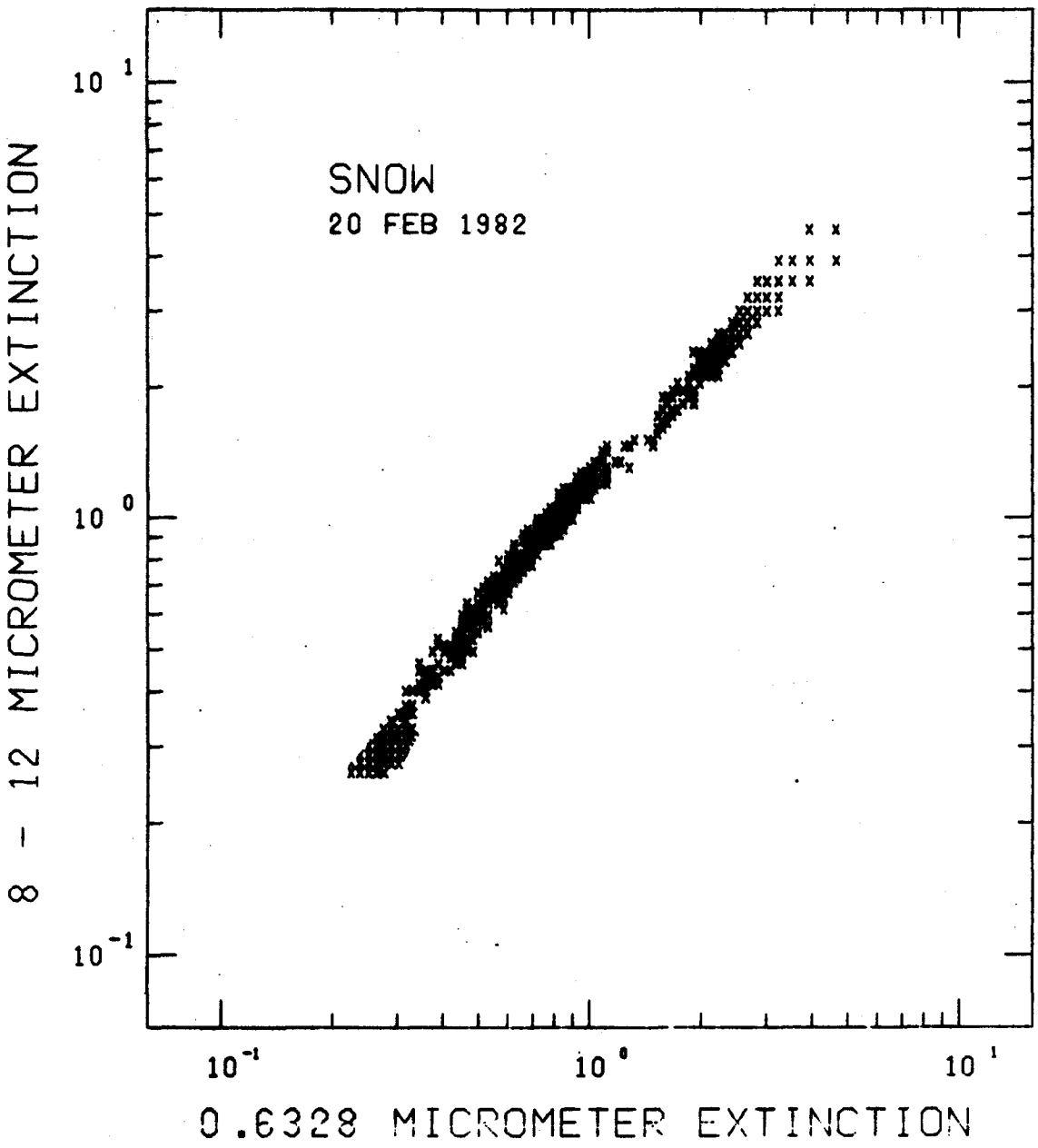

Figure 38. Extinction in snow, 20 February 1982.

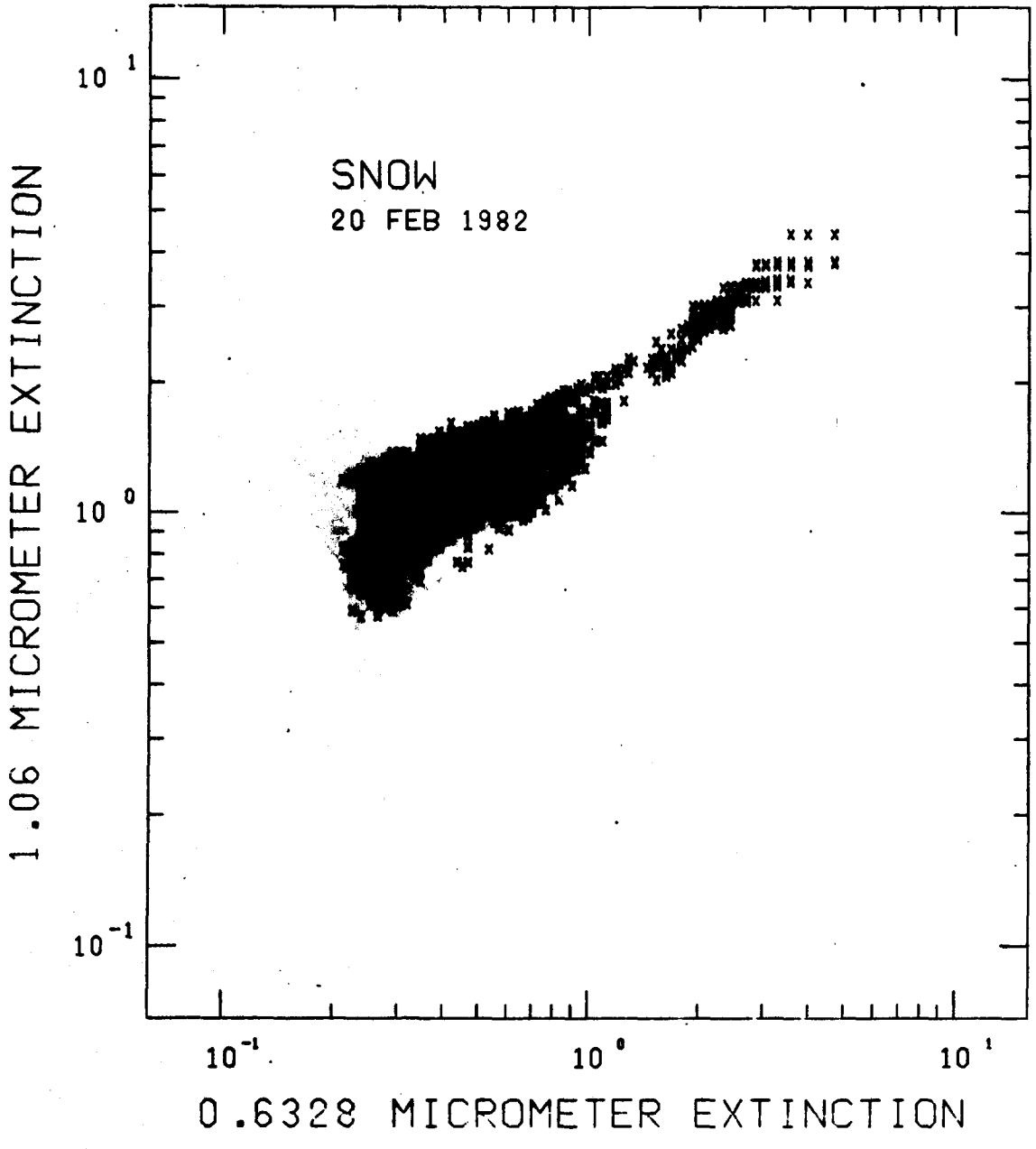

Figure 39. Extinction in snow, 20 February 1982.

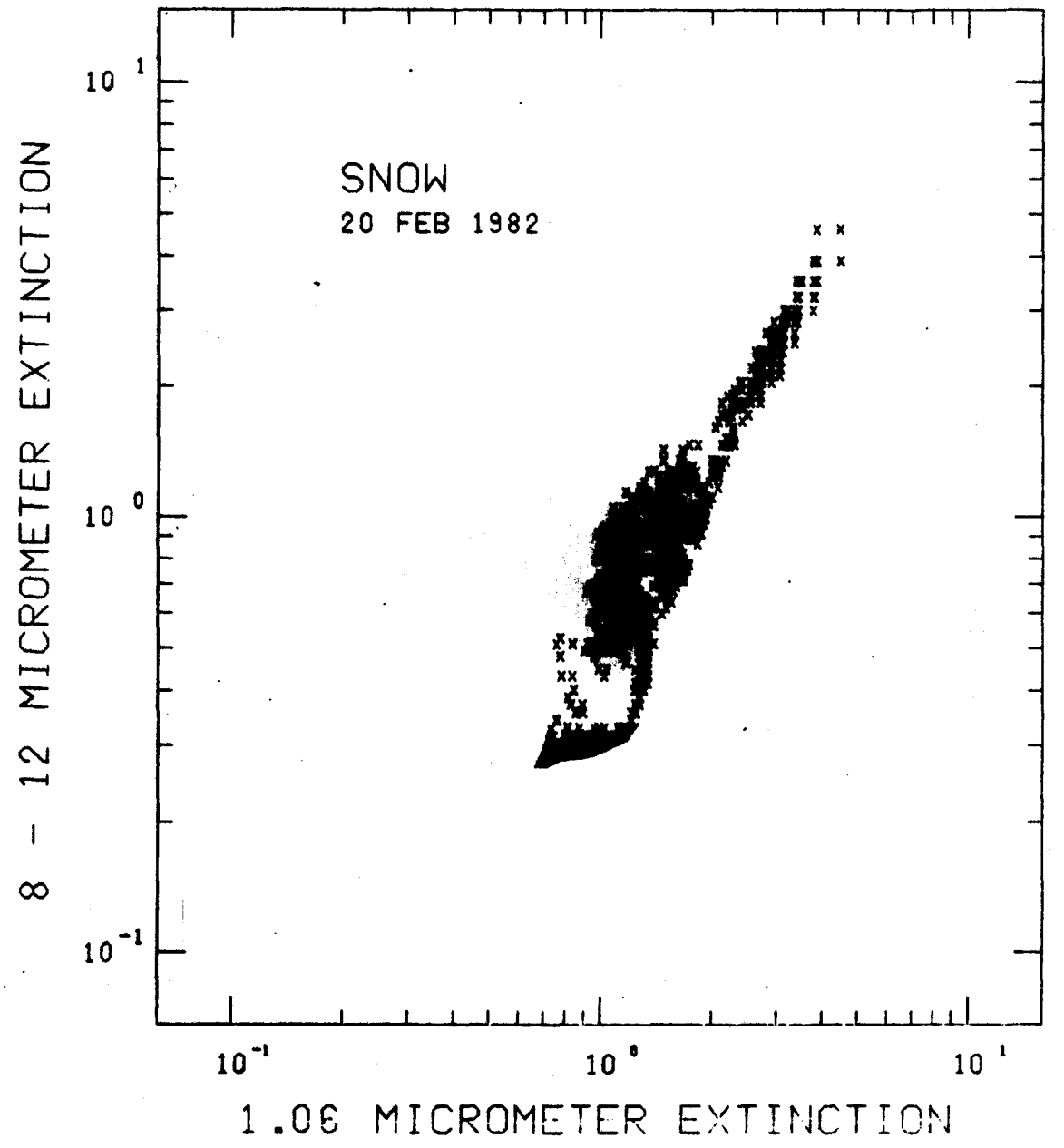

Figure 40. Extinction in snow, 20 February 1982.

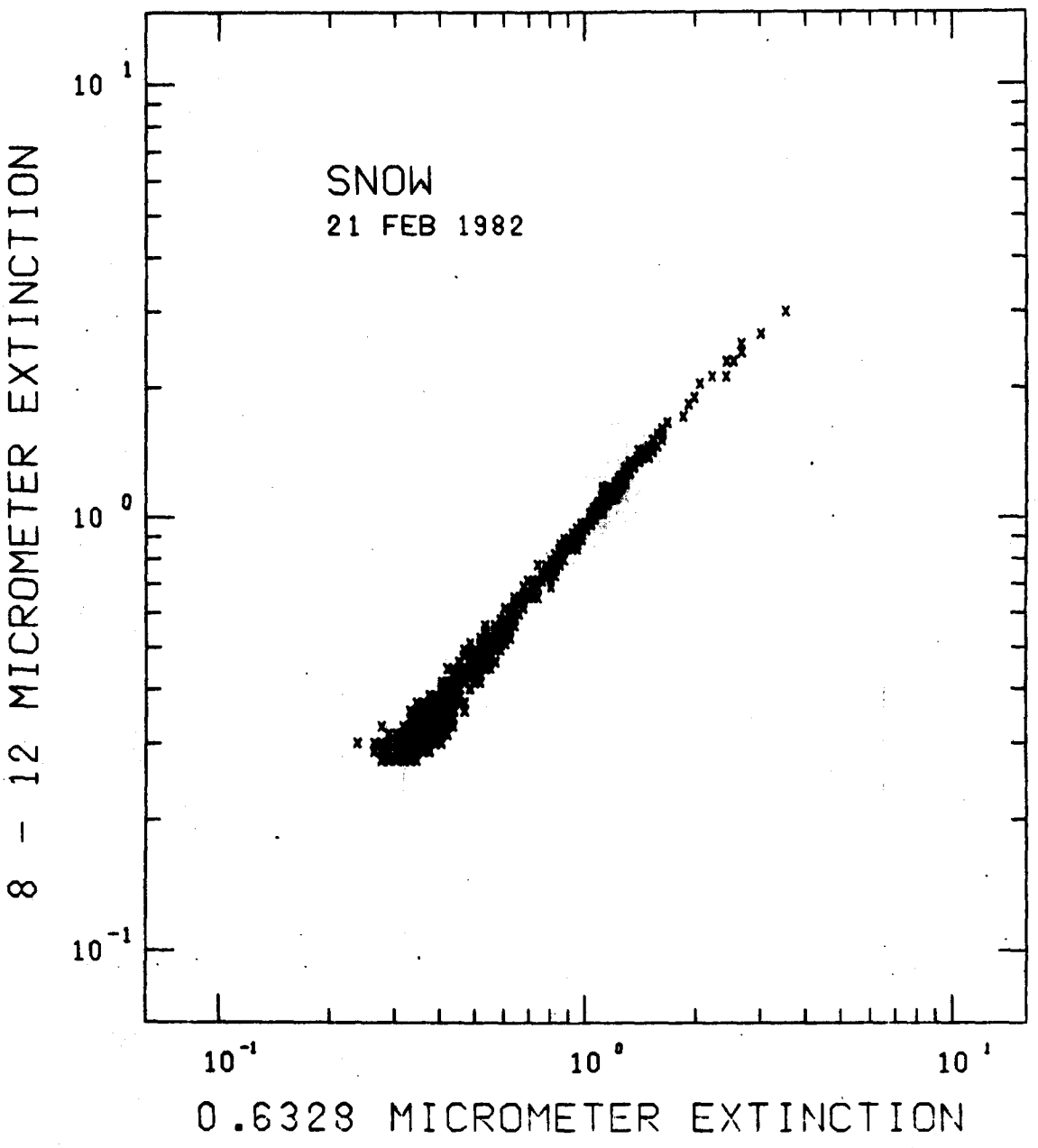

Figure 41. Extinction in snow, 21 February 1982.

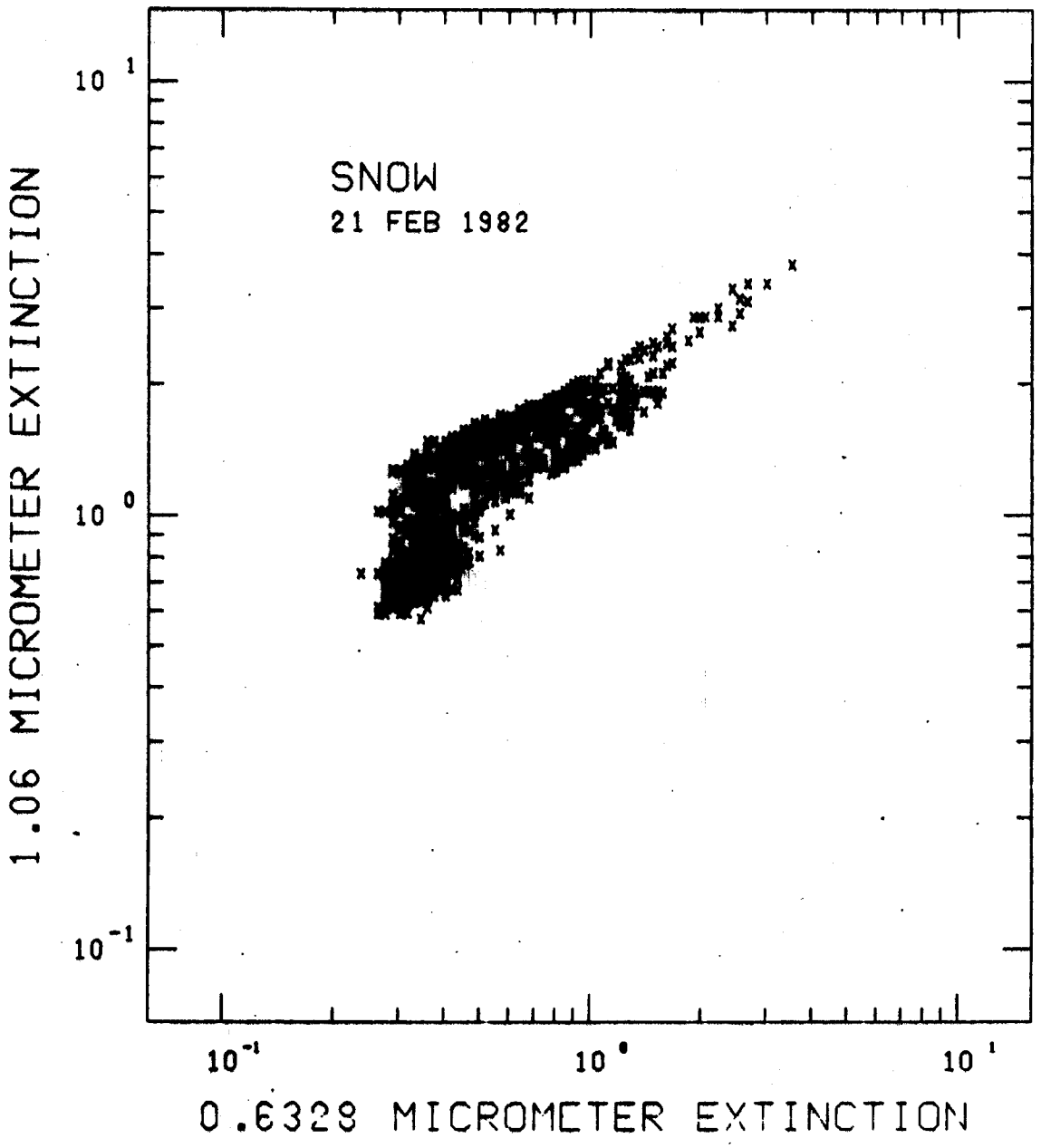

Figure 42. Extinction in snow, 21 February 1982.

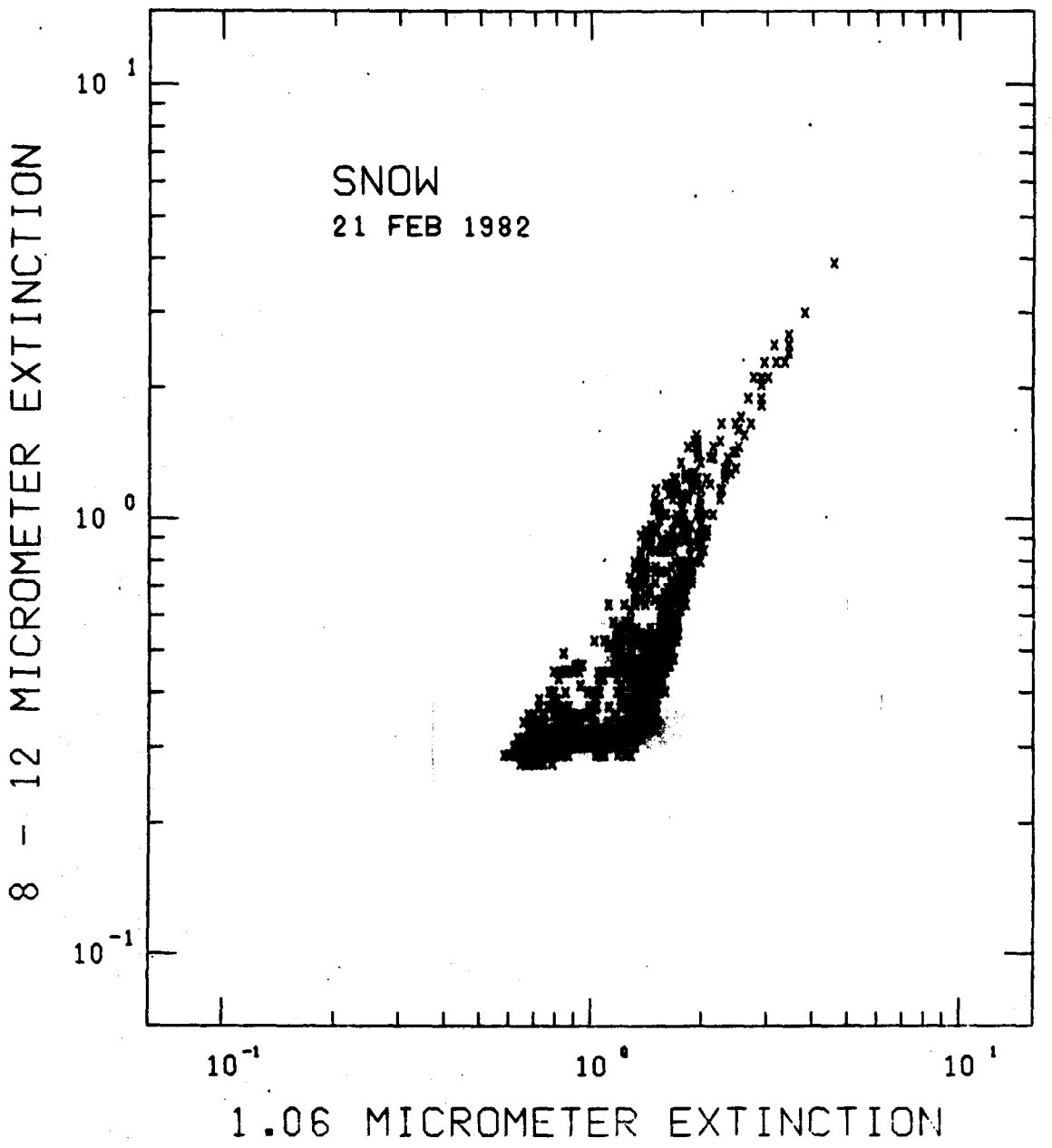

Figure 43. Extinction in snow, 21 February 1982.

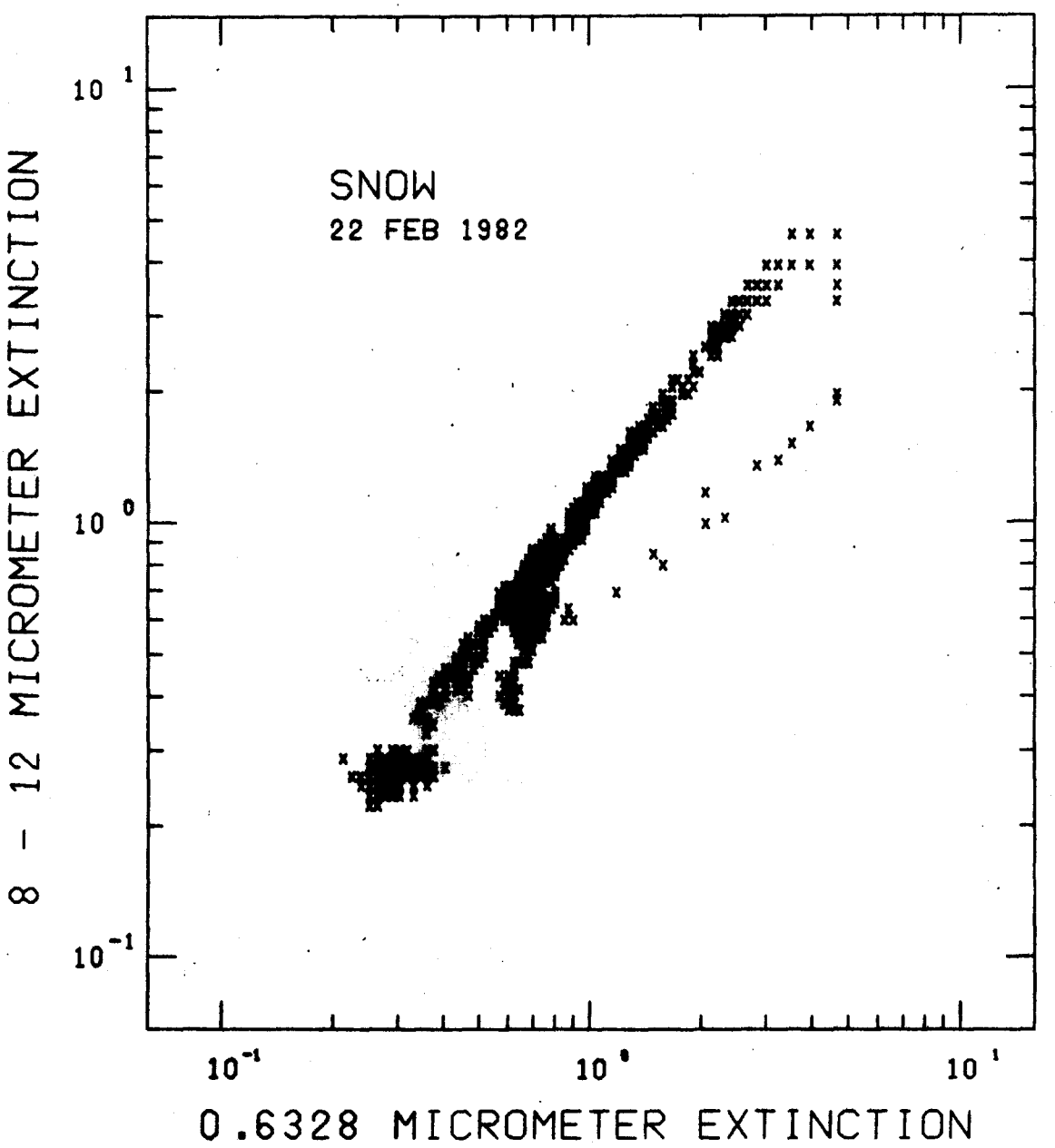

Figure 44. Extinction in snow, 22 February 1982.

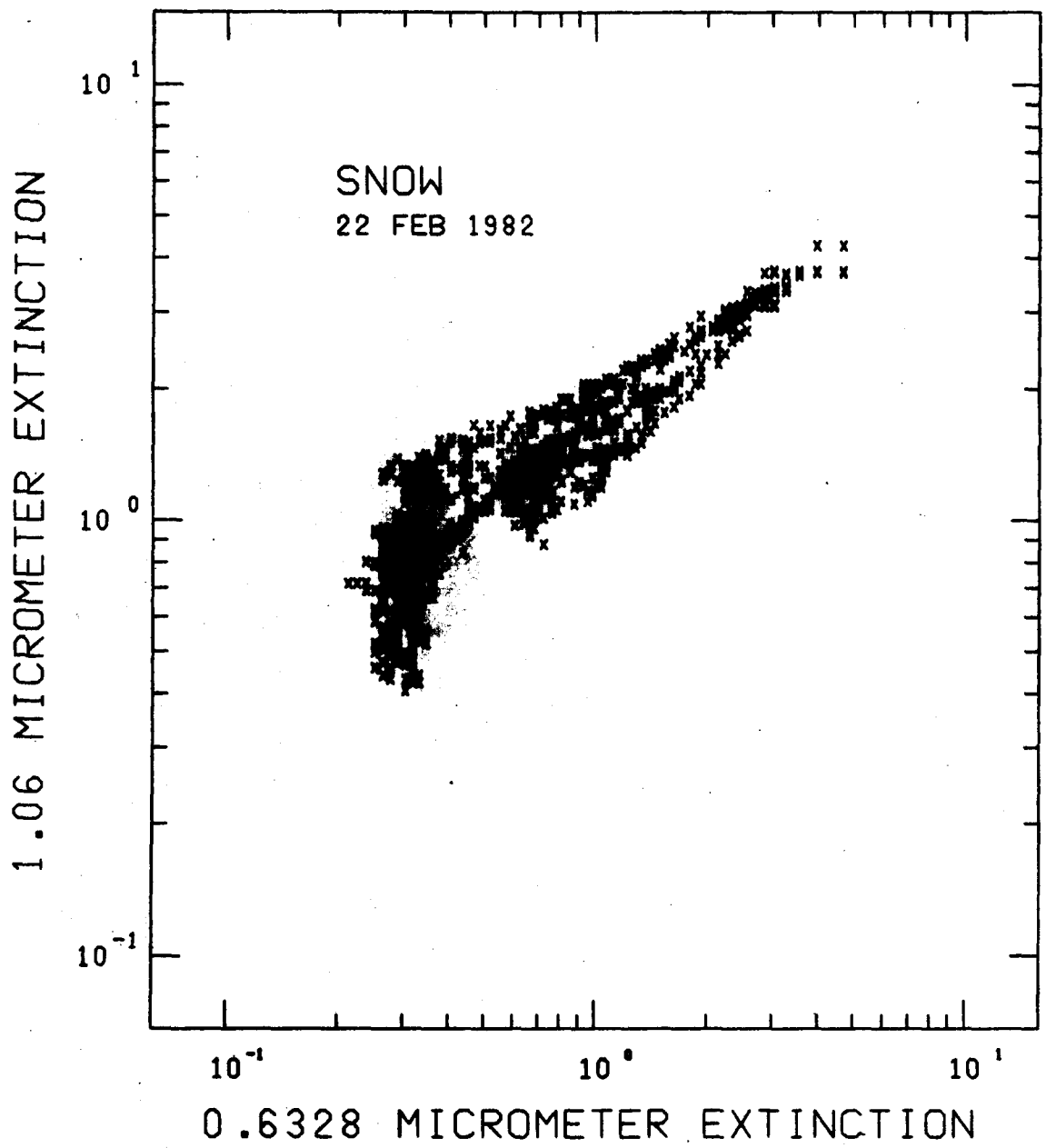

Figure 45. Extinction in snow, 22 February 1982.

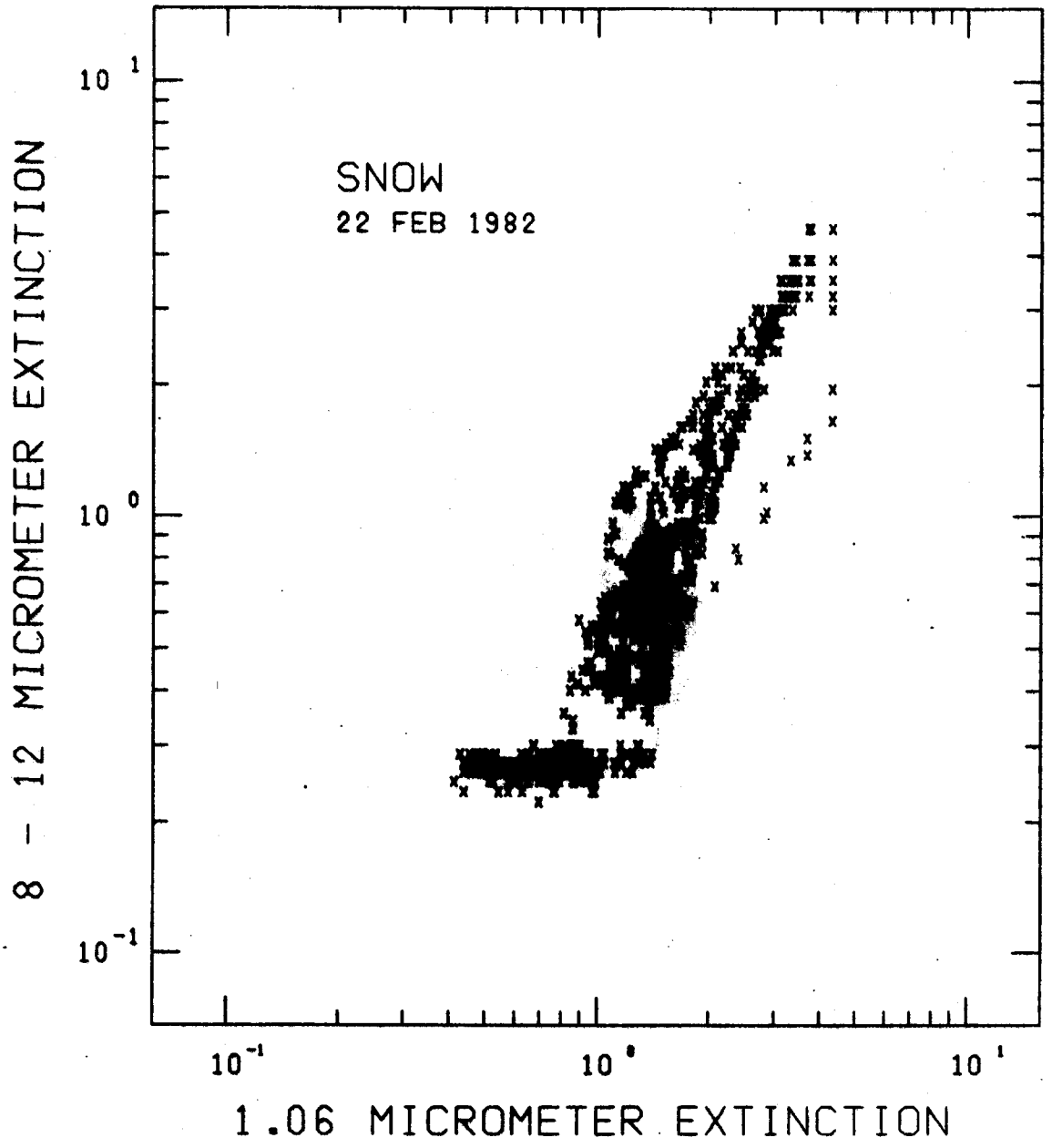

Figure 46. Extinction in snow, 22 February 1982.

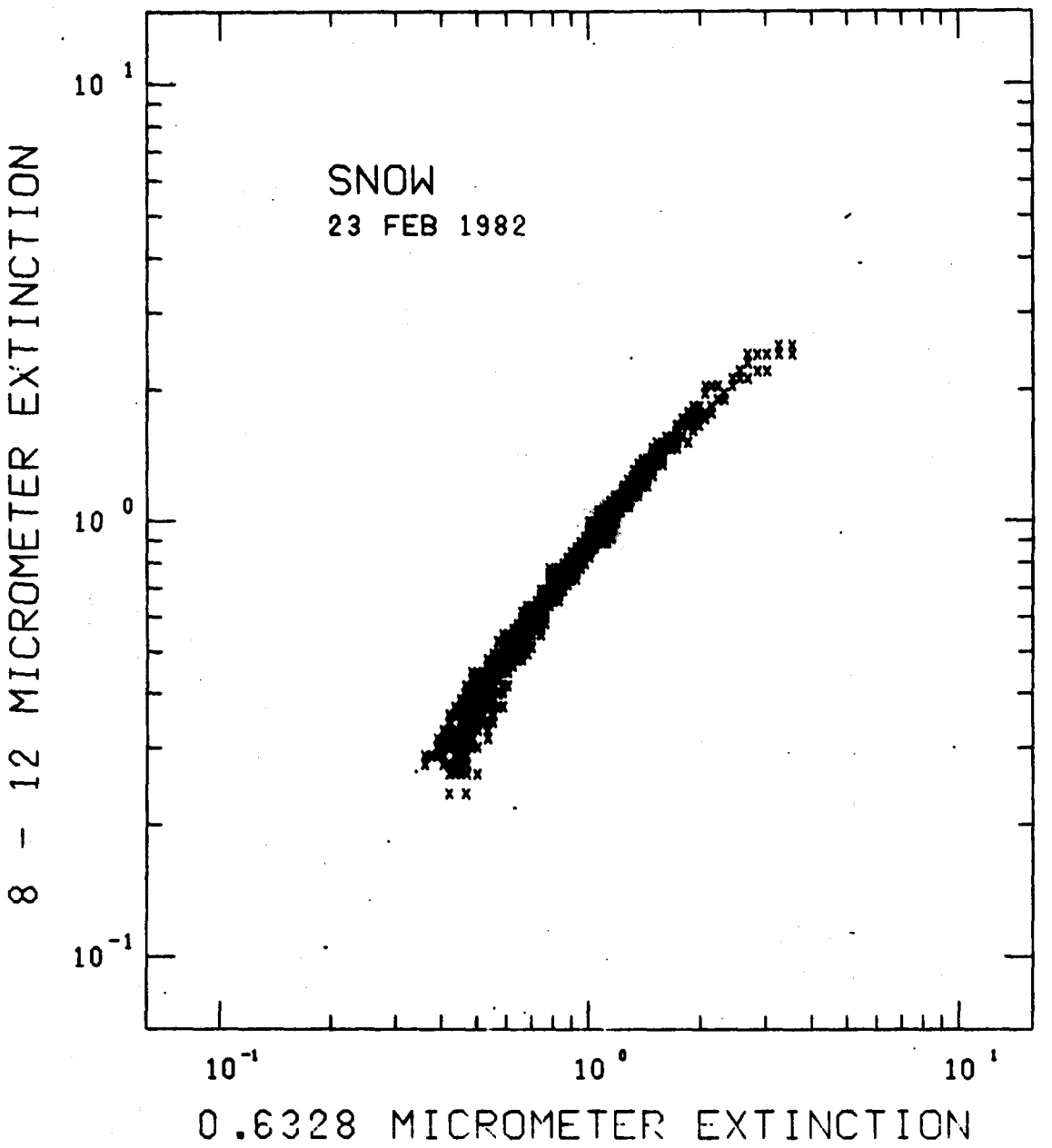

Figure 47. Extinction in snow, 23 February 1982.

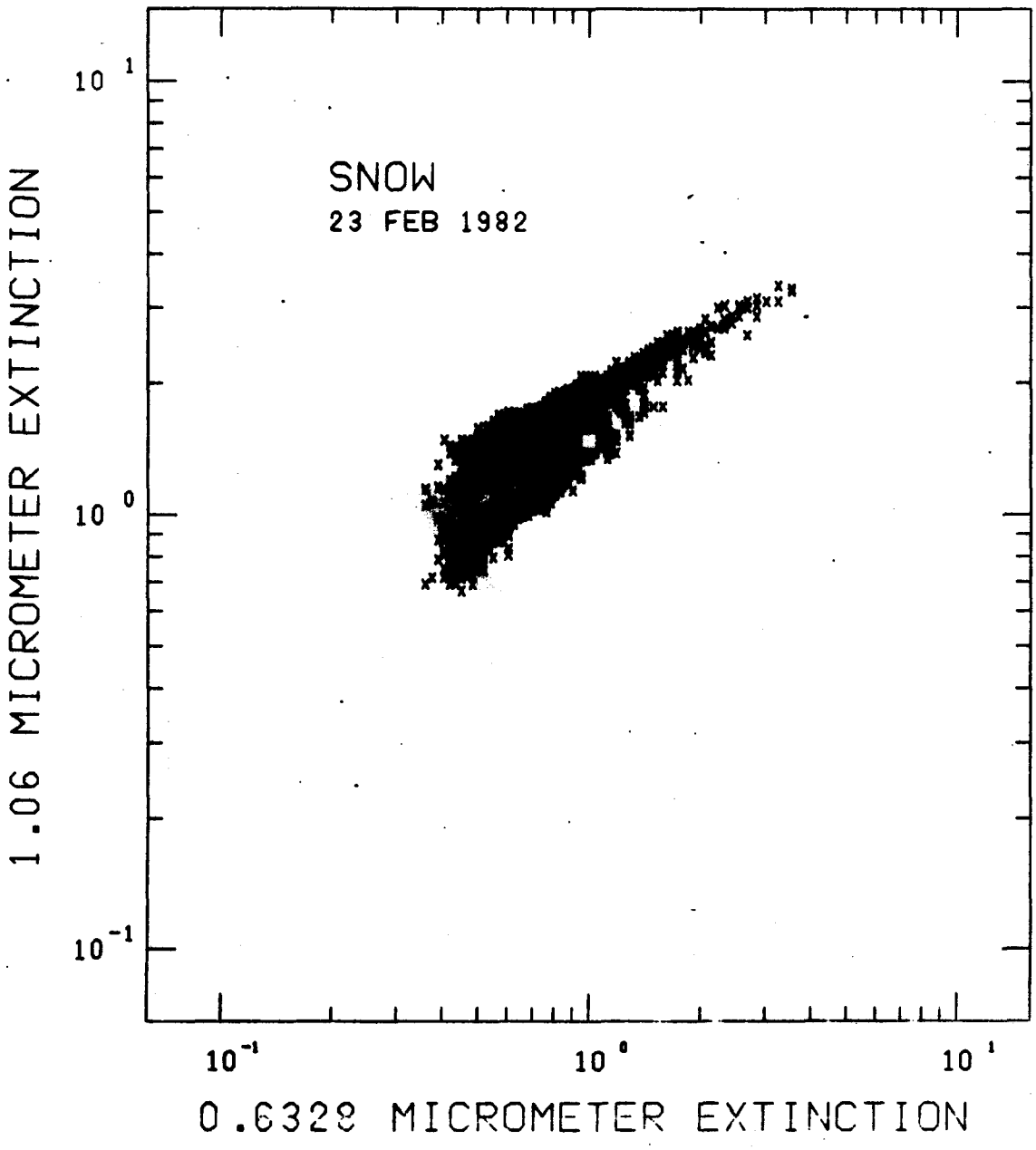

Figure 48. Extinction in snow, 23 February 1982.

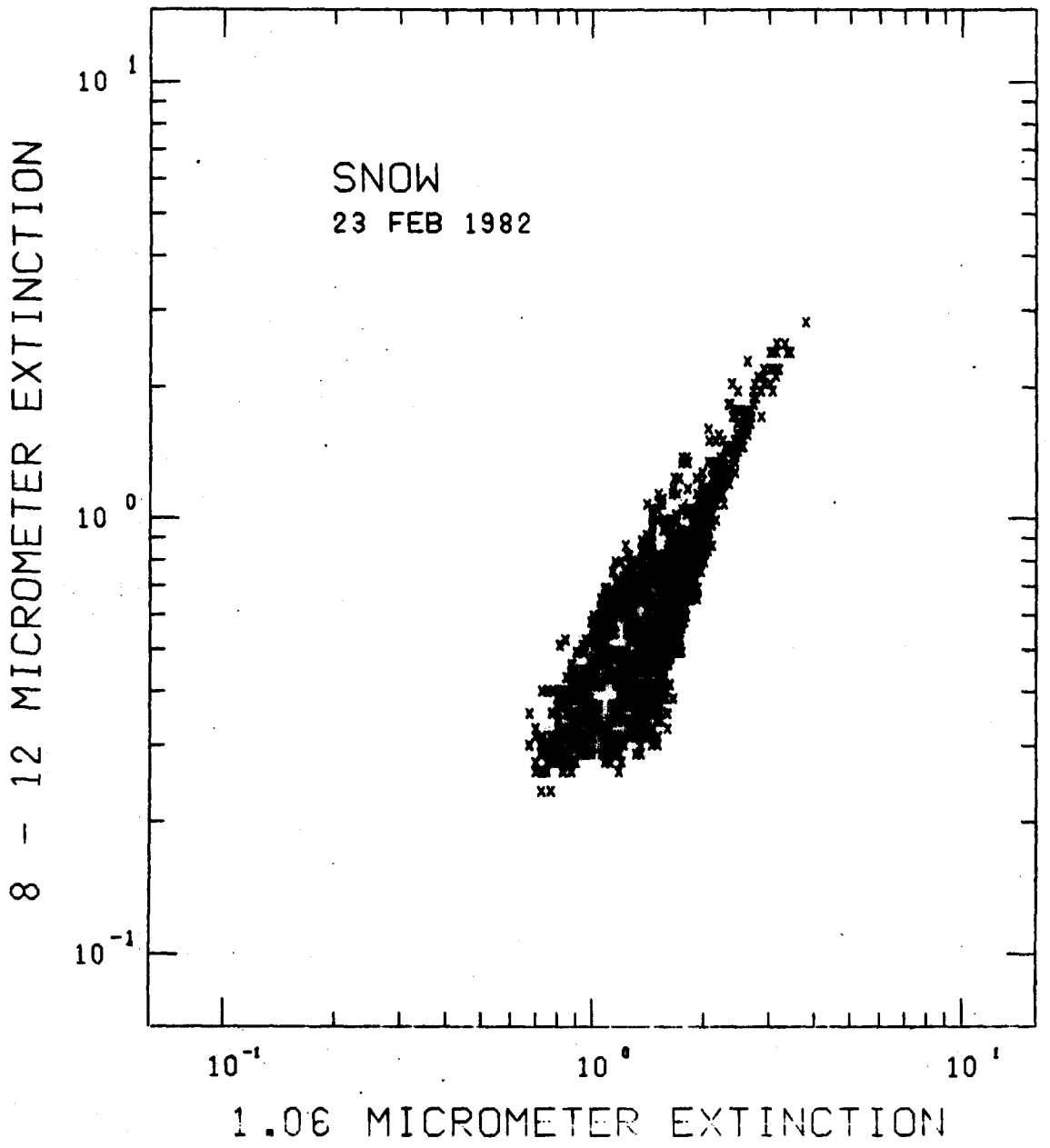

Figure 49. Extinction in snow, 23 February 1982.

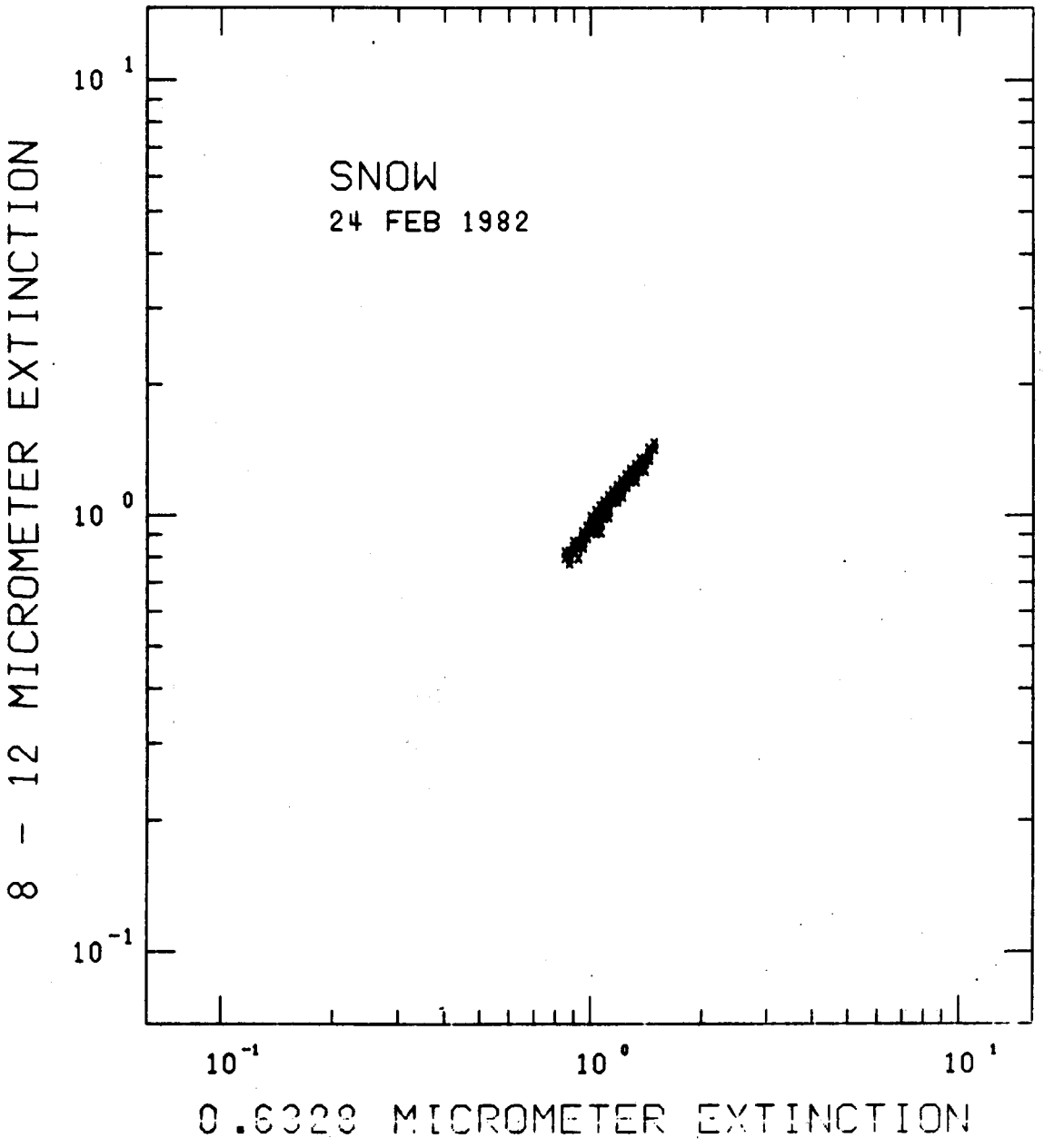

Figure 50. Extinction in snow, 24 February 1982.

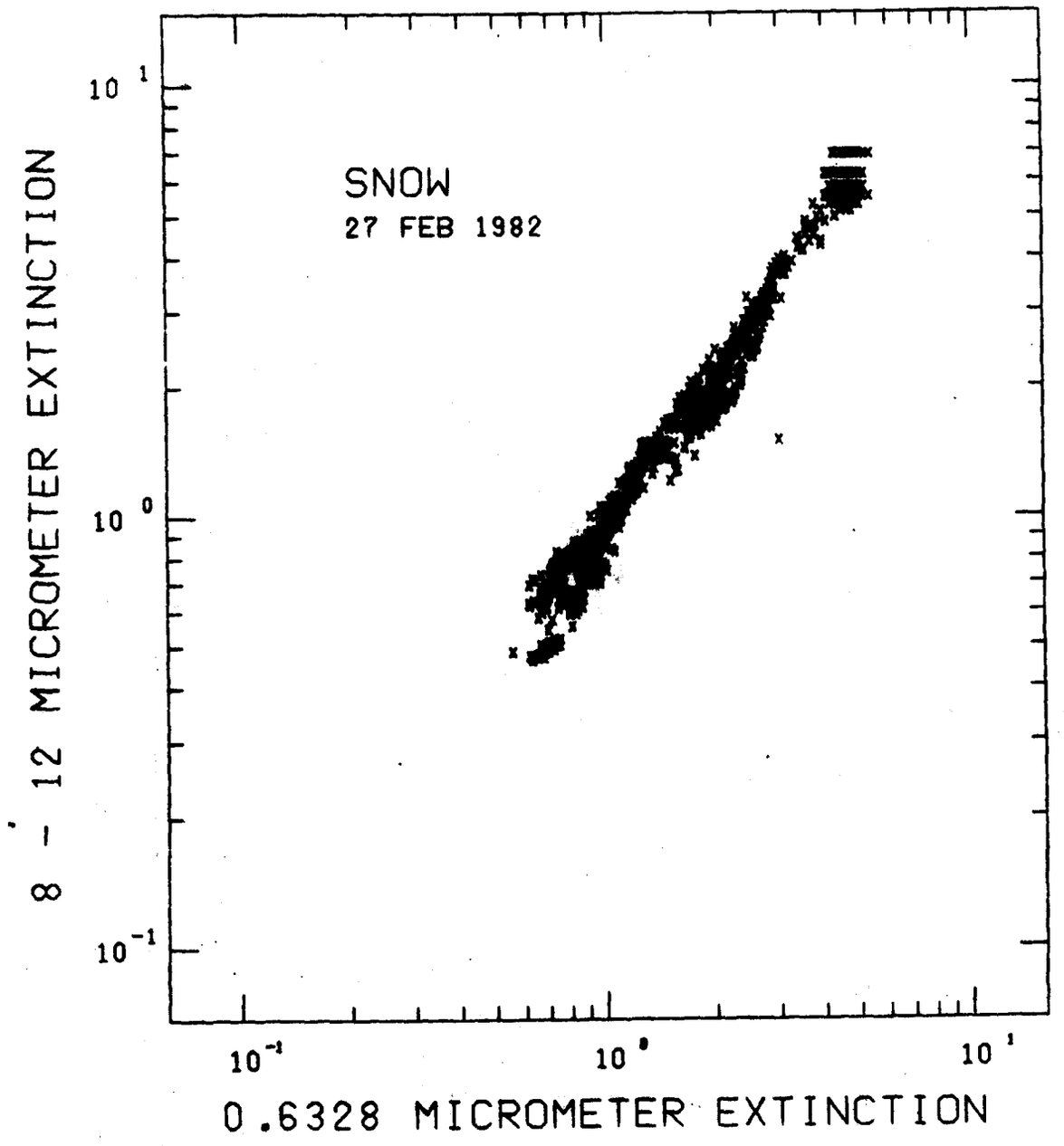

Figure 51. Extinction in snow, 27 February 1982.

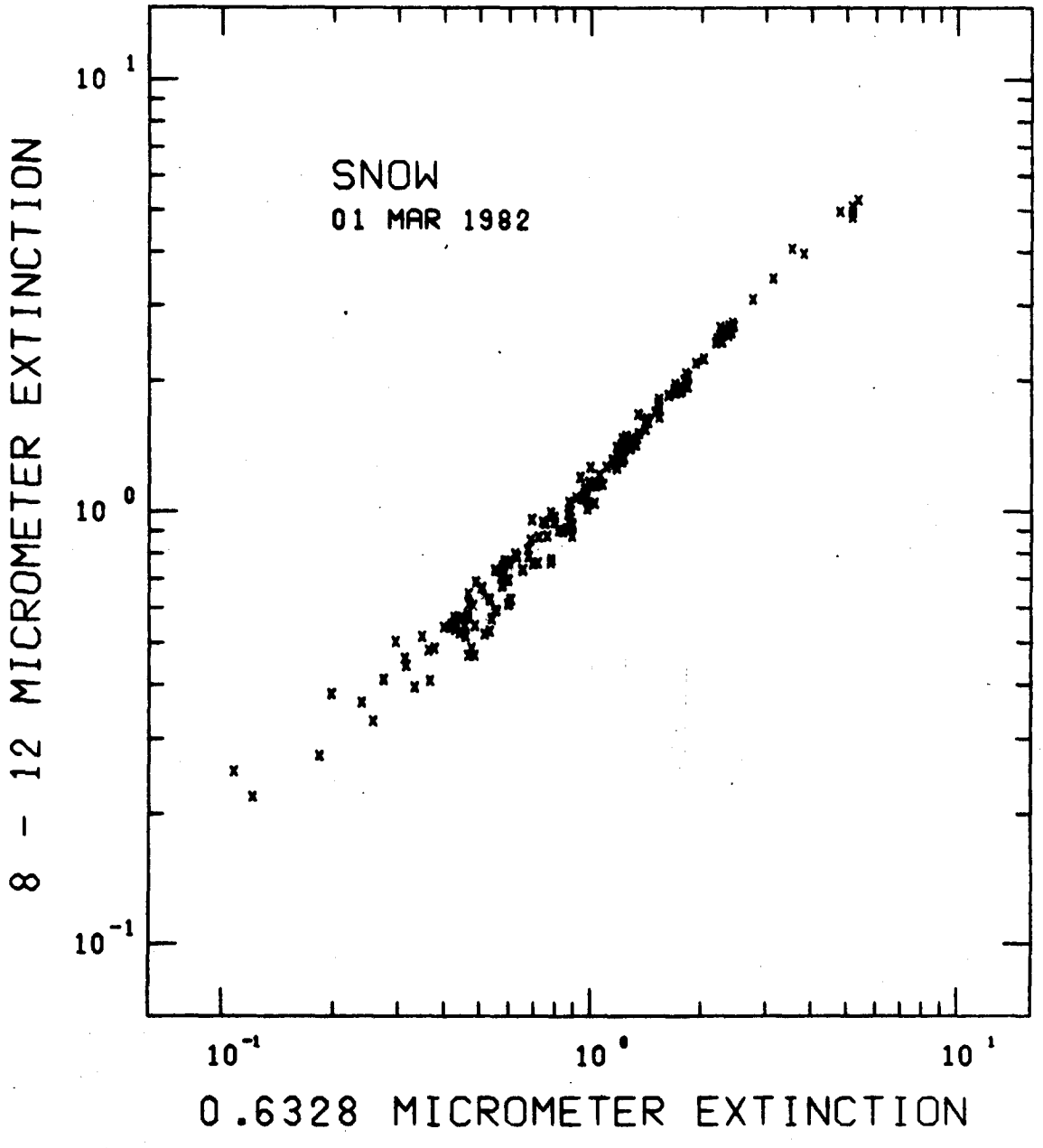

Figure 52. Extinction in snow, 01 March 1982.

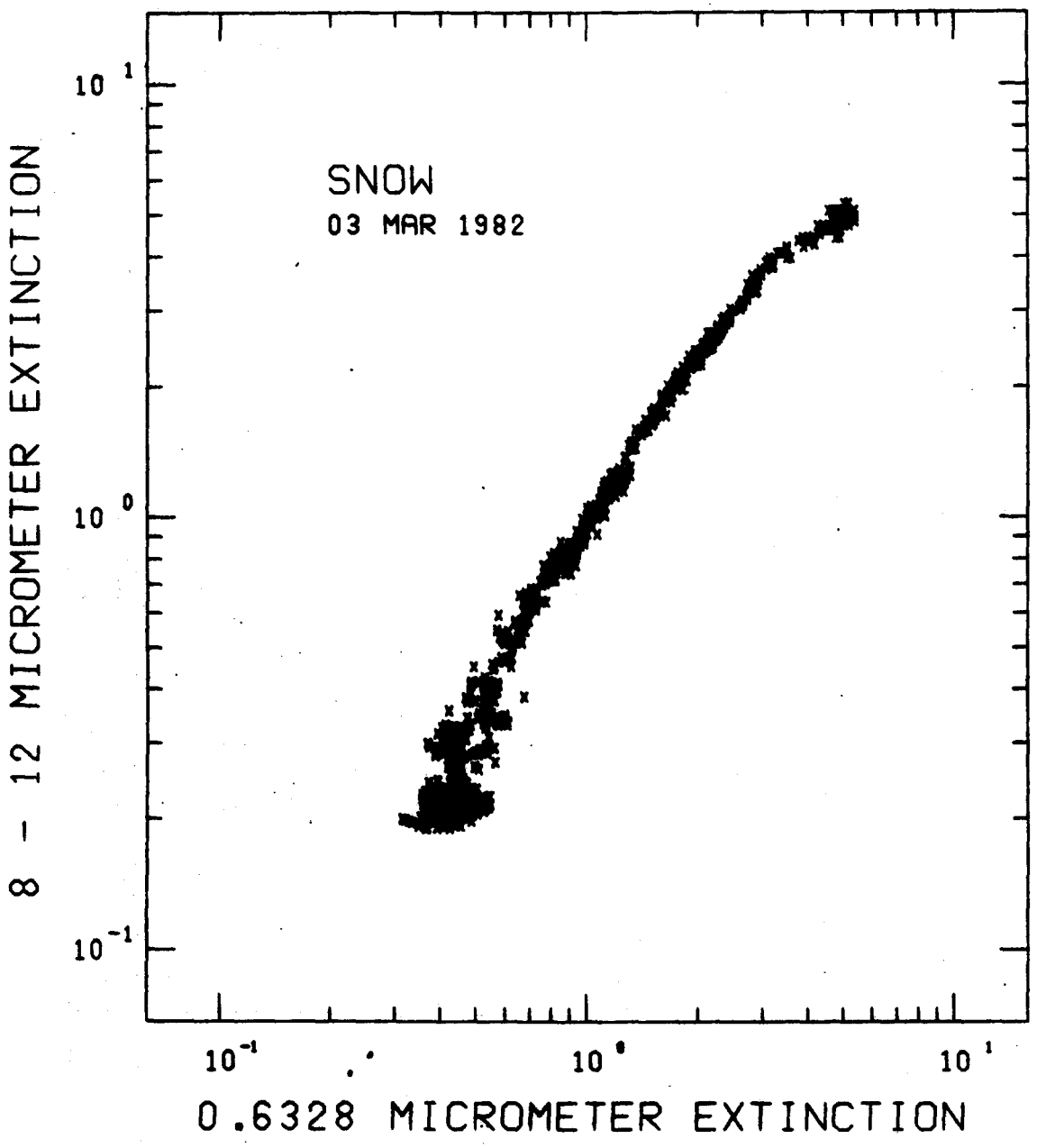

Figure 53. Extinction in snow, 03 March 1982.

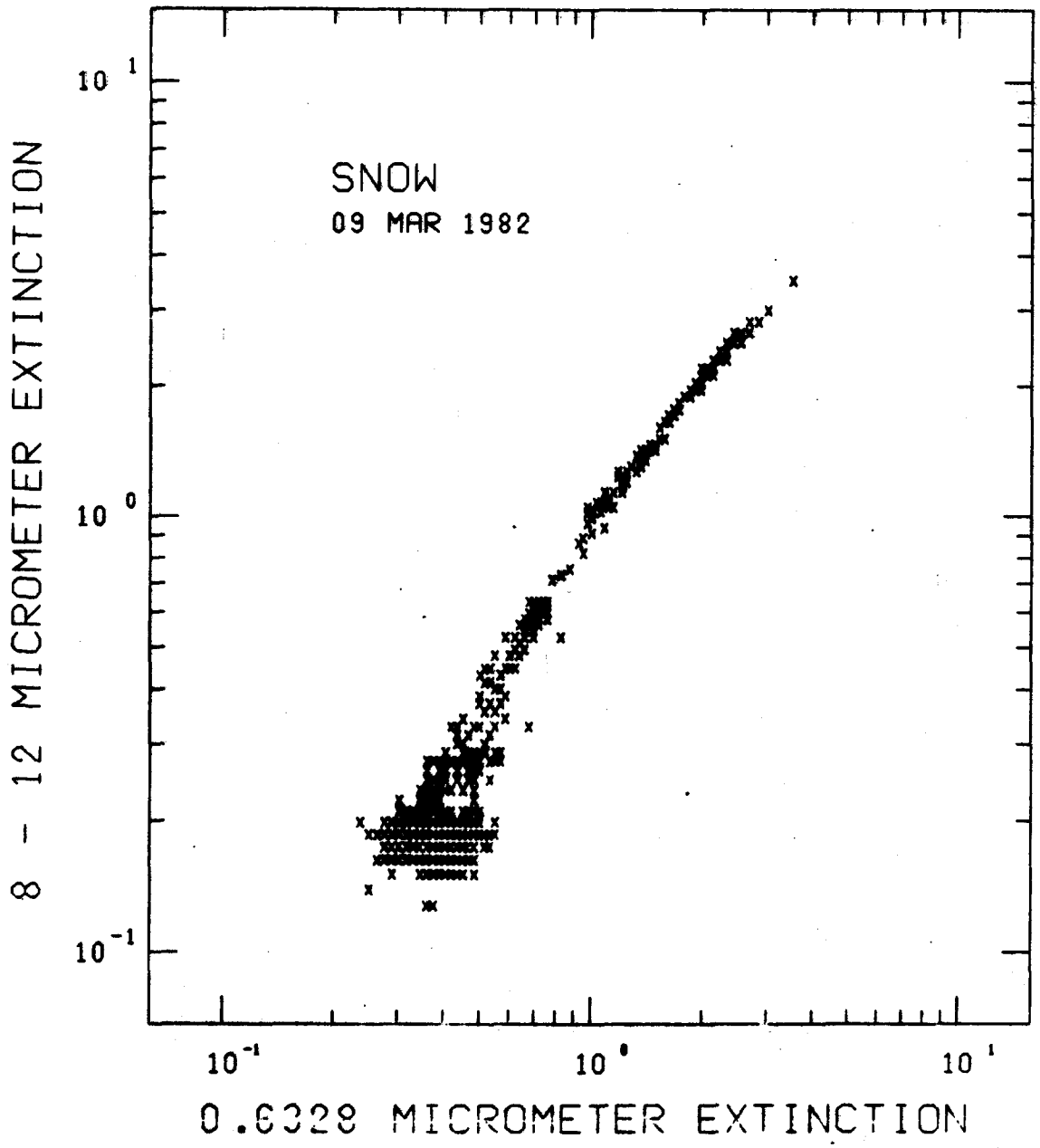

Figure 54. Extinction in snow, 09 March 1982.

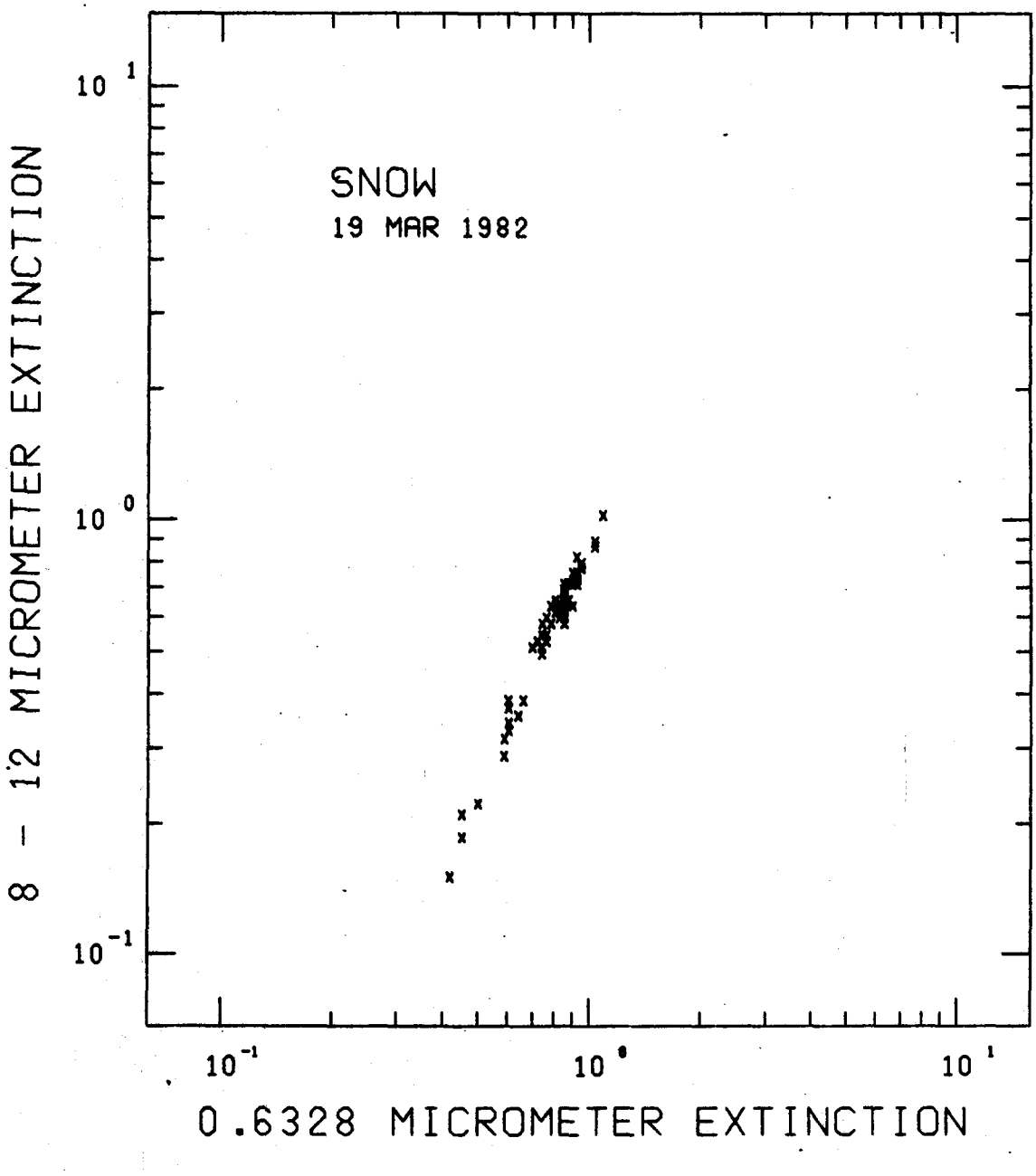

Figure 55. Extinction in snow, 19 March 1982.

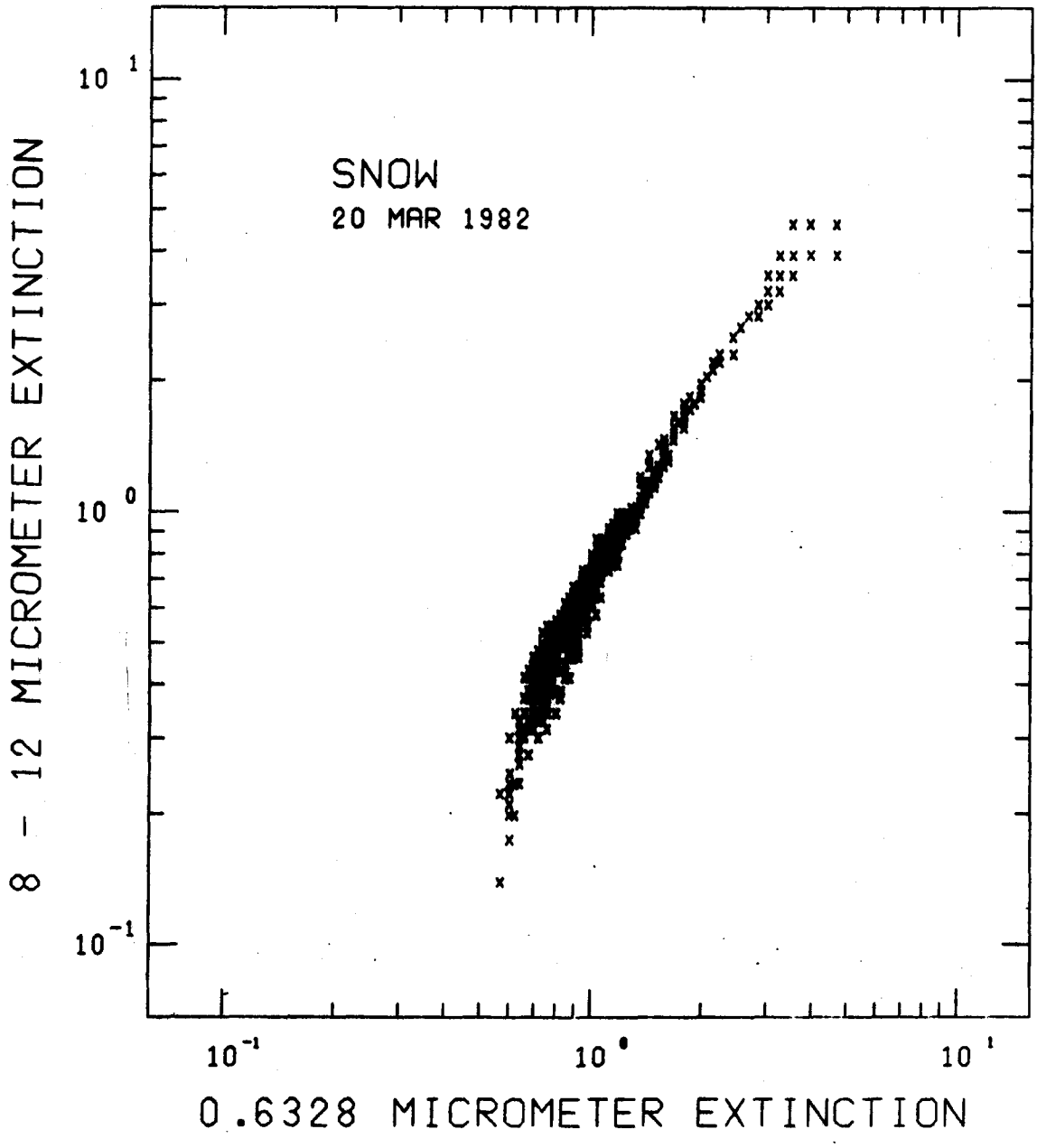

Figure 56. Extinction in snow, 20 March 1982.

platelets. The slope of the curves depends on both the phase function of crystals at the wavelengths of interest and on the susceptibility of the transmissometer receivers to scattered radiation.

The spread in the transmission data for small values of the extinction coefficient (less than 1.0 km^{-1}) has been attributed to the extinction measurements at 1.06 micrometers. Since the output of the Nd:YAG laser has been found to vary by as much as 20%, the output is continuously monitored and the return power is ratioed by the input power. Therefore, laser power fluctuations are not the cause of the spread. It is possible that the phase function of snow is considerably different than the phase functions at 0.6328 micrometers and in the 8 to 12 micrometer band. If the liquid water associated with snow crystals was having an effect on the phase function at 1.06 micrometers, a variation in the phase function may be expected within any given snow crystal type. However, a similar effect should be seen in the 8 to 12 micrometer band because of the higher imaginary index of refraction of water in this band.

When the extinction due to two types of natural obscurants is measured, a larger data spread is found as is curvature of the parameterized GAP curve. Measurements of extinction in the 8 to 12 micrometer band are graphed as a function of the extinction at 0.6328 micrometers in Figure 57. The evidence of a fog formation and dissipation can be seen in the data of 10 June 1981. The curvature is attributed to simultaneous rain and fog in amounts varying in time. Varying amounts of rain and snow on 31 March 1982 account for the behavior seen in Figure 58.

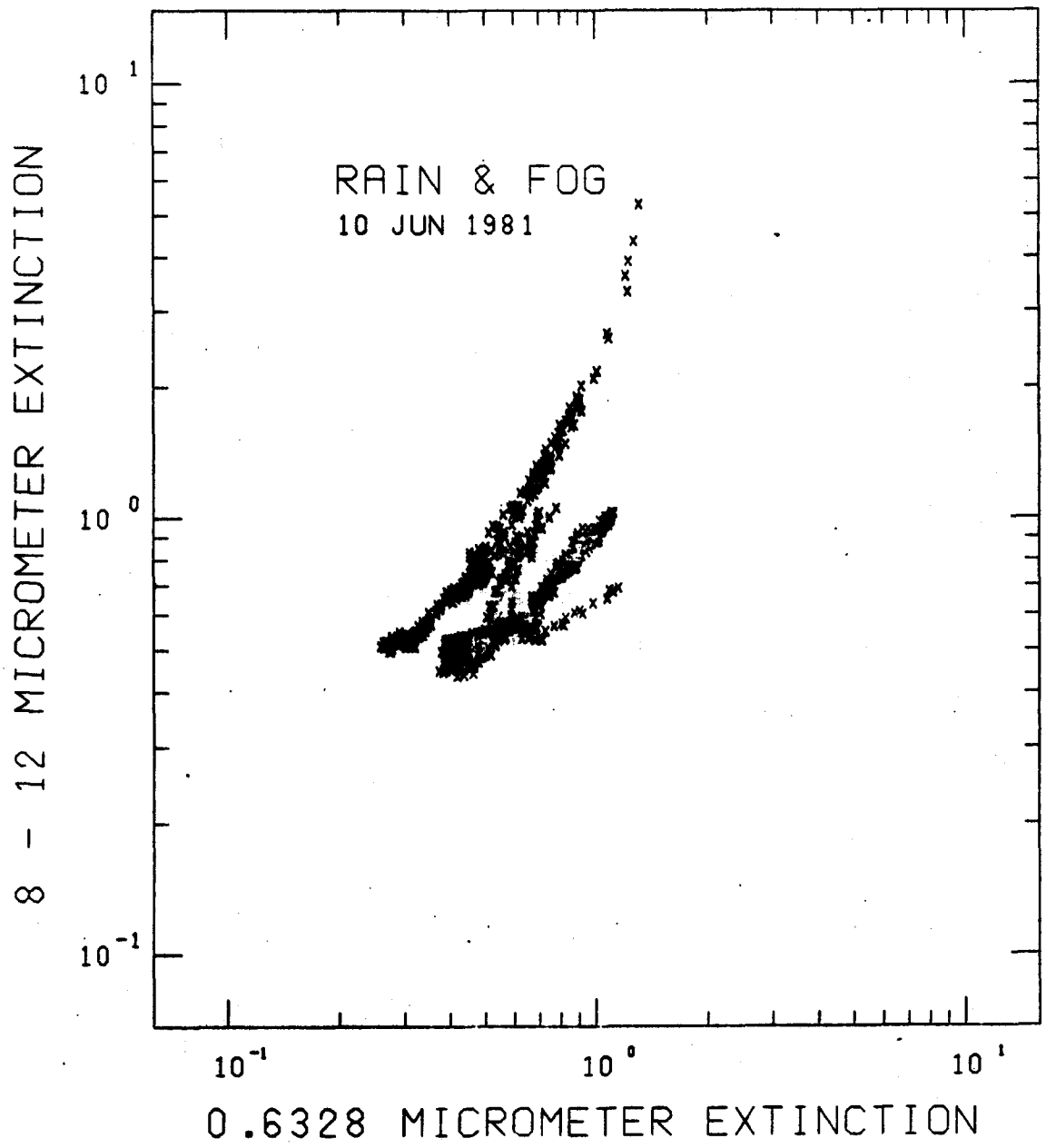

Figure 57. Extinction in rain and fog, 10 June 1982.

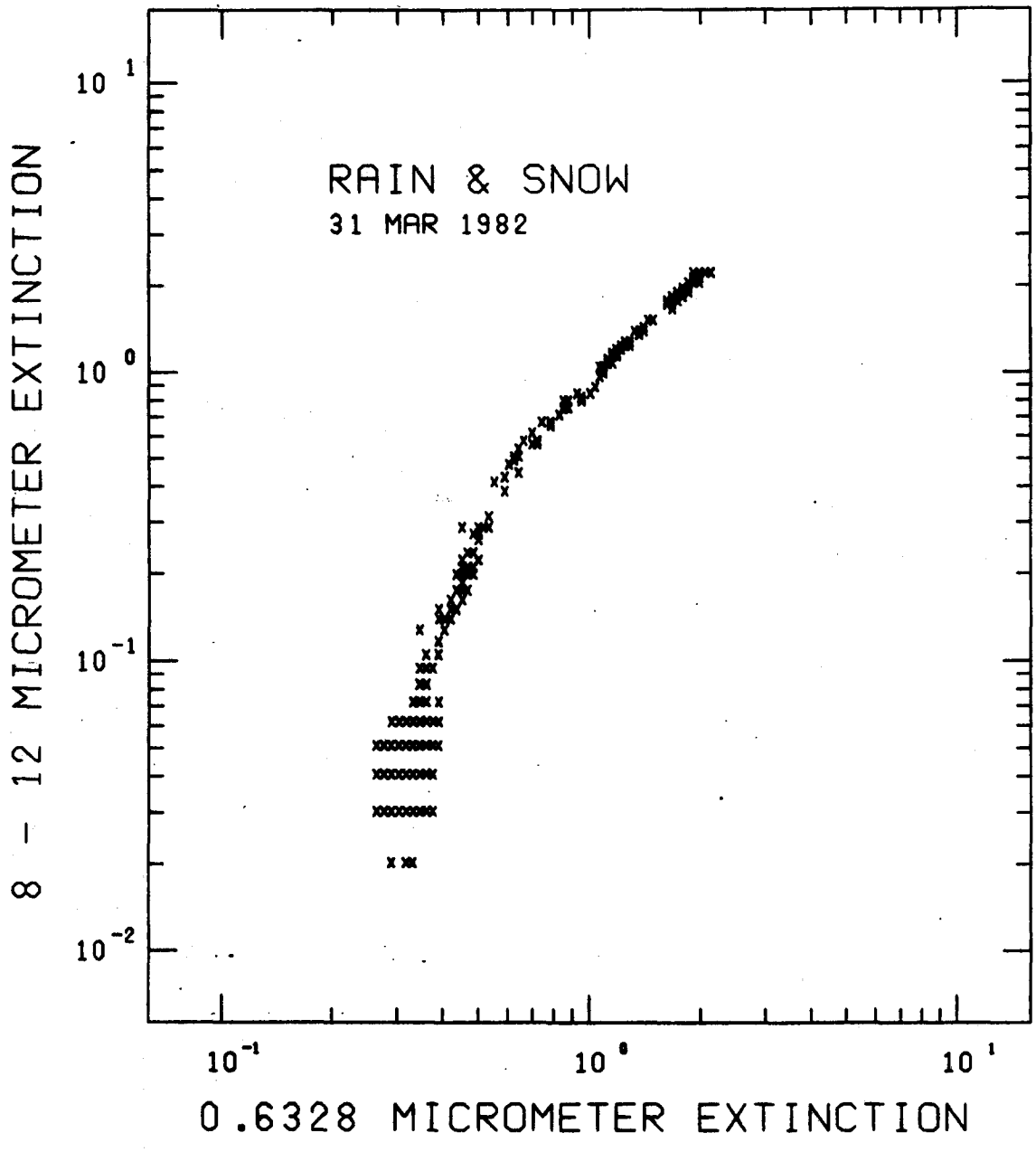

Figure 58. Extinction in rain and fog, 31 March 1982.

REFERENCES

Asano, S. and G. Yamamoto, Appl. Optics 14 29 (1975).

Barteneva, O.D., Dougyallo, Ye.N., and Polyakova, Ye.A., Tr. GGO (1967).

Best, A.C., Quart. J. Ray. Meteorol. Soc. 76 16-36 (1950).

Bisyarin, V.P., Bisyarina, I.P., Ruback, V.K., and Sokolov, A.V., Radio Eng. Electron. Phys. 16 1594-1597 (1971).

Born, M. and E. Wolf, Principles of Optics, 4th Ed., Pergamon Press, New York, 1970.

Bruscaglioni, P., Optics Commun. 27 9-12 (1978).

Bruscaglioni, P., Lett. Nuovo Cimento 24 485-488 (1979).

Bruscaglioni, P. and A. Ismaelli, Nuovo Cimento 1C 147-166 (1978).

Bruscaglioni, P. and A. Ismaelli, Optica Acta 26 679-691 (9179).

Carradina, C. and G. Tonna, Atmos. Environ. 15 271 (1981).

Chu, T.S. and D.C. Hogg, B.S.T.J. 47 723-759 (1968).

Chýlek, P., J. Atmos. Sci. 35 296 (1978).

Dugin, V.P., B.M. Golubitskiy, S.O. Mirumyants, P.I. Paramonov, and M.V. Tantashev, Izv. Atmos. Ocean. Phys. 7 581 (1971).

Dugin, V.P., O.A. Volkovitskiy, S.O. Mirumyants, and N.K. Nikiforova, Izv. Atmos. Ocean. Phys. 13 22 (1977).

Duncan, L.D., R.C. Shirkey, R.A. Sutherland, E.P. Avara, and H.H. Monahan, ASL-TR-0047 (1979).

Eklund, H., S. Lundqvist, B. Marthinsson, and S.T. Eng, Infrared Physics 18 337-342 (1978).

Fabelinskii, I.L., Molecular Scattering of Light, Plenum Press, New York, 1968.

Greenberg, J.M., A.C. Lind, R.T. Want, and L.F. Libelo in Electromagnetic Scattering, R.L. Rowell and R.S. Stein, eds., Gordon and Breach, New York, 1967.

Huffman, P., J. Atmos. Sci. 27 1207 (1970).

Huffman, P.J. and W.R. Thursby, J. Atmos. Sci. 26 1073-1077 (1969).

Jacobowitz, H., J. Quant. Spectrosc. Radiat. Transfer 11 691-695 (1971).

Jessen, W., A. Kohnle, H. Hipp, and D.H. Hohn, Infrared Phys. 20 175-183 (1980).

Kagiwada, H. and R. Kalaba, Rand Report RM-5537-PR, Rand Corporation, Santa Monica, CA, 1967.

Kerker, M., The Scattering of Light, Academic Press, New York, 1969.

Laws, J.O., Trans. Am. Geophys. 22 709-721 (1941).

Laws, J.O., and D.A. Parsons, Trans. Am. Geophys. 24 452-460 (1943).

Liou, K.N., Appl. Optics 11 667 (1977a).

Liou, K.N., J. Atmos. Sci. 29 524 (1972b).

Liou, K.N., R. Baldwin, and T. Kaser, J. Atmos. Sci. 33 553 (1976).

Liou, K.N. and R.F. Coleman in Light Scattering by Irregularly Shaped Particles, D.W. Schuerman, ed., Plenum Press, New York, 1979.

McClatchey, R.A., W.S. Benedict, S.A. Clough, D.D. Burch, R.F. Calfee, K. Fox, L.S. Rothman, and J.S. Goring, AFCRL-TR-73-0096 (1973).

Mie, G., Ann. Physik 25 377-445 (1908).

Moulton, J.R., R.J. Bergeman, and M.C. Sola, IRIS Symposium, 1976.

Mugnai, A. and W.J. Wiscombe, J. Atmos. Sci. 37 1291 (1980).

Nikiforova, N.K., L.N. Pavlova, A.G. Petrushin, V.P. Synkov, and O.A. Volkovitskiy, J. Aerosol. Sci. 8 243 (1977).

Pinnick, R.G., D.L. Hoijelle, G. Fernandez, E.B. Stenmark, J.D. Lindberg, G.G. Hoidale, and S.G. Jennings, J. Atmos. Sic. 35 2020 (1978).

Pinnick, R.G., S.G. Jennings, P. Chýlek, and H.J. Auvermann, J. Atmos. Sci. 36 1577 (1979).

Roach, W.T., R. Brown, S.J. Caughey, J.A. Garland, and C.J. Readings, Quart. J. R. Met. Soc. 102 313 (1976).

Sassen, K. and K.N. Liou, J. Atmos. Sci. 36 838 (1979a).

Sassen, K. and K.N. Liou, J. Atmos. Sci. 36 854 (1979b).

Selby, J.E.A., F.X. Kneizys, J.H. Chetwynd, Jr., and R.A. McClatchey, AFGL-TR-78-0053 (1978).

Shields, F.S., NV&EOL Internal. Memorandum, 1978.

Shifrin, K.S., Scattering of Light in a Turbid Medium, NASA TT F-477 (1968).

Smith, H.J.P., D.J. Duke, M.E. Gardner, S.A. Clough, F.X. Kneizys, and L.S. Rothman, AFGL-TR-78-0081 (1978).

Sokolov, A.V. and Sukhonin, Ye.V., Radio Eng. Electron. Phys. 15 2167-2171 (1971).

Turner, R.E., F.G. Gerhardt, J.L. Manning, R.E. Meredith, S.M. Singer, F.G. Smith, and P.C. Vavra, ASL-CR-80-0177 (1980).

Van de Hulst, H.C., Light Scattering by Small Particles, Wiley, New York, 1957.

Volkovitskiy, O.A., L.N. Pavlova, and A.G. Petrushin, Izv. Atmos. Ocean. Phys. 16 98 (1980).

Wait, J.R., Can. J. Phys. 33 189 (1955).

Wendling, P., R. Wendling, and H.K. Weickmann, Appl. Optics 18 2663 (1979).

Winchester, Jr., L.W., W.K. Choi, G.G. Gimmestad, S.M. Lee, and P.N. Parks, Poc. 2nd KRC Symp. on Ground Vehicle IR Signatures 1 123-131 (1980a).

Winchester, Jr., L.W., W.K. Choi, G.G. Gimmestad, S.M. Lee, and P.N. Parks, JOSA 70 1561 (1980b).

Winchester, Jr., L.W., G.G. Gimmestad, S.M. Lee, and D.K. Wilburn, TACOM Tech. Report 12612, 1981.

Winchester, Jr., L.W., G.G. Gimmestad, and S.M. Lee, CLEO '82 Tech. Digest 1982.

Winchester, Jr., L.W., Proc. Eleventh International Laser Radar Conference, 1982a.

Winchester, Jr., L.W., Submitted to J. Atmos. Sci. 1982b.

Commander 1
TECTA
Fort Hood, TX 76544
ATTN: ATCAT-CS-STI

Commander 2
Picatinny Arsenal
Dover, NJ 07801
ATTN: ARDAR-LCU-T, Bldg. 24

U.S. Department of Commerce 5
NOAA Environmental Research Laboratory
Technical Reports Boulder, CO 80303
ATTN: Library, R-51

Director 1
U.S. Army Materiel Systems Analysis Agency
Aberdeen Proving Ground, MD 21005
ATTN: DRXSY-T

Director 1
U.S. Army Engineer Waterways Experimentation Station
Vicksburg, MS 39180
ATTN: Library Branch

Commander 1
U.S. Army Aviation Test Board
Fort Rucker, AL 36360
ATTN: STEBF-PO

Commander
U. S. ArmyArmor and Engineering Board 1
Fort Knox, KY 40121
ATTN: ATZK-AE-TE-E

Commander 1
U.S. Naval Test Center
Code 3941
China Lake, CA 93555

Commander 2
U.S. Army Mobility Equipment Research and Development Command
Fort Belvoir, VA 22060
ATTN: DRDME-RT

Commander
U.S. Army Electronics Research and Development Command
Night Visions and Electro-Optics Laboratory
Fort Belvoir, VA 20060
ATTN: DELNV-VI 10
DELNV-L 2

DISTRIBUTION LIST

	COPIES
Commander U.S. Army Tank Atuomotive Research and Development Command Warren, MI 48090	
ATTN: DRCPM-FVS	1
DRCPM-M60	1
DRCPM-M113	1
DRDTA-TSL	5
DRDTA-ZSC	30
Director Defense Advanced Research Projects Agency 1400 Wilson Blvd. Arlington, VA 22209	1
Defense Technical Information Center Cameron Station Alexandria, VA 22314	
Commander Harry Diamond Laboratories Adelphi, MD 20783	
ATTN: DRXBO-RAL	1
DELMD-R-CM	1
Commander U.S. Army Missile Command Redstone Arsenal, AL 35809	
ATTN: DRSMI-TEI	2
DRSMI-REO	1
DRSMI-REL	1
DRSMI-OG	1
DRSMI-RPRD	1
DRSMI-RRA	1
DRSMI-RRO	1
DRSMI-RHC	1
Commander U.S. Army Electronic Proving Grounds Fort Huachuca, AZ 85613	1
ATTN: STEEP-MT-ST	
Director U.S. Army Ballistic Research Laboratories Aberdeen Proving Ground, MD 21005	1
ATTN: DRXBR-LB	

Commander
U.S. Air Force Systems Command
Wright-Patterson AFB, OH 45433
ATTN: AGM-65, SD65 E — 2

Commander
U.S. Air Force Armament Laboratory
Eglin AFB, FL 32542
ATTN: AFATL-DLB — 4
AFATL/DLODL Technical Library — 4

Commander
U.S. Army Atmospheric Sciences Laboratorys
White Sands Missle Range, NM 88002
ATTN: DELAS-EO — 5

Commander
U.S. Army Cold Regions Research & Engineering Laboratory
Hanover, NH 03755
ATTN: CRREL-RD — 1
CRREL-RG — 2

U.S. National Aeronautic and Space Administration — 1
ATTN: Chief of Planetary Materials
Lyndon B. Johnson Space Center
Houston, TX 77058

U.S. Army Chemical Systems Laboratory — 2
Aberdeen Proving Ground, MD 21012
ATTN: DRDAR-CLB-PS

Air Force OSR/NC — 1
Bolling Air Force Base
Washington, D.C. 20332

Project manager Smoke/Obscurants — 3
Aberden Proving Ground, MD 21005
ATTN: DRCPM-SMK

Air Force GL — 1
Hanscom AFB
Bedford, MA 01731

Commander — 1
U.S. Army Combined Arms Combat Developments Activity
Fort Leavenworth, KS 66027
ATTN: ATCA-CCC-S